University of Cape Town

Faculty of Engineering and the Built Environment

Structural Investigation of Negative Gaussian Curvature Shells as Liquid-Storage Vessels

Candidate

Hlasoa Mahlelebe

Supervisor

Professor Alphose Zingoni

Thesis in partial fulfilment of the requirements for the degree of

Master of Science in Engineering in Structural Engineering and Materials

In the Department of Civil Engineering

UNIVERSITY OF CAPE TOWN

July 2023

Plagiarism Declaration:

1. I am presenting this dissertation in FULL/PARTIAL fulfilment of the requirements for the degree.
2. I know that plagiarism is wrong. Plagiarism is using another's work and pretending that it is one's own.
3. This dissertation has been submitted to the Turnitin module (or equivalent similarity and original checking software) and I confirm that my supervisor has seen my report and any concerns revealed by such has been resolved with my supervisor.

4. I hereby grant the University of Cape Town a free licence to reproduce for the purpose of either the whole or any portion of the contents in any manner whatsoever of the above dissertation.

Signed: Signed by candidate Date:24 /07/2023

Abstract

Shells of negative Gaussian curvature, such as hyperboloid of revolution, can be seen in most parts of the world in application in the energy industry as cooling towers supported on the large surface area on the ground (Zingoni, 2018). Hyperboloid of revolution shell has been found to resist self-weight stresses better when used as a cooling tower, and it is constructed to heights up to 200m or even more (Zingoni, 1999). Concrete can be moulded into almost any shape, provided the formwork is well constructed to give the desired shape. This makes it possible to be built into a large-capacity supersized tank (Zingoni, Mokhothu & Enoma, 2015).

Some research has emerged on the analysis and design aspects of some elevated liquid containment vessels such as cylindrical, spherical, conical, and an Inze tank (a tank of compound geometry comprising of spherical top closure, vertical cylindrical sides, a conical transition in a lower part and a spherical bottom closure). The current study explores the structural investigation of hyperboloidal shells of revolution when used on a different application as a form of elevated liquid-containing vessel, making the current study novel in liquid containment application.

In the current study, closed-form analytical solutions for membrane stress resultants due to hydrostatic loading have been developed and were used to conduct the structural investigation. The solutions developed were based on the membrane theory for shells of revolution for the concrete vessel and can be used to assess the membrane stress state at any point on the hyperboloidal vessel subjected to hydrostatic loading. It was found that increasing the geometric ratio of *b/a* decreased the maximum membrane meridional stress resultant from vessel to vessel. However, the same increase of *b/a* increased the maximum hoop stress resultants. The hoop stress resultants were 2.3 times the meridional stress resultant for the geometric ratio *b/a* =2.1 and 4.4 times for *b/a* = 2.8. Therefore, the hoop stresses were taken as governing the structural design. The Finite Element Method (FEM) using ABAQUS software was also used to check the accuracy of the derived closed-form solutions. These were in good agreement with an error of less than 5% for both hoop and meridional stresses, hence the developed equations are reliable in predicting stresses in the vessel due to hydrostatic loading.

Furthermore, the FEM method using ABAQUS software was used to conduct a linear eigenvalue buckling analysis for zones that experience significant compressive stresses in the hyperboloidal vessel. The meridional stresses were entirely in compression throughout the vessel for all eight tested vessels from a *b/a* ratio of 2.1 to a *b/a* ratio of 2.8. It was found that increasing the geometric ratio of *b/a* increases the linear buckling capacity of the vessel when subjected to hydrostatic loading. The eigenvalues occurred in pairs, which resembles a feature of symmetry of symmetrical structural systems. The other observation was that the eigenvalues

were negative, which meant that the loading must be reversed for buckling to occur on the vessel. The first eigenvalue means that the liquid must be 24.914 times denser than water for the vessel to buckle. As a result, the vessel will be safe even after imperfections have been accounted for in the non-linear buckling analysis (Zingoni, 2022).

A comparative study was also conducted for the hyperboloidal vessel versus the circular cylindrical vessel on hoop stress resultants with the equivalent volumes, height, and thickness of the vessels and the same material properties of concrete (unreinforced). The maximum stresses on the eight studied vessels showed that the hoop stresses in the circular cylinder ranged from 1.2 times to 1.5 times that of the hyperboloidal vessel. The linear buckling analysis for the eight studied vessels under hydrostatic loading revealed a factor of safety in the range 24.9 to 29.4. Results obtained on the stress analysis and linear eigenvalue buckling analysis in this study motivate that future research may be conducted for further structural investigations such as nonlinear buckling analysis, seismic analysis, and the effect of bending disturbances on the negative Gaussian shells to be considered for high-volume containment. However, it should be kept in mind that the loading on the structure was strictly hydrostatic only, which is one of the key limitations of this study.

Acknowledgements

I would like to thank God for giving me the strength to work on this dissertation to completion.

I would like to thank my supervisor at the University of Cape Town, Professor Alphose Zingoni, for his full guidance on the dissertation. I would also like to thank him for his support through funding for fees and living expenses for my studies and for making it possible for me to complete this masters.

I would also like to thank my parents Ntate Teboho Daniel Mahlelebe and ‘M’e Mahlasoa Agnes Mahlelebe, and my sister Masempe Alexina Mahlelebe for always offering support throughout the masters journey.

Table of contents

List of Figures

List of Tables

Nomenclauture

A	Mean radius of a toroidal shell
a	Throat radius of the hyperboloidal vessel
b	Curvature constant of the hyperboloid of revolution
H	Height of the hyperboloidal vessel
ϕ_c	Angular coordinate measuring the angle from the upward direction of the local axis y-y-y around the meridian
ϕ_e	The meridional angle at a shell edge
ϕ	Meridional angle
θ	Hoop circle angle
N_ϕ	Meridional stress resultant
N_θ	Hoop stress resultant
r_1	The principal radius of curvature
r_2	The secondary radius of curvature
p_ϕ	Load per unit area in the meridional direction
p_θ	Load per unit area in the hoop direction
p_r	Load per unit area in the normal direction
H_e	Horizontal shear force edge redundant
M_e	Bending moment area redundant
p_{crit}	Critical buckling pressure
γ	Weight per unit volume
η	Structural efficiency of the containment vessel
λ	Eigenvalue

1 Introduction

Shell structures are man-made structures that have existed for centuries in the civil engineering industry. However, the roofing application of shells in public space areas was the first application of shell structures in history. The Pantheon of ancient Rome is a notable example of a historical shell structure built around two thousand years ago. More examples of this roofing application can be found in (Zingoni 2018:1). For thin shells, the thickness dimension of shell structures is significantly less when compared to the other two dimensions, a reason for them being called thin structures (Sharma, Sharma & Mukhija, 2021).

The modern application of shell structures in civil engineering is a result of their high strength-to-weight ratios and several other properties, such as high stiffness and form (Zingoni, 2018:1). These modern applications include liquid-containment structures, liquid-retaining structures, and containment shells of nuclear power plants (Frank J & Michel P, 1987; Sharma, Sharma & Mukhija; Nasir et al., 2002; Zingoni, 2018:6). For the different modern applications of shell structures, some factors need to be considered for the shell structure to be structurally sound. These include the type of shell surface, the loading configuration, the boundary conditions, discontinuities at edges, and gaussian curvature (Zingoni, 2018:10).

Gaussian curvature (a product of two principal radii of curvature of a shell element at any given point) is the most crucial property of shell structures used to classify the shell structure based on the surface. There are three classes of shell surfaces, namely, synclastic surfaces (positive Gaussian curvature), anticlastic (negative Gaussian curvature), and developable characters (zero Gaussian curvature) (Zingoni, 2018:11). The Gaussian curvature is positive if both principal radii of curvatures lie on the same side of the surface at any given point. It is negative when the principal radii lie on opposite sides of the surface and developable when they have one radius of curvature approaching infinity (Zingoni, 2017:11). Apart from the classification based on curvature; shell structures can be classified using the geometric form.

Classification based on the geometric form can be broken down into two classes: surfaces of revolution and surfaces of translation. Surfaces of revolution can be generated by rotating a plane curve known as a meridian about the axis of revolution (Sharma, Sharma & Mukhija, 2021; Mathieu, Shambina & Jaafar, 2021). Examples are circular cylinders, cones, elliptical or spherical domes, toroids and hyperboloids of revolution. On the other hand, a surface of translation is generated by keeping a plane curve parallel to its initial plane when moving it along a different plane curve (Sharma, Sharma & Mukhija, 2021). Surfaces of revolution are widely used as liquid-containment shell structures (Zingoni, 2015).

A shell of revolution possesses the advantage of a high strength-to-weight ratio, which gives it excellence when used as a containment (Zingoni, 2015). According to Zingoni (2018), the basis for the design of reinforced concrete and liquid storage tanks can be traced from the early 1940s when Slater began the work on their design. Gary (1948), Timoshenko and Woinowski-Krieger (1959), and Wilby (1977) also contributed to the fundamentals of the design of such tanks.

Containment structures such as elevated liquid storage vessels exist in various geometrical forms such as circular cylindrical vessels, spherical vessels, and circular conical vessels or a combination of different geometrical shapes such as an intze tank (Zingoni, 2017:68-74). Concrete has the property of mouldability, which gives it the advantage of being formed into various geometrical forms. However, Zingoni (2015) states that not much research has explored new shell forms for concrete tanks. It thus opens a gap for further research for more efficient shell configuration solutions for large supersized liquid tanks (Zingoni, 2015).

1.1 Problem statement

Urbanisation has significantly increased demand for potable water in cities around the world. As a result, more efficient and economic large capacity containment structures are needed to address the problem. This study is a structural investigation of new and potentially more efficient liquid-containment structures as search for solutions for high-capacity elevated liquid storage tanks continues. Negative Gaussian shells in the form of a hyperboloidal shape used as cooling tower in the energy sector were found effective in resisting self-weight stresses on a study by Zingoni (1999). Therefore, this study is a structural investigation on negative Gaussian shells as a new shell form as liquid containment structure.

1.2 Research objectives and scope

This study investigates the structural feasibility of liquid-storage shells of revolution of negative Gaussian curvature. With a particular interest in the hyperboloidal shell of revolution while used as a liquid-containing vessel. To accomplish the objective, the dissertation will:

1. Derive closed-form analytical expressions for the membrane meridional and hoop stress resultants of a hyperboloidal tank based on membrane theory
2. Check and compare the analytical solutions with numerical analysis solutions using the Finite Element Analysis software (ABAQUS)

3. Then, carry out a parametric study of how such stresses vary with the geometric ratio *b/a* of the hyperbola and produce plots of meridional stress resultant N_ϕ and the hoop stress resultant N_θ against the height coordinate *y*
4. Comparing the stress variations of a hyperbolic bell tank versus those of a circular bell tank
5. Investigation of the linear buckling behaviour of such vessels, especially for those ranges of geometric parameters where the stress analysis reveals the presence of significant compressive stresses using ABAQUS

1.3 Limitations

1. The structure will only be subjected to hydrostatic loading for analysis, therefore only stress behaviour due to hydrostatic loading will be considered in this study (see section 3.1.2)
2. The stress analysis will be based on membrane theory of shells of revolution
3. A non-linear buckling analysis study will not be part of the buckling stability analysis.
4. No physical tests will conducted in the laboratory due to time constraints, however physical testing in crucial in validating the results obtained from analytical methods and numerical methods. The Finite Element Analysis (FEA) model will be calibrated against existing models.

1.4 Research Aim

Zingoni (2015b) reviewed recent findings regarding the strength, stability, and dynamics of liquid-containment shells of revolution. In this review, opportunities for future research emerged. One of the future recommendations was to explore new and more efficient shell configurations, seeking solutions for high-capacity elevated liquid storage. He also mentioned that high concrete water tanks could be moulded and constructed into various shapes because fresh concrete can be moulded into different shapes using formwork. He further emphasised that the structure's resistance to external loading depends on its shape. According to Nasir et al. (2002), hyperboloidal shell structures are the most efficient and economical solution used as axisymmetric shells. However, not much exploration of this shell forms has been done for other applications such as liquid containment. Therefore, this dissertation is a structural investigation of the hyperboloid of revolution, a negative Gaussian surface, used as a new geometrical form in a liquid containment application taking into account the limitations outlined in section 1.3.

1.5 Elevated liquid storage tanks

Shell structures built with different materials are widely used around the globe for large capacity liquid containment application. Figures 1-4 to 1-7 show some examples of elevated liquid storage tanks currently used in industry to contain various liquids depending on the application.

Figure 1-1:spherical vessel with liquefied gas [https://www.marksanglobal.com/oil-gas-storage.php]

Figure 1-2:Ellipsoidal pressure vessel for gas storage [https://m.indiamart.com/proddetail/lpg-spherical-tank-4189894597.html]

Figure 1-3:Cylindrical elevated water-storage vessels [https://www.istockphoto.com/photo/the-elevated-reinforced-concrete-water-tank-tower-gm1067756220-285572190]

Figure 1-4:Elevated cylindrical tank [https://www.hydrex.co.za/industries/water-storage]

2 Literature review

Stress analysis and linear buckling analysis are preliminary steps for the structural investigation of containment structures. Membrane theory of shells of revolution gives the best approximation of the true stresses in the shell in the meridional and hoop (radial) direction which are essential for stress analysis. This chapter begins with the brief review of membrane theory of shells of revolution and then further reviews the current research on different aspects considered for the structural investigation of shell structures.

This chapter focuses on different unusual profiles of shells of revolution in the application as liquid-containment vessels. Shells of revolution in this section are classified according to the Gaussian curvature. These are thin structures built as curved surfaces, and this curvature gives shell structures adequate strength (Nasir et al., 2002). Shells of revolution are Gaussian surfaces with either positive or negative curvature, and this section will look at various aspects of those shells. The various aspects covered include (i) shell geometry and optimisation; (ii) stress analysis of the shell; (iii) junction problems; (iv) buckling and stability analysis; (v) FEM modelling and experimental studies, and (vi) design and construction considerations of these atypical geometries of shells of revolution.

2.1 The membrane theory of shells of revolution

Membrane theory of shells of revolution is valid provided the structure being investigated meets the criteria as discussed by Zingoni (2018:26). A surface of revolution is generated by rotating a plane curve through 360^{o} about a straight line called the axis of revolution (Zingoni, 2018:35). In Figure 2-1, the plane curve is the line *y=cos x,* and the axis of revolution is the *y-axis.*

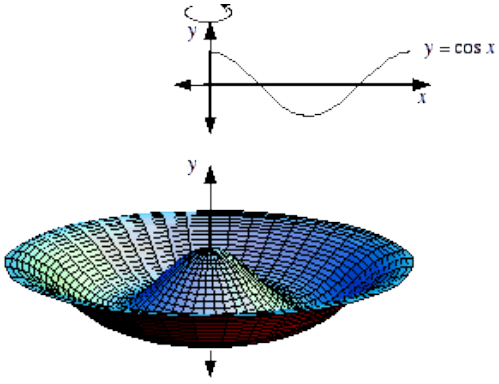

Figure 2-1:Generating a surface of revolution
(https://www.mathwords.com/s/surface_of_revolution.htm,n.d)

The shells of revolution can either be axisymmetrically loaded or be subjected to anti-symmetric loading. Wind loading is one example of anti-symmetric loading because the structure feels the wind load from where the wind comes from, which in most cases, is not acting on the entire surface of the structure. On the other hand, containment shells of revolution subjected to hydrostatic loading only are axisymmetrically loaded; this is a result of pressure being equal at the same level in a containment vessel.

2.1.1

2.1.1 Geometric preliminaries and loading on a shell element

shows an axisymmetrically loaded shell of revolution element with geometrical parameters describing the element's location on the shell's surface. The assumption is made that no bending moments, twisting moments, or transverse shear forces exist in the shell shown in . The positive sign conversion is that tensile forces are positive, and the compressive forces are negative (Zingoni, 2018:36). The derivations and results presented in sections 2.1.1 to 2.3.3 are extracted from Zingoni (2018:36)

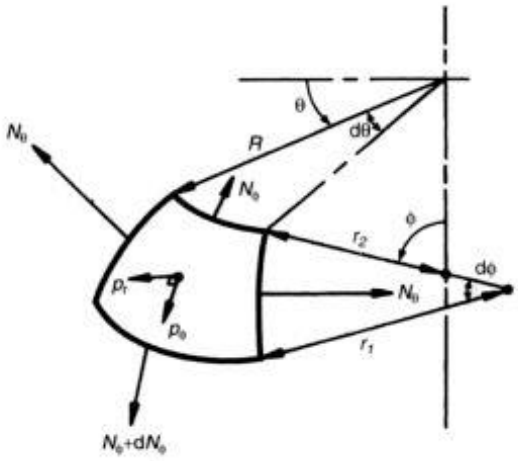

Figure 2-2:Element of axisymmetrically loaded shell of revolution(Zingoni, 2018:36)

Where,

r_1 denotes the principal radius of curvature

r_2 is the second principal radius of curvature

R is the radius of the circle of latitude through a point

N_ϕ is the meridional stress resultant (force per unit length in meridional direction)

N_θ is the hoop stress resultant (force per unit length in the hoop direction)

p_r is the load per unit area acting normal to the shell mid-surface (positive pointing away from the axis of revolution of the shell)

p_ϕ is the force per unit area of the shell mid-surface acting in meridional direction (positive if acting in the direction of increasing ϕ.)

From , the radius *R* of the circle of latitude at the coordinate ϕ is given by

$$R = r_2 \sin\phi \qquad \textbf{2-1}$$

The edges of the shell element in the two meridional sections are each of arc length $r_1 d\phi$. The upper horizontal edge of the element is of arc length $Rd\theta$, but the lower horizontal edge of the element is of increased arc length $(R + RdR)d\theta$ since *R* has increased with respect to ϕ .
Although the shell element is curved and trapezoidal in projection, its surface area may be approximated as $Rd\theta \times r_1 d\phi$ as if the area is rectangular.

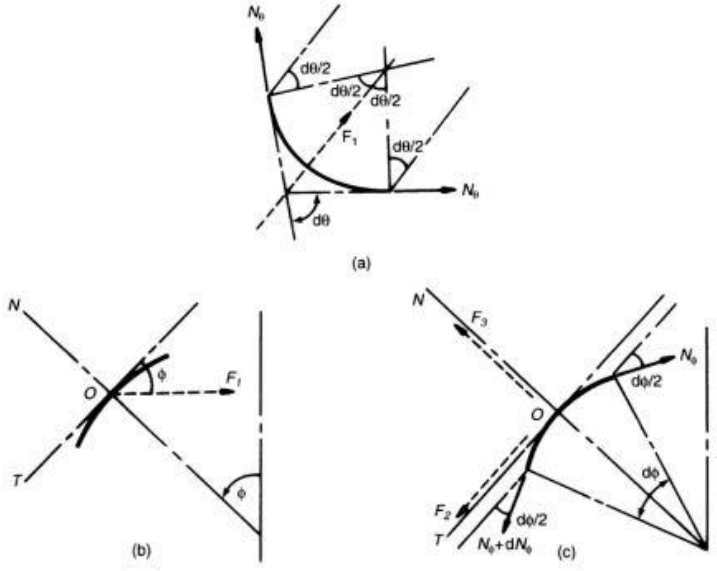

Figure 2-3:Derivations of the governing equations of equilibrium for an element of an axisymmetrically loaded shell of revolution(Zingoni, 2018:37)

2.1.2 Governing equations of equilibrium

The shell element is in equilibrium under externally applied loading, as shown in . shows various sections of the shell element and will be used for derivations of the governing equations. (a) shows the section of the element in the horizontal plane of the circle of latitude. The forces acting at the ends of the element are given by $N_\theta \times r_1 d\phi$. the resultant of these two end forces is a horizontal force F_1 directed towards the axis of revolution of the shell and is given by

$$F_1 = N_\theta \times r_1 d\phi \left(\sin\frac{d\theta}{2}\right) + N_\theta \times r_1 d\phi \left(\sin\frac{d\theta}{2}\right) \qquad \textbf{2-2}$$

$\approx N_\theta \times r_1 d\phi d\theta$ (since $sin\beta \approx \beta$ for very small angles)

(b) shows a section of an element in the vertical plane of a meridian. Resolving F_1 along *OT* (The positive direction of the tangent to the meridian), we obtain the contribution of N_θ to the force resultant along *OT* as

$$-F_1 \cos\phi \qquad \textbf{2-3}$$

Which upon substituting the expression for F_1,

$$-N_\theta \times r_1 \cos\phi \, d\phi d\theta \qquad \textbf{2-4}$$

Figure 2-3(c) shows a section of the shell element in the vertical plane of the meridian, with the meridional forces shown. The total meridional force acting at the upper edge $N_\phi \times Rd\theta$. The total meridional force acting at the lower edge is $(N_\phi + dN_\phi)(R + dR)d\theta$. Resolving these two forces along *OT*, their resultant F_2 is given as

$$\begin{aligned} F_2 &= (N_\phi + dN_\phi)(R + dR)d\theta \times \cos\frac{d\phi}{2} - N_\phi \times Rd\theta \times \cos\frac{d\phi}{2} \\ &\approx N_\phi dRd\theta + RdN_\phi d\theta \\ &= d(RN_\phi)d\theta \end{aligned} \qquad \textbf{2-5}$$

Since $\cos\beta \approx 1$ for very small angles β; the term containing $dN_\phi dRd\theta$ has also been neglected in comparison with the other terms, as it is much smaller.

Finally, the contribution of the external loading to the force resultant along *OT* is simply given by

$$p_\phi \times r_1 Rd\theta d\phi \qquad \textbf{2-6}$$

Summing up all the forces along *OT*, equations 2-4 to 2-6,

$$d(RN_\phi)d\theta - N_\theta \times r_1 \cos\phi \, d\phi d\theta + p_\phi \times r_1 Rd\theta d\phi = 0 \qquad \textbf{2-7}$$

Simplifying by dividing throughout by $d\theta$, equation 2-7 becomes,

$$d(RN_\phi) - N_\theta \times r_1 \cos\phi \, d\phi + p_\phi \times r_1 Rd\phi = 0 \qquad \textbf{2-8}$$

The next step is to determine all the forces acting in the direction of *ON*, which positive is normal to the shell mid-surface. Referring to (b), F_1 (stemming from N_θ)

$$-F_1 \sin\phi \quad \textbf{2-9}$$

Substituting for F_1 yields,

$$-r_1 N_\theta \sin\phi \, d\phi d\theta \quad \textbf{2-10}$$

FromFigure 2-3(c) the resultant of the N_ϕ forces along *ON*, which is denoted by F_3, is given by

$$F_3 = -N_\phi R d\theta \sin\frac{d\phi}{2} - (N_\phi + dN_\phi)(R + dR) d\theta \sin\frac{d\phi}{2} \quad \textbf{2-11}$$

For small angles $\sin(d\phi/2)$ is equal to $(d\phi/2)$ and ignoring relatively small quantities, equation 2-11 becomes

$$\approx -RN_\phi d\theta d\phi \quad \textbf{2-12}$$

The resultant of the external loading along the direction *ON* is given by

$$p_r r_1 R d\phi d\theta \quad \textbf{2-13}$$

Summing up all the contributions, from equations 2-10 to 2-13,

$$-r_1 N_\theta \sin\phi \, d\phi d\theta - RN_\phi d\theta d\phi + r_1 p_r R d\phi d\theta \quad \textbf{2-14}$$

Upon dividing throughout by $d\theta d\phi$ replacing *R* with equation 2-1, and dividing throughout by $\sin\phi$ and re-arranging

$$r_1 N_\phi + r_1 N_\theta = r_1 r_2 p_r \quad \textbf{2-15}$$

Dividing throughout by $r_1 r_2$

$$\frac{N_\phi}{r_1} + \frac{N_\theta}{r_2} = p_r \quad \textbf{2-16}$$

2.1.3 General solution

Equation 2-16 can be written in the form,

$$N_\theta = r_2 p_r - \frac{r_2}{r_1} N_\phi \quad \textbf{2-17}$$

Substitution equation 2-17 into 2-8,

$$d(RN_\phi) - r_1 \left(r_2 p_r - \frac{r_2}{r_1} N_\phi\right) \cos\phi \, d\phi = -r_1 p_\phi R d\phi \quad \textbf{2-19}$$

Dividing throughout by $d\phi$ leads to the expression

$$\frac{d(RN_\phi)}{d\phi} + r_2 N_\phi \cos\phi = r_1 r_2 p_r \cos\phi - r_1 R p_\phi \quad \textbf{2-20}$$

Which, upon multiplication by $\sin\phi$ throughout equations 2-20,

$$\left[\frac{d(RN_\phi)}{d\phi}\right]\sin\phi + (r_2 \sin\phi) N_\phi \cos\phi = r_1 r_2 p_r \cos\phi \sin\phi - r_1 R p_\phi \sin\phi \quad \textbf{2-21}$$

Replacing $(r_2 \sin\phi)$ in the second term of the left-hand side of equation 2-21 by *R*

$$\left[\frac{d(RN_\phi)}{d\phi}\right]\sin\phi + RN_\phi \cos\phi$$

By applying differential calculus

$$\frac{d}{d\phi}(RN_\phi \sin\phi)$$

Thus expression 2-21 now becomes

$$\frac{d}{d\phi}(RN_\phi \sin\phi) = r_1 r_2 p_r \cos\phi \sin\phi - r_1 R p_\phi \sin\phi \quad \textbf{2-22}$$

Integrating both sides of equation2-22

$$(RN_\phi \sin\phi) = \left[\int \left(r_1 r_2 p_r \cos\phi \sin\phi - r_1 R p_\phi \sin\phi\right) \mathrm{d}\phi + k\right] \quad \textbf{2-23}$$

Replacing *R* with $(r_2 \sin\phi)$ to obtain,

$$(\sin^2\phi) N_\phi = \left[\int (r_1 r_2 p_r \cos\phi \sin\phi - r_1 R p_\phi \sin\phi)\, \mathrm{d}\phi + k\right] \quad \textbf{2-24}$$

For which the general solution for N_ϕ can finally be written as

$$N_\phi = \frac{1}{(\sin^2\phi)}\left[\int (r_1 r_2 p_r \cos\phi \sin\phi - r_1 R p_\phi \sin\phi)\, \mathrm{d}\phi + k\right] \quad \textbf{2-25}$$

Where *k* is the constant of integration obtained from the suitable boundary conditions on the shell surface.

2.2 Positive Gaussian curvature surfaces

2.2.1 Egg-shaped profile of parabolic ogival form

These geometric profile vessels are widely used in the industry to contain sludge, and they have been used quite extensively due to the low maintenance costs [2]. Usually, the more complex the geometry of the structural form is, the more expensive it is to construct, considering the complexity of the setting out, including massive formwork for pouring concrete (Zingoni, 2018). However, for this geometrical profile, the high construction costs are offset by the lower maintenance costs in the long run (Zingoni, 2018:94). They are designed to resist hydrostatic pressure from the contained liquid, and hydrostatic pressure is the primary loading condition that requires careful attention. Figure 2-4 shows the geometrical parameters of the parabolic ogival vessel in liquid containment.

The geometry of the parabolic ogival liquid containment vessel may be defined as follows (Zingoni,2018:95):

$$\frac{D}{2} - x = ky^2 \qquad \textbf{2-26}$$

Where k is a constant.

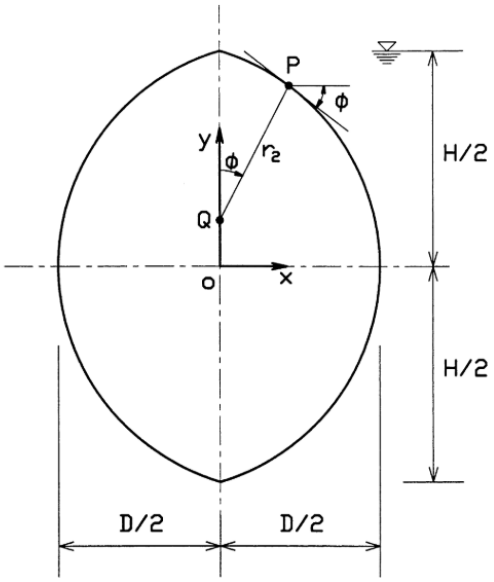

Figure 2-4:Geometrical properties of the parabolic ogival shell (Zingoni, 2002)

2.2.1.1 Shell geometry and optimisation

A thorough search of the literature on this aspect was conducted. Unfortunately, nothing was found in the review. Thus future work may be done on this aspect.

2.2.1.2 Stress analysis of the shell

The membrane theory is used to determine the stress distribution of the parabolic ogival profile as it approximates the exact internal stresses in the hydrostatically loaded parabolic ogival vessel. The hydrostatic pressure varies smoothly from the surface to any depth on the vessel's surface. The other requirements for the membrane theory to be valid through the entire shell surface are the thickness of the body, slope of the meridian, and principal radii of curvature, which all are geometrical properties (Zingoni, 2018:26).

Hydrostatic loading is axisymmetric, and therefore no forces become out of balance. This makes leeway for only two stress resultants concerned for the stress analysis; the hoop stress resultants and the meridional stress resultant (Zingoni, 2018:36). The closed-form membrane meridional stress resultant is given by equation 2-27, and the membrane hoop stress resultant is given by equation 2-28 (Zingoni, 2002).

$$\frac{N_\phi}{\gamma H^2} = \frac{\xi}{16}\left(\frac{\sin\phi}{4\sin^2\phi - \xi^2 cos^2\phi}\right)\left[-\left(\frac{4+\xi^2}{sin^2\phi}\right) + \left(\frac{\xi^2}{2sin^4\phi}\right) - \xi(4+\xi^2)\left(\frac{cos\phi}{sin\phi}\right) + \frac{\xi}{3}(4+\xi^2)\left(\frac{cos\phi}{sin^3\phi}\right)(1+2sin^2\phi) - \frac{\xi^3}{15}\left(\frac{cos\phi}{sin^5\phi}\right)(3+4sin^2\phi+8sin^4\phi) + \frac{1}{30\xi^2}(112+120\xi^2+15\xi^4)\right] \quad \textbf{2-27}$$

$$\frac{N_\theta}{\gamma H^2} = \frac{1}{32\xi^2}(4sin^2\phi - \xi^2 cos^2\phi)\left[\left(\frac{2\xi sin\phi - \xi^2 cos\phi}{sin^4\phi}\right) - \left(\frac{\xi sin\phi}{4sin^2\phi - \xi^2 cos^2\phi}\right) \times \left[-\left(\frac{4+\xi^2}{sin^2\phi}\right) + \left(\frac{\xi^2}{2sin^4\phi}\right) - \xi(4+\xi^2)\left(\frac{cos\phi}{sin\phi}\right) + \frac{\xi}{3}(4+\xi^2)\left(\frac{cos\phi}{sin^3\phi}\right)(1+2sin^2\phi) - \frac{\xi^3}{15}\left(\frac{cos\phi}{sin^5\phi}\right)(3+4sin^2\phi+8sin^4\phi) + \frac{1}{30\xi^2}(112+120\xi^2+15\xi^4)\right]\right] \quad \textbf{2-28}$$

The non-dimensional parameter $\xi = \frac{H}{D}$ in both equations 2-27 and 2-28.

Figure 2-5 shows the plots of the meridional and hoop stress expressed as a non-dimensional number from equations 2-27 and 2-28. The other essential findings from Zingoni (2002), using the non-dimensionless parameter ξ, the hoop stress resultant remained positive (tensile) throughout the vessel, ranging from zero at the very topmost point on the vessel to the maximum value at the point coinciding with the x-axis at the surface, while the meridional stress resultant has both tensile and compressive (negative) values. The meridional stress resultant is tensile from the topmost point (apex) where $\phi = 0°$ up to around the equator where $\phi = 90°$, then decreasing and becoming compressive at regions on the lower part of the tank.

The vessel's height was kept constant while increasing the diameter *D*, leading to the reduction of the non-dimensional parameter ξ. As a result, the hoop stress resultant increased rapidly. The proposed value of the dimensionless parameter is in the range anywhere between 1.5 and 2.0 for practical purposes and to provide the most structurally sound geometry of the parabolic ogival shell of revolution (Zingoni, 2002). This study also found that the stress resultants in the shell are directly proportional to H^2 or D^2.

Zingoni (2002) also defined the structural efficiency of the tank η as the ratio of the non-dimensional volume to the non-dimensional peak hoop stress resultant, which is given by equation 2-29

$$\eta = \frac{V}{H^3} \times \frac{\gamma H^2}{H(N_\theta)_{peak}} = \frac{\gamma V}{H(N_\theta)_{peak}} \qquad \textbf{2-29}$$

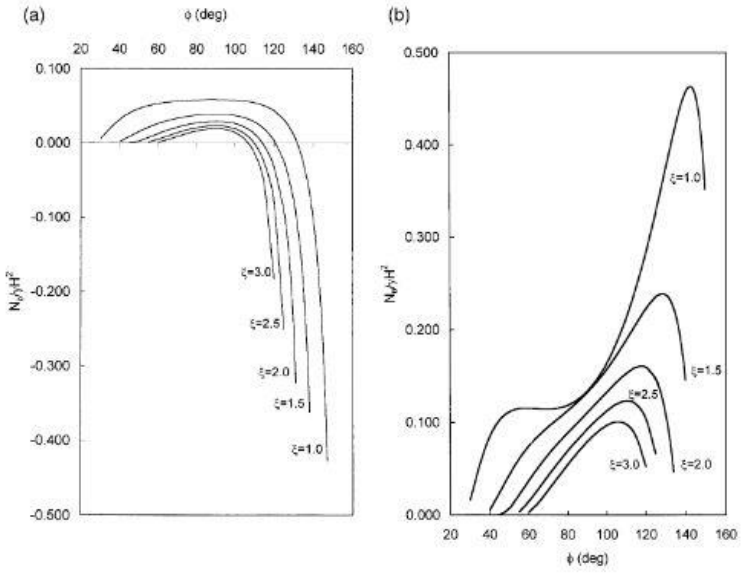

Figure 2-5:Non-dimensional stress variation with ϕ: (a) meridional stresses; (b) hoop stresses (Zingoni, 2002)

2.2.1.3 Junction problems

The membrane theory is valid for stresses in the shell with a smooth surface without discontinuities (Zingoni, 2018:26). When a shell surface is discontinuous, the shell is prone to bending and shear effects at particular locations on the shell where discontinuities are found. Zingoni (2001) investigated how the discontinuities in the sludge egg-shaped sludge digester affect the stresses in the shell. This paper found that discontinuity effects temper with the local meridional pressures and the stresses arising elsewhere in the structure are significantly higher than at the junctions. The stresses governing the design are, therefore, membrane stresses.

The introduction of the discontinuity effects resulted in a slight increase of membrane hoop stress with a tensile magnitude of 0.95N/mm^2, resulting in a net tensile value of 1.09N/mm^2. Furthermore, the membrane hoop tension at the lower edge of the shell was reduced from 11.05N/mm^2 to a value of 10.64N/mm^2 (Zingoni, 2001).

2.2.1.4 Buckling and stability studies

The study by Zhang et al. (2021) on the buckling performance of egg-shaped shells fabricated through free hydroforming has shown that hydroformed shells exhibit adequate buckling capacity when subjected to hydrostatic pressure. However, achieving concentricity during fabrication of conical sections became a challenge, and advised that the challenge may be addressed by designing the egg-shaped shells in the meridional direction.

Zhang et al. (2018) conducted a study on the buckling of externally uniformly pressurised egg-shaped shells with variable and constant wall thickness; in this study, they found that the shells of revolution with variable thickness performed better than the constant wall thickness shells in resisting buckling disturbances. Furthermore, this investigation shows that the average collapse pressure for the surfaces with variable thickness was about 24% higher than that of the constant thickness, which offers an improved buckling capacity.

Zhang et al. (2017b) studied the effect of varying the ratio *B/L* under uniform (similar to *D/H* in Figure 2-4 when subjected to uniform external pressure $p=1MPa$. In this study, fourteen egg-shaped shells were numerically and experimentally studied. The wall thickness and mass were kept constant through the experiment. The results indicated that, as the ratio *B/L* increased, a decrease in buckling capacity was observed. The nonlinear buckling analysis further showed that the shells were very sensitive to imperfections. This was observed through a significant decrease in critical buckling load as the imperfection size increased.

Egg-shaped pressure hulls were found to perform better in resisting applied forces when compared with the equivalent spherical pressure hull considering the hull strength, buoyancy reserve, and space efficiency and therefore the egg-shaped pressure hulls are recommended for future developments in deep-sea manned submersibles (Zhang et al., 2017a).

2.2.1.5 FEM modelling and experimental studies

Zhang et al. (2021) obtained consistent results while validating the numerical results with experimental results on shells fabricated using free hydroforming. Hydroformed shells subjected to low pressures deformed non-axisymmetrically by showing dimples on the experimental studies. A good agreement between experimental results and numerical results were obtained when assessing the effect of varying the wall thickness of a shell structure under uniform external pressure (Zhang et al., 2018) On a study by Zhang, Wang, Wang & Tang (2017) consistency of analytical results with numerical analysis results was achieved. This shows that a well calibrated numerical model yields useful results.

2.2.2 Spherical vessel

The spherical vessel mid-surface is entirely defined by the radius *a*, and the angle ϕ at any point on the surface, as shown in Figure 2-6. The vessel may either contain water or gas with the unit weight γ (N/m^3) (Flügge, 1960).

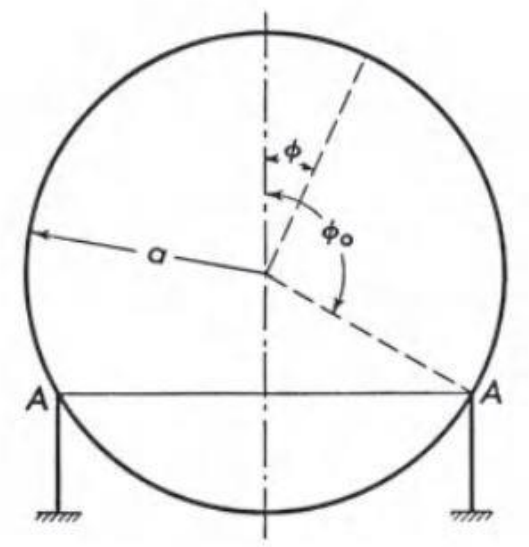

Figure 2-6:Elevated spherical vessel(Flügge, 1960)

2.2.2.1 Shell geometry and optimization

Ali (2018) used a Level set shape optimization method to minimise the weight of offshore spherical tank supports. Topology optimization was used to design the spherical tank supports due to its ability to effectively produce novel, non-anticipated designs that focus on certain functionalities (Ali, 2018). The compliance optimisation function was chosen as the objective function, which was minimised during the optimisation process. As a result, the stiffness of the supports was maximised. The compliance-based design increased the design stiffness compared to the stress-based functions (Ali, 2018).

2.2.2.2 Stress analysis

Flügge (1960) derived the membrane stress resultants for the elevated spherical vessel supported on vertical columns based on the general membrane theory of shells. The membrane meridional stress resultant and the hoop stress resultant for the region $0 < \phi < \phi_0$ is given by equation 2-30 and equation 2-31, respectively (Flügge, 1960).

$$N_\phi = \frac{\gamma a^2}{6}\left(\frac{1-cos\phi}{1+cos\phi}\right)(1+2cos\phi) \qquad \textbf{2-30}$$

$$N_\theta = \frac{\gamma a^2}{6}\left(\frac{1-cos\phi}{1+cos\phi}\right)(5+4cos\phi) \quad \textbf{2-31}$$

The bottom part of the spherical vessel, which is below the horizontal circle at the support defined by $\phi = \phi_0$ takes a different form of membrane stress resultants. The result at $\phi = \pi$, N_ϕ is finite, leading to equations 2-32 and 2-33 for membrane meridional stress resultant and hoop stress resultant in the region $\phi_0 < \phi < \pi$ respectively (Flügge, 1960).

$$N_\phi = \frac{\gamma a^2}{6}\left(\frac{5-5cos\phi+2cos^2\phi}{1-cos\phi}\right) \quad \textbf{2-32}$$

$$N_\theta = \frac{\gamma a^2}{6}\left(\frac{1-7cos\phi+4cos^2\phi}{1-cos\phi}\right) \quad \textbf{2-33}$$

At the support location, there is discontinuity, and the difference in the meridional stress resultant applied to the shell ring beam is resolved into the vertical component given by equation 2-34. The horizontal component is given by equation 2-35, resulting in compressive hoop stress in the ring (Flügge, 1960).

$$\frac{2\gamma a^2}{3sin\phi_0} \quad \textbf{2-34}$$

$$\frac{2\gamma a^2}{3}\left(\frac{cot\phi_0}{sin\phi_0}\right) \quad \textbf{2-35}$$

2.2.2.3 Junction problems

According to Zingoni (2018:257), at the support junction, the location of the vertical supports of the liquid-filled spherical vessel causes the bending effects at the support. The proposed location of the supports with minimal bending effects is the equator of the vessel (Zingoni, 2018:267). In addition, the inclination of the supports may further minimise the bending effects. Furthermore, an increased depth of the column section in the direction towards the axis of revolution of the shell also minimizes the bending effects, which now meet the shell tangentially below the equator (Zingoni, 2018:265).

Zingoni (2018:262) gave expressions for the solutions for the variation of total stresses (membrane + bending) and deformations for the spherical vessel with respect to the distance from the support, just above and below the support location. To link the bending theory and the membrane theory, the application of the kinematic conditions of continuity between the region

of the shell just above the ring-beam and the region just below the ring-beam by introducing boundary conditions governing edge corrections (Zingoni & Pavlovic, 1991).

Zingoni & Pavlovic (1993:409) studied the effect of local shell thickening and quantifying the discontinuity stresses in the vicinity of the supports. Therefore, reference must be made to Figure 2-7 for the regions where the stress resultants are valid.

For regions 1 and 2 in Figure 2-7, the membrane stress resultants are given by:

$$N_{\phi}^{m} = \frac{\gamma a^2}{6}\left(\frac{1}{sin^2\phi}\right)\{1 - 3cos^2\phi + 2cos^3\phi\} \quad \textbf{2-36}$$

$$N_{\theta}^{m} = \frac{\gamma a^2}{6}\left(\frac{1}{sin^2\phi}\right)\{5 - 6cos\phi - 3cos^2\phi + 4cos^3\phi\} \quad \textbf{2-37}$$

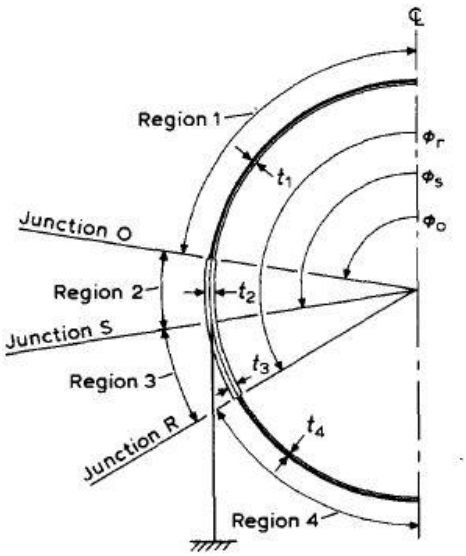

Figure 2-7:shell thickening geometrical parameters at junctions(Zingoni & Pavlovi6, 1993)

For regions 3 and 4, the membrane stress resultants are given by:

$$N_{\phi}^{m} = \frac{\gamma a^2}{6}\left(\frac{1}{sin^2\phi}\right)\{5 - 3cos^2\phi + 2cos^3\phi\} \quad \textbf{2-38}$$

$$N_{\theta}^{m} = \frac{\gamma a^2}{6}\left(\frac{1}{sin^2\phi}\right)\{1 - 6cos\phi - 3cos^2\phi + 4cos^3\phi\} \quad \textbf{2-39}$$

The change in thickness at junction *O* and junction *R* resulted in deformations at the edges of junctions *O* and *R*. For derivations and solutions obtained for the deformations, refer to (Zingoni & Pavlović, 1993:411). Zingoni, Mokhothu & Enoma (2015) studied the behaviour of multi-segmented spherical vessels for high liquid containment. At each segment-segment interaction, bending disturbances introduced at the junction were accounted for by an axisymmetric bending theory for spherical shells (Zingoni, Mokhothu & Enoma, 2015).

2.2.2.4 Buckling and stability studies

Flügge (1960:477) studied the elastic-buckling behaviour of the spherical vessel under external uniform pressure *p*. The solution for the critical buckling pressure is given by equation 2-40.

$$p_{cr} = \frac{2Et^2}{\sqrt{3(1-v^2)a^2}} \qquad \textbf{2-40}$$

Where,

E is Young's modulus of elasticity
v is the Poisson's ratio
a is the radius of the spherical vessel

2.2.2.5 FEM modelling and experimental studies

Petrović et al. (2015) outline the importance of experimental validation of FEM results. The FEM results rely on various factors such as mesh density, the type of FEM mesh, boundary conditions, and proper constraints; therefore, validation must be done to ensure the accuracy of the FEM results. They further indicate that if a high-level correspondence of results from analytical results, FEM results and experimental results is achieved, safety standards are also met.

At the support location, the maximum values of equivalent stresses were obtained through the FEM analysis. Figure 2-8 shows the equivalent stress distribution on the surface of the steel spherical tank subjected to self-weight and the hydrostatic pressure modelled using FEM. The analysis was performed using FEM analysis. The stress concentrations at the support-vessel contact point could lead to the tank's failure due to high stresses acting on a tiny area. These stresses were also higher than the yield stress of the steel material used to construct the surface (Petrović et al., 2015).

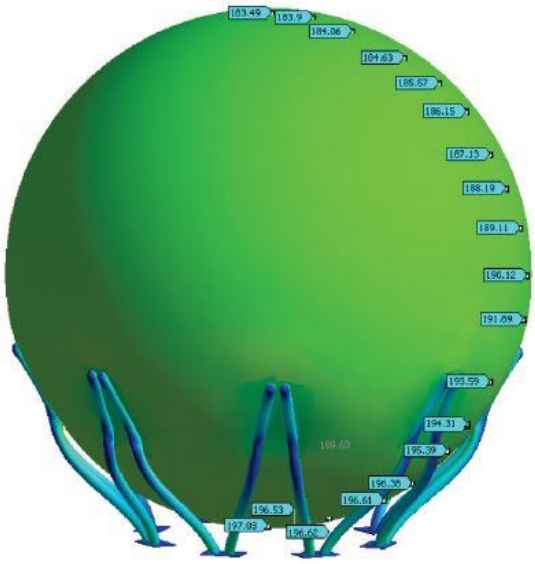

Figure 2-8:Equivalent stresses on the spherical steel tank (Petrović et al., 2015)

The experiment was performed by subjecting the spherical vessel to hydrostatic pressure, and measurements of stresses were carried out at seven measuring points. Twenty-one strain gauges were set-up at those seven stress measuring points, as shown in Figure 2-9. The measuring equipment used for the experiment was the HBM UPM 100.

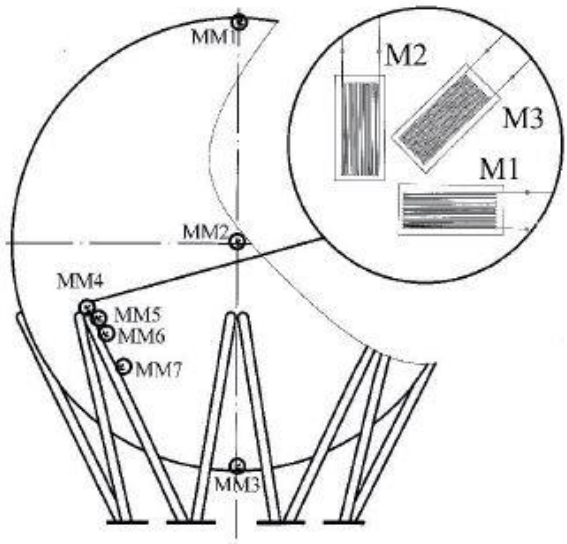

Figure 2-9:Experimental setup showing measuring points(Petrović et al., 2015)

Petrović et al. (2015) also present some findings on the accuracy of the FEM results versus the analytical results by comparing them with the experimental results. FEM results showed a better deviation from the experimental results at all seven locations on the surface measured for stress. The maximum error was 8.1 percent at the MM4 location, which is at support-to-support

interaction, as seen in Figure 2-9. In the study by Zingoni, Mokhothu & Enoma (2015), very accurate results were obtained while validating the closed-form analytical solutions using FEM. Hence FEM solutions derived from that study may be reliably used. Furthermore, aurate results can be obtained and used to validate the finite-element programmes (Zingoni, Mokhothu & Enoma, 2015).

2.2.3 Ellipsoidal vessel

Shells with an ellipsoidal surface geometrical form have different industrial applications as internally pressurised vessels, domes, and tanks. When used as tanks, ellipsoidal shells form a shell of revolution, which can be formed by rotating an ellipse about the vertical axis, generally defined as the z-axis, to create a surface of revolution. An ellipsoidal shell of revolution is a positive gaussian surface because the maximum and minimum radii of curvature lie on the same side of the meridian. The details of the different ellipsoidal geometrical forms as shells of revolution are described in (Krivoshapko 2007). Figure 2-10 shows the two different types of the ellipsoidal shell of revolution.

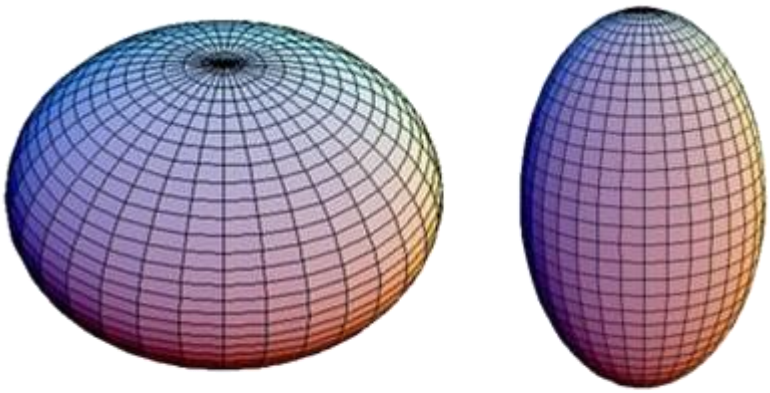

a) Oblate spheroid b) Prolate spheroid

Figure 2-10: Types of ellipsoidal shells (https://www.web-formulas.com/Math_Formulas/Geometry_Surface_of_Ellipsoid.aspx,n.d)

The geometry of the spherical vessel is defined by equation 2-41.

$$\frac{x^2}{a^2}+\frac{y^2}{b^2}=1 \qquad \textbf{2-41}$$

2.2.3.1 Shell geometry and optimisation

A thorough search of the literature was conducted for this aspect. Unfortunately, nothing was found. Thus future work may be done on this aspect.

2.2.3.2 Stress analysis

The stress analysis based on the membrane theory for shells of revolution of the elliptic profile has been derived by (Zingoni, 2018:86). In this work, both the meridional stress and hoop stress equations are derived for the continuous membrane surface. Zingoni (2018:86) also evaluates the applicability of these equations at the pole location since the equations may be inappropriate at the pole. Both maximum and minimum radii of curvature r_1 and r_2 tend to have a finite value at the pole for the elliptic profile. Furthermore, the rates of change of both maximum and minimum radii of curvature tend to be zero at the pole, which validates the membrane solution's applicability at any point on the membrane, including at the supports (Zingoni, 2018:91).

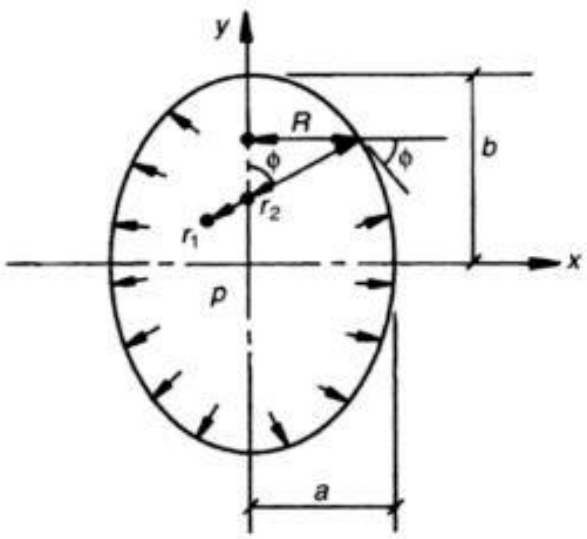

Figure 2-11:Geometrical parameters of an ellipsoidal vessel(Zingoni, 2018:61)

The membrane meridional and hoop stress resultant solutions for the ellipsoidal vessel subjected to internal pressure *p* are given by (Zingoni, 2018:89).

$$N_\phi = \frac{pa^2}{2}\,\frac{1}{(a^2 sin^2\phi + b^2 cos^2\phi)^{1/2}} \qquad \textbf{2-42}$$

$$N_\phi = \frac{pa^2}{2b^2}\frac{b^2 + (b^2 - a^2)sin^2\phi}{(a^2sin^2\phi + b^2cos^2\phi)^{1/2}} \quad \textbf{2-43}$$

Equation 2-43 and equation 2-44 give the hoop stress resultant for the prolate and oblate spheroidal vessels, as seen in Figure 2-10 for both shapes.

$$N_\phi = \frac{pa^2}{2b^2}\frac{b^2 - (b^2 - a^2)sin^2\phi}{(a^2sin^2\phi + b^2cos^2\phi)^{1/2}} \quad \textbf{2-44}$$

The particular case of an ellipsoid of revolution is a unique vessel with geometrical parameters *a* and *b* equal. As a result, the radii of curvature r_1 and r_2 become equal. Thus, the derivation is not as complex as for the elliptic profile. Zingoni (2018:72) derived the membrane stress resultants equations for the spherical vessel. This work showed that the membrane rotation *V* at the support is the same for an upper and lower level of the vessel, while for the displacement δ, that was not the case, and thus, bending disturbances had to be corrected.

2.2.3.3 Junction problems

In a review paper by Krivoshapko (2007), a junction at a cylinder-ellipsoid connection exists for the reservoirs with ellipsoidal bottoms. The stress concentration was noted at this point. As a result, the continuity of the surface is violated, and bending stresses exist at the junction. The stress state was accounted for by considering a boundary effect at the intersection.

2.2.3.4 Buckling and stability studies

The ratio of *b/a* characterises the buckling behaviour of the ellipsoidal shell of revolution when subjected to high internal pressure, provided the body is thin enough. The local buckling phenomenon occurs when the ratio of *b/a* is less than ½ (Zingoni, 2018:386-388).

The critical buckling pressure of the spheroidal vessel decreases rapidly as b rises above a. Corrections for the critical buckling pressure are necessary for the spheroidal vessel. As a result, knock-down factors are used to correct the theoretical values as they have been found to deviate significantly from the realistic values (Zingoni, 2018:386-388).

Barathan & Rajamohan (2022) studied the non-linear buckling analysis of a semi-elliptical steel dome subjected to uniform hydrostatic loading. This study found that the dome is sensitive to buckling at the apex. Affine imperfections were imposed on the structure, and it was found that an increase in imperfection amplitude decreases the critical buckling load. In

addition, an increase in aspect ratio (h/R) was found to improve the buckling resistance of the shell.

Li et al. (2019) studied the buckling behaviour of large-scale thin-walled ellipsoidal heads under internal pressure. They found that the decrease in radius-to-height ratio increases buckling pressure. There is an agreement in the argument by (Barathan & Rajamohan, 2022) and (Li et al. (2019) on the effect of the height-to-radius ratio on buckling load; the more prolate form the ellipsoid structure takes, the better it resists buckling.

2.2.3.5 FEM modelling and experimental studies

Barathan & Rajamohan (2022) conducted experimental studies. They also used the FEM program ANSYS to investigate the non-linear behaviour of a semi-ellipsoid subjected to hydrostatic pressure. A 4-node shell element was selected for the ANSYS software to conduct the analysis. As a result, a reasonable agreement of results between the experimental and the finite-element method was found. Furthermore, the eigenvalue buckling analysis overestimated the critical buckling pressures when comparing essential loads obtained from a non-linear buckling analysis and experimental studies since imperfections are not accounted for in the linear buckling analysis.

Subramani & Sugathan (2012) investigated the buckling behaviour and an ellipsoidal shell using FEM packages ANSYS and LS-DYNA. A top-down approach was used to create the cylindrical and elliptical members and then meshed with a 4-node element using Shell63 and Shell43 finite-element types in elastic and plastic ranges, respectively. A linear eigenvalue and a nonlinear buckling analysis were conducted. A recommendation for nonlinear analysis to obtain actual buckling load was made in the study due to the high stresses obtained in the linear domain due to not accounting for geometrical imperfections.

The experimental study reported in the review article by Krivoshapko (2007) on the ellipsoidal shell was said to have agreed with the theoretical methods of 85% of the conducted experiments on aluminium material, giving confidence in the use of the derived theoretical methods.

In this section, all the authors agree on the issue of the linear buckling analysis overestimating the buckling pressure. However, the actual buckling pressure on the vessel may be obtained by conducting a nonlinear buckling analysis.

2.2.4 Arbitrary profiles

In this section, only the stress analysis is covered. No other relevant aspects have been reported in the existing literature and are still open for further research. The membrane solutions of elevated shell-of-revolution tanks of arbitrary meridional profiles were first studied by Zingoni (1995). The geometrical shapes explored in this study are (i) the parabola, (ii) the cosh function, (iii) the cubic function, and (iv) the ellipse.

The study was novel on those geometrical profiles for application as liquid containment vessels. The mentioned profiles meet all the requirements for using the membrane theory for the stress analysis of shells throughout the surface but not including the pole location. Furthermore, these shells have zero slopes at the pole, continuously increasing as the height of the surface increases, forming a bowl-like profile. As a result, they were recommended for use in the application as containment vessels. Figure 2-12 shows the geometric parameters of a shell of revolution that forms a profile of an arbitrary shape (Zingoni, 1995). The complete derivation of the results presented in Sections 2.2.4.1 to 2.2.4.4 may be seen in Zingoni (1995). These are also given in Zingoni's book (2018).

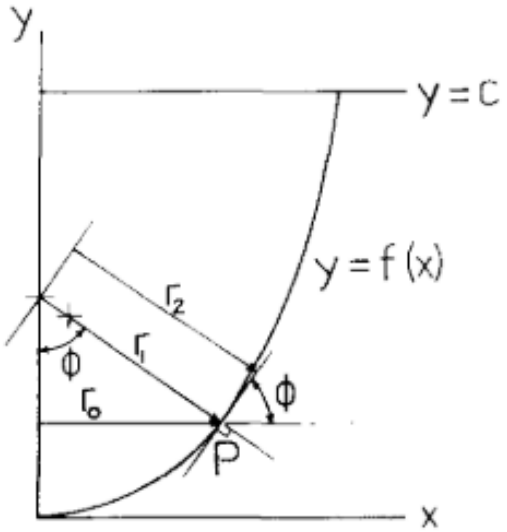

Figure 2-12:Geometric parameters of an arbitrary meridian surface of revolution [reproduced(Zingoni, 1995)]

2.2.4.1 Parabolic profile

The meridional profile of this surface of revolution follows a function of $f(x) = kx^2$ given that $x \geq 0$. The membrane stress resultants solutions were obtained from the membrane theory of shells presented in the study by Zingoni (1995).

$$N_\phi = \frac{\rho}{8}(1+4k^2x^2)^{\frac{1}{2}}(2{x_H}^2 - x^2) \quad \textbf{2-45}$$

$$N_\theta = \frac{\rho}{8}(1+4k^2x^2)^{\frac{1}{2}}\left\{4(x_H^2 - x^2) - \frac{2x_H^2 - x^2}{1+4k^2x^2}\right\} \quad \textbf{2-46}$$

2.2.4.2 Cosh profile

Cosh profile follows the function *f(x)* = *k* (cosh *x* - 1) given that $x \geq 0$, the meridional and hoop stress equations are given in equations 2-47 and 2-48.

$$N_\phi = \frac{\rho}{2}\frac{(1+k^2\,sinh^2\,x)^{\frac{1}{2}}}{x\,sin\,hx}\{x^2\,cosh\,x_H - 2x\,sinh\,x + 2(\cosh x - 1)\} \quad \textbf{2-47}$$

$$N_\theta = \frac{\rho}{2}\frac{(1+k^2\,sinh^2\,x)^{\frac{1}{2}}}{\sinh x}\Big\{2x(cosh\,x_H - \cosh\,x) - \frac{\coth x}{1+k^2sinh^2x}\{x^2cosh\,x_H - 2\sinh x + 2(\cosh x - 1)\}\Big\} \quad \textbf{2-48}$$

2.2.4.3 Cubic profile

The meridional and hoop stress resultant equations for the cubic profile are given by equations 2-49 and 2-50.

$$N_\phi = \frac{\rho}{10}\frac{(1+9k^2x^4)^{\frac{1}{2}}}{3x}(5x_H^3 - x^3) \quad \textbf{2-49}$$

$$N_\theta = \frac{\rho}{10}\frac{(1+9k^2x^4)^{\frac{1}{2}}}{3x}\left\{10(x_H^3 - x^3) - \frac{2}{1+9k^2x^4}(5x_H^3 - x^3)\right\} \quad \textbf{2-50}$$

2.2.4.4 Elliptic profile

Equations 2-51 and 2-52 give the meridional and hoop stress resultants.

$$N_{\phi} = \rho \frac{\{(b^2-a^2)x^2+a^4\}^{1/2}}{6ax^2}\{2\{a^3-(a^2-x^2)^{3/2}\}-3x^2(a^2-x_H^2)^{1/2}\} \quad \textbf{2-51}$$

$$N_{\theta} = \rho \frac{\{(b^2-a^2)x^2+a^4\}^{1/2}}{6ax^2}\left\{6x^2\{(a^2-x^2)^{1/2}-(a^2-x_H^2)^{1/2}\}-\right. \quad \textbf{2-52}$$

$$\left.\frac{a^4}{(b^2-a^2)x^2+a^4}\{2\{a^3-(a^2-x^2)^{3/2}\}-3x^2(a^2-x_H^2)^{1/2}\}\right\}$$

The other finding from the arbitrary profiles is that the cubic vessel violates the membrane hypothesis at the pole. Therefore, the membrane hypothesis is unsuitable at the pole (Zingoni, 1995). Only the stress equations have been developed for these profiles; other aspects of analysis, such as buckling and stability, may still be explored on the different arbitrary profile surfaces of the revolution and are still open for future research.

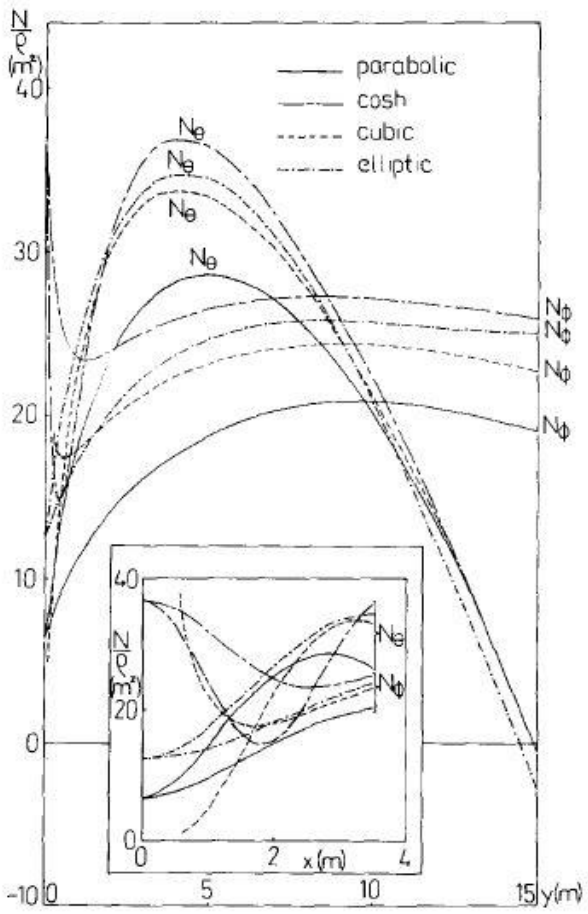

Figure 2-13:Variation of membrane stress resultants with coordinate y for the four numerical cases. (variation with respect to coordinate x, for the insert, for the lower portions of the tanks) (Zingoni, 1995)

2.3Negative Gaussian curvature shells

2.3.1 Circular toroidal shells

2.3.1.1 Shell geometry and shape optimization

Vu (2015) studied minimum weight design for toroidal shells with a strengthening component for circular toroidal shells. The optimum shell shape was found by adjusting geometry and wall thickness. The study was conducted using Differential Evolution and Particle Swarm Optimization. He found that the former method outshines the latter in most

cases investigated. The constraints of the optimization study included first yield pressure, plastic pressures, plastic instability pressure and internal volume of the toroid.

The maximum material saving from the study by Vu (2015) was found to be 70.69%, for the ratio of R_0/r_0 =1.25 in case 1, refer to Figure 2-14. The material saving was also significant for the loading constraint type Y (the elastic state, first yield). The other interesting result from the study is that doubling the ratio of R_0/r_0 reduces material saving by over 50%, and the ratio of material savings varied from 6 to 9. Future recommendation from the study by Vu (2015) shows that the optimized shape and geometry of the toroidal vessel, which are the web-strengthening components, can be developed for further research based on the approach he used. As a result, the aim of material saving was obtained.

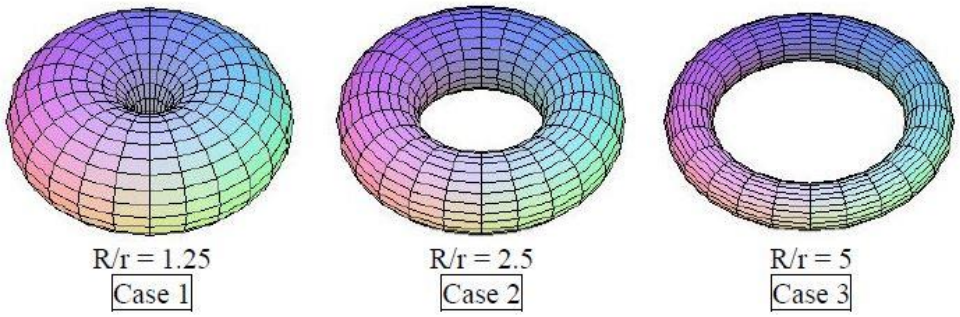

Figure 2-14:shapes of benchmark toroids for optimization (Vu, 2015)

2.3.1.2 Stress analysis of the shell

Closed-form analytical solutions are developed based on two theories, the membrane theory and the bending theory of shells. On the other hand, membrane theory gives insights into the approximate state of stress in the shell. As a result, closed-form membrane solutions are always a good starting point for the designer to understand what to expect for the total stresses.

Flügge (1960) derived closed-form analytical solutions for membrane meridional and hoop stress resultants of a circular toroid subjected to uniform pressure *p* using the membrane theory of shells. Enoma N et al. (2015) derived closed-form analytical solution equations for the membrane meridional and hoop stress resultants in the circular toroid when subjected to hydrostatic loading.

Figure 2-15 shows the geometrical parameters used while deriving the closed-form membrane solutions for a circular toroidal vessel.

For the upper-outer region, where $0 < \emptyset < \pi/2$, the membrane meridional stress and hoop stress resultant solutions are given by equations 2-53 and 2-54.

$$(N_{\emptyset})_1{}^{o} = \frac{\gamma a^2}{6sin\emptyset(A + asin\emptyset)}\{a(1 + (-3 + 2cos\emptyset)cos^2\emptyset) - 3A(\emptyset + (-2 + \cos\emptyset)\sin\emptyset)\} \quad \textbf{2-53}$$

$$(N_{\theta})_1{}^{o} = \frac{\gamma a}{6sin^2\emptyset}\left\{4a(5 + 4cos\emptyset)sin^4\left(\frac{\emptyset}{2}\right) + 3A(\phi - cos\emptyset\sin\emptyset)\right\} \quad \textbf{2-54}$$

For the lower-outer region, where $\pi/2 < \emptyset < \pi$, the membrane meridional and membrane hoop stress resultant solutions are given by equations 2-55 and 2-56.

$$(N_{\emptyset})_2{}^{o} = \frac{\gamma a^2}{6sin\emptyset(A + asin\emptyset)}\{a(5 + (-3 + 2cos\emptyset)cos^2\emptyset) + 3A(\pi - \emptyset - (-2 + \cos\emptyset)\sin\emptyset)\} \quad \textbf{2-55}$$

$$(N_{\theta})_2{}^{o} = -\frac{\gamma a^2}{12sin^2\emptyset}\{a(1 + 6cos\phi + 3cos2\phi - 2cos3\phi + 6A(\pi - \phi + cos\phi sin\phi)\} \quad \textbf{2-56}$$

The membrane meridional and hoop stress resultants solutions for the upper-inner region are given by equations 2-57 and 2-58.

$$(N_{\emptyset})_1{}^{i} = \frac{\gamma a^2}{6sin\emptyset(A - asin\emptyset)}\{a(1 + cos\emptyset)^2 + 3A(-\pi + \phi + (2 + cos\phi)sin\phi)\} \quad \textbf{2-57}$$

$$(N_{\theta})_1{}^{i} = -\frac{\gamma a}{6sin^2\emptyset}\left\{4a(-5 + 4cos\emptyset)cos^4\left(\frac{\emptyset}{2}\right) + 3A(\pi - \emptyset - cos\emptyset\sin\emptyset)\right\} \quad \textbf{2-58}$$

Lastly, the membrane meridional and membrane hoop stress resultant solutions for the lower-inner region are given by equations 2-59 and 2-60.

$$(N_{\emptyset})_2{}^{i} = \frac{\gamma a^2}{6sin\phi(A - asin\phi)}\{a(-5 + (3 + 2cos\emptyset)cos^2\emptyset) + 3A(\emptyset + (2 + \cos\emptyset)\sin\emptyset)\} \quad \textbf{2-59}$$

$$(N_{\theta})_2{}^{i} = -\frac{\gamma a}{12sin^2\phi}\{a(1 - 6cos\phi + 3cos2\phi + 2cos3\phi + 3A(-2\phi + 2sin3\phi)\} \quad \textbf{2-60}$$

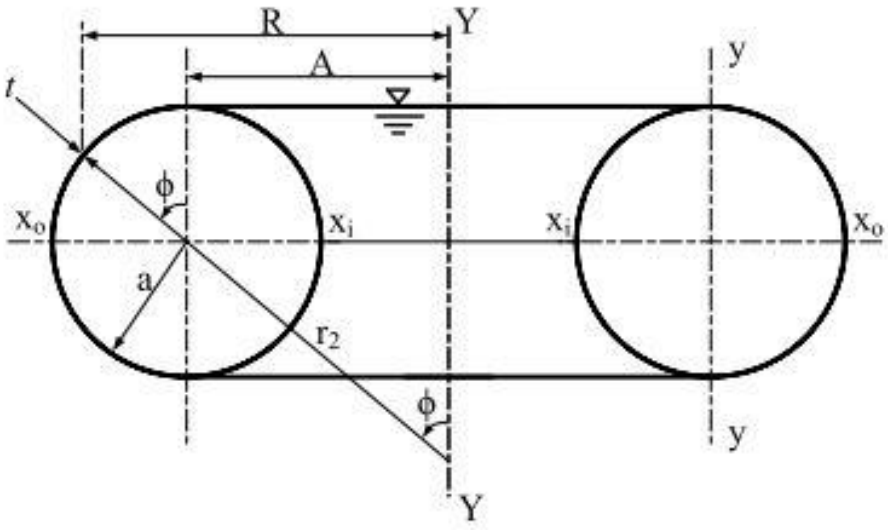

Figure 2-15:Geometrical parameters of a circular toroid subjected to internal hydrostatic pressure (Enoma N et al., 2015)

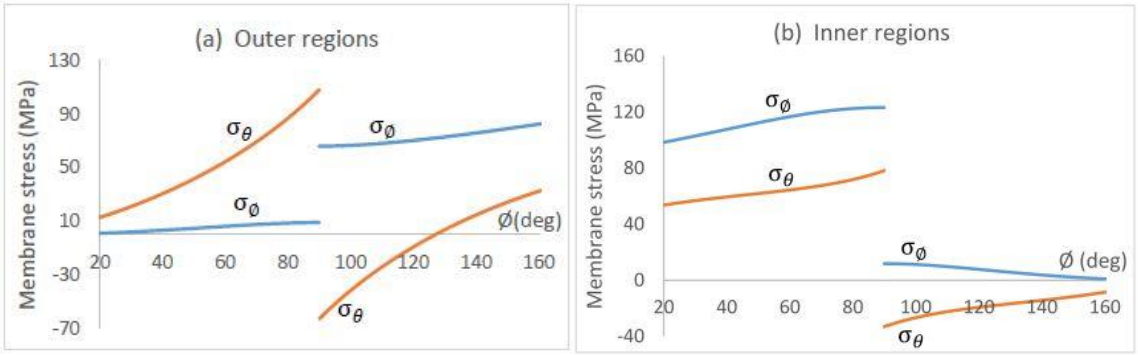

Figure 2-16:Variations of membrane stresses on the inner and outer regions of the circular toroid with angular parameter ∅ (Enoma N et al., 2015)

From Figure 2-16, the graphs only show stresses in regions where membrane theory is applicable, that is, in regions where there are no bending disturbances which is in the range $20° < \phi < 160°$. As the value of ϕ increases, in the outer-upper region, the tensile (hoop) stresses increase rapidly, while the meridional stresses increase gradually. In the inner-upper region, the meridional and hoop stresses increase gradually as the value of ϕ increases. It can also be seen that maximum hoop stresses occur in the outer-upper region, while the maximum meridional stresses occur in the inner-upper region of a toroidal vessel. The vessel is a steel plate with Young's modulus $E = 200 \times 10^9 N/m^2$ and Poisson ratio of $v = 0.3$ (Enoma N et al., 2015).

Vu (2015) conducted a study on optimisation looking at the minimum weight design of a toroidal vessel and found that the ratio of maximum von misses stress is highly influenced by

the ratio of R/r, and the stresses are maximum on the inner surface of the toroidal vessel. Therefore, the smaller R/r ratio vessel gives the best optimal cross-section. The geometrical parameters can be seen in Figure 2-15 Figure 2-15:Geometrical parameters of a circular toroid subjected to internal hydrostatic pressure (Enoma N et al., 2015).

2.3.1.3 Junction problems

The analytical solution gives the best approximation of the state of stress in the toroidal shell subjected to the internal hydrostatic pressure throughout the surface of the shell, excluding zones surrounding the support or where there are discontinuities in the shell. An example is at the vicinity of the top and bottom circles of latitude, and this is due to bending stresses induced due to discontinuities at these zones (Enoma N et al., 2015).

2.3.1.4 Buckling and stability studies

Galletly & Blachut (1995) investigated the stability of complete circular and non-circular toroidal shells subjected to external uniform pressure. They found that Jordan's closed-form elastic buckling equation (equation 2-61) shows an excellent agreement with the numerical results of BOSOR 5 software. The equation is therefore recommended for use by designers for perfect circular toroidal shells. Reference must be made from Figure 2-15 for the geometrical parameters *r, t, and R* in equation 2-29. *E* is Young's modulus, and for Poison's ratio, *v=0.3* is used in the equation. Figure 2-17 shows sample buckling modes for the circular toroids.

$$P_{cr} \approx 0.185E\left(\frac{t}{r}\right)^{7/3}\left(\frac{r}{R}\right)^{2/3} \qquad \textbf{2-61}$$

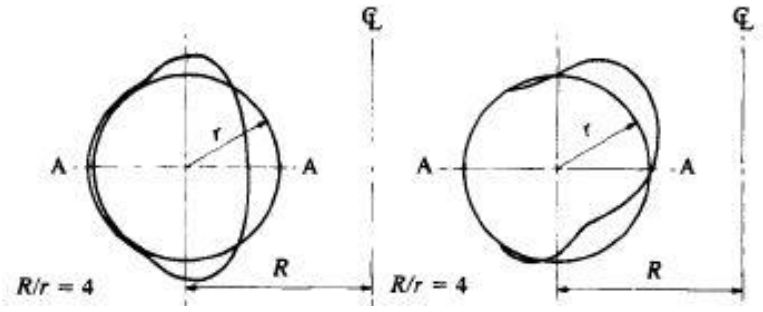

Figure 2-17:Sample buckling modes for circular toroid(Galletly & Blachut, 1995)

2.3.1.5 FEM modelling and experimental studies

Vu (2015) used ABAQUS software for the stress analysis of the toroidal vessel subjected to internal pressure. ABAQUS is a Finite Element Method programme used for analysing complex structural analysis problems. The geometry and loading of the shell were symmetric

about the vertical axis of the shell. As a result, the choice of the finite element type was made SAX2, a 2-Dimensional axisymmetric shell element (Purdel & Stere, n.d.).

Adachi & Benicek (1964) examined the buckling behaviour of a torispherical vessel subjected to internal fluid pressure using experiments. The models were constructed using polyvinyl chloride material with a base diameter of 10.52 inches. Observations were made on the thickness, central angle and toroidal radius. The models were assumed to behave in a linear-elastic manner. The relationship between the buckling pressure and the wall thickness of the torisphere under internal pressure is given by equation 2-62, and the geometric parameters ϕ and the ratio R_T/D are constant in the equation. The geometrical properties describing the surface of the torisphere are shown in Figure 2-18.

$$\frac{p}{E} = \left(\frac{t}{R_T}\right)^n \qquad \textbf{2-62}$$

Figure 2-19 shows the findings from Adachi & Benicek (1964) on the relationship between the buckling pressure and the torisphere thickness for various bulkhead configurations.

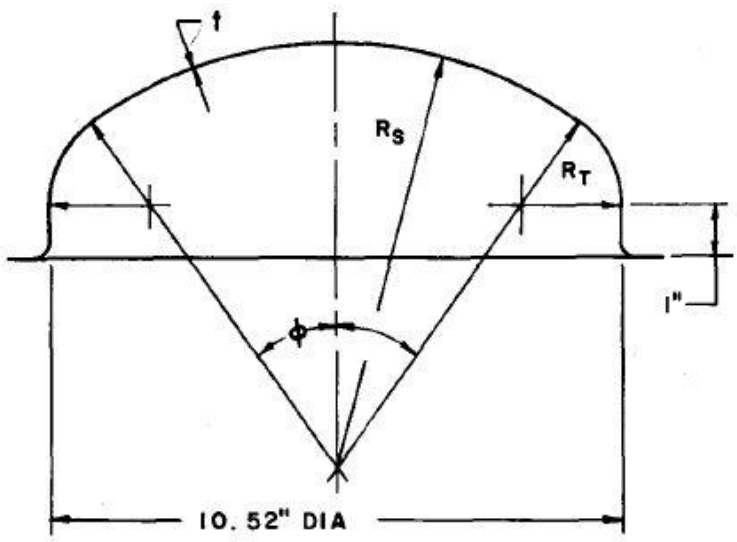

Figure 2-18:Geometrical parameters of the torisphere(Adachi & Benicek, 1964)

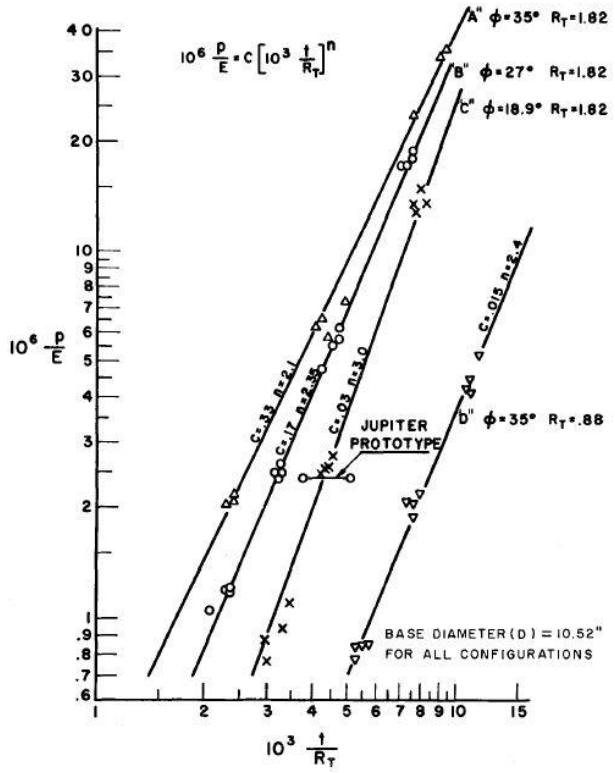

Figure 2-19:Buckling pressure versus thickness for various bulkhead configurations

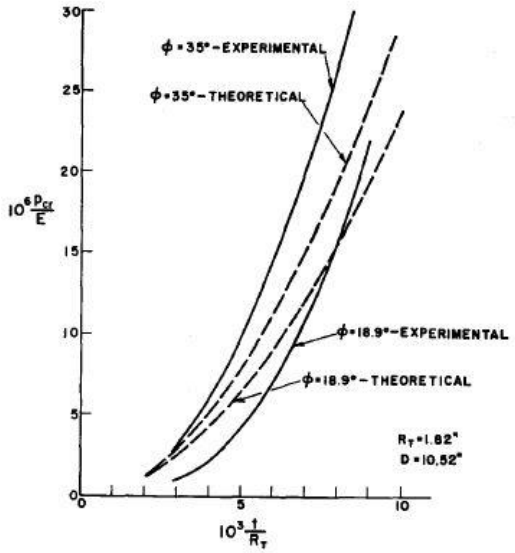

Figure 2-20:Expermental results versus theory(Adachi & Benicek, 1964)

It can also be seen from Figure 2-20 that the theoretical and experimental results are accurate. Adachi & Benicek (1964) also indicated that the change in toroidal radius significantly affects the buckling pressure, but more data is still required to provide precise results. Figure 2-21 shows the initial buckling of the torisphere at critical buckling load p_{cr}.

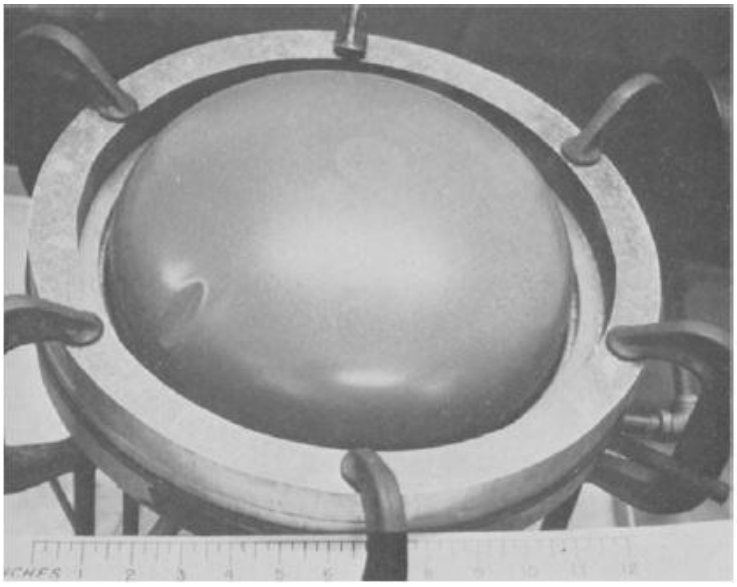

Figure 2-21:Buckling of the torisphere at critical buckling pressure(Adachi & Benicek, 1964)

Jones, Holliday & Larson (1999) compared the experimental test results for the bursting of thin toroidal shells under internal pressure. The experiment and the Finite-element modelling software ABAQUS were the two methods used in this study. The finite-element mesh contained 13 482 eight-node reduced integration quadrilateral elements CAX8R with 41 541 nodes. The experimental and FEM results were in good agreement with each other.

Figure 2-22 shows the variation of applied pressure with toroidal shell diametral dilation on the three-specimen tested at four-hour intervals and the elastic-plastic analysis results. The graph shows that the results from the experiment and the FEM analysis agree. Furthermore, the study shows an error of comparison of less than 5% when comparing the burst pressure from both the experiment and the finite-element analysis and therefore concluded that elastic-plastic FEM analysis can be reasonably accurate to predict the bursting pressure of the toroidal membrane structures (Jones, Holliday & Larson, 1999).

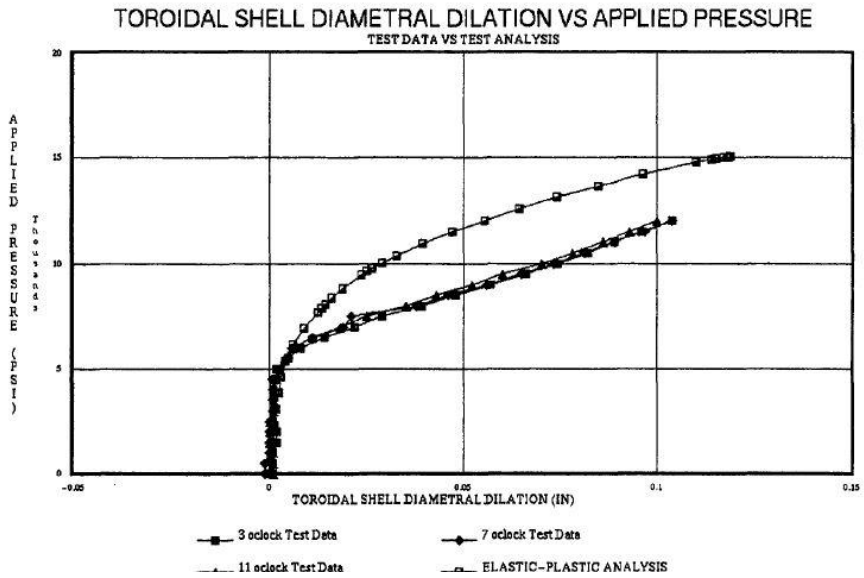

Figure 2-22:experimental results versus FEM analysis results(Jones, Holliday & Larson, 1999)

2.3.2 Elliptical toroidal vessel

The elliptic meridian is defined by the governing equation of the form:

$$\frac{x^2}{a^2}+\frac{y^2}{b^2}=1 \qquad \textbf{2-63}$$

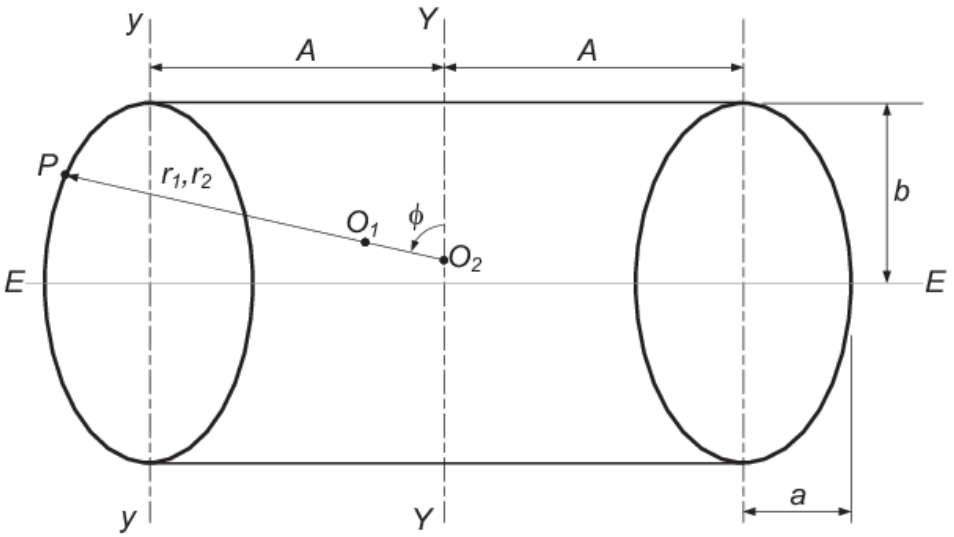

Figure 2-23:Geometry of an elliptic torus(Zingoni, Enoma & Govender, 2015)

2.3.2.1 Shell geometry and shape optimization

No literature was found on this aspect, and a gap for future research is noted.

2.3.2.2 Stress analysis of the shell

Enoma N (2018:92) developed the closed-form analytical solutions for membrane meridional and hoop stress resultants for an elliptic toroidal vessel subjected to hydrostatic pressure based on membrane theory. However, the membrane solutions are not applicable for the locations on the shell with any discontinuities in either geometry, thickness or loading. Figure 2-23 shows the geometrical properties of an elliptical toroidal vessel used to derive the membrane stress resultants. The results below are for hydrostatic loading (Enoma,2018).

$$N_{\phi}^{m} = \frac{\gamma a^2}{6(A+x)sin\phi_c}\left[-\frac{3A}{a\sqrt{a^2-b^2}}\left\{\frac{x_{el_2}}{x_{el_1}}tan^{-1}\left(\frac{b}{x_{el_1}}tan\left(\frac{\phi_c}{2}\right)\right)\right.\right.$$
$$\left.+\frac{x_{el_3}}{x_{el_4}}tan^{-1}\left(\frac{b}{x_{el_4}}tan\left(\frac{\phi_c}{2}\right)\right)\right\}$$
$$+\frac{\sqrt{2}}{x_{el_5}^{\frac{3}{2}}}(4b^3cos^3\phi_c + 3A\{(3a^2+b^2)sin\phi_c + (-a^2+b^2)sin(3\phi_c)\})$$
$$\left.+\frac{3b}{x_{el_5}}\left(\frac{2a^2b}{-a^2+b^2} - Asin(2\phi_c)\right) + \left(\frac{3a^2}{a^2-b^2} - 2\right)\right] \quad \textbf{2-64}$$

$$N_\theta^m = \frac{\gamma x_{el}^3}{6b}\left(\frac{a^2}{x_{el}} + \frac{A}{sin\phi_c}\right)\Bigg[\frac{6b^2}{x_{el}^4}(x_{el} - bcos\phi_c)$$
$$- \frac{x_{el}}{(Ax_{el} + a^2 sin\phi)sin\phi}\Bigg[\frac{3a^2}{a^2 - b^2} - 2$$
$$- \frac{3A}{a\sqrt{a^2 - b^2}}$$
$$\times\left\{\frac{x_{el_2}}{x_{el_1}} tan^{-1}\left(\frac{b}{x_{el_1}} tan\left(\frac{\phi_c}{2}\right)\right) + \frac{x_{el_3}}{x_{el_4}} tan^{-1}\left(\frac{b}{x_{el_4}} tan\left(\frac{\phi_c}{2}\right)\right)\right\}$$
$$+ \frac{\sqrt{2}}{x_{el_5}^{\frac{3}{2}}}(4b^3 cos^3\phi_c + 3A\{(3a^2 + b^2)sin\phi_c + (-a^2 + b^2)sin(3\phi_c)\}) \quad \textbf{2-65}$$
$$+ \frac{3b}{x_{el_5}}\left(\frac{2a^2 b}{-a^2 + b^2} - Asin(2\phi_c)\right)\Bigg]\Bigg]$$

Where:

$$x_{el_1} = \sqrt{2a^2 - b^2 - 2a\sqrt{a^2 - b^2}}$$

$$x_{el_2} = -a^2 + b^2 + a\sqrt{a^2 - b^2}$$

$$x_{el_3} = a^2 - b^2 + a\sqrt{a^2 - b^2}$$

$$x_{el_4} = \sqrt{2a^2 - b^2 + 2a\sqrt{a^2 - b^2}}$$

$$x_{el_5} = a^2 + b^2 + (-a^2 + b^2)cos(2\phi_c)$$

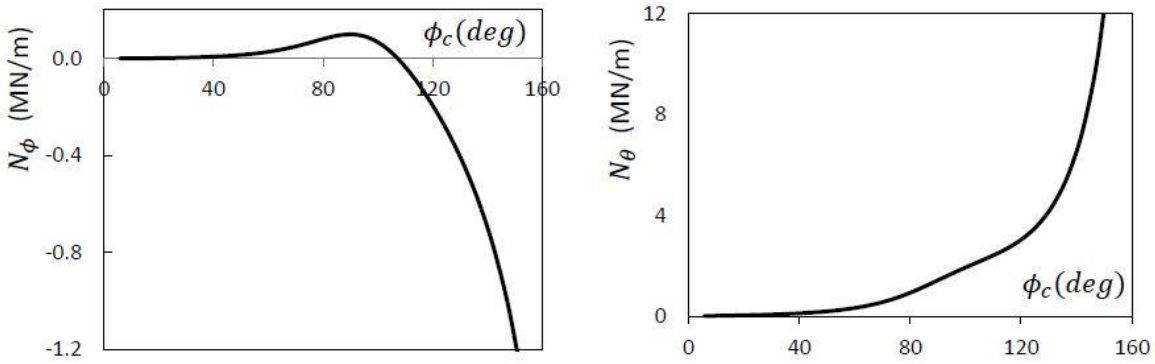

Figure 2-24:Variation of membrane stress resultants with ϕ_c on the outer region of the elliptic toroidal tank (Enoma N, 2018)

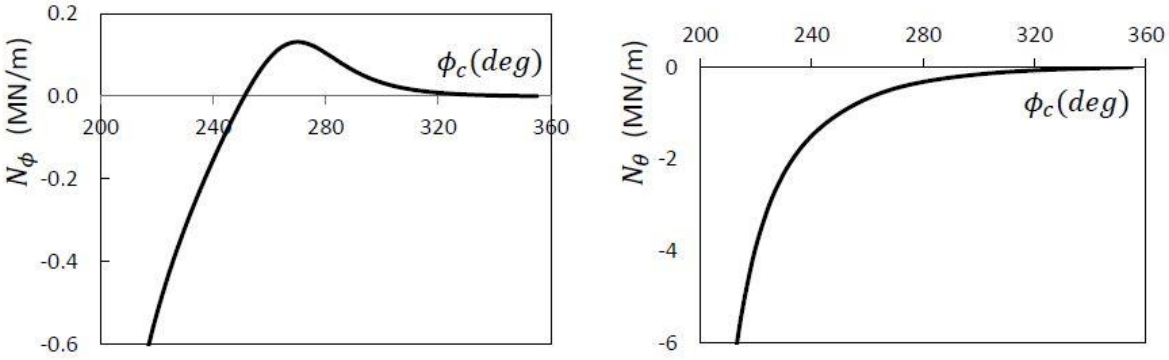

Figure 2-25:Variation of membrane stress resultants with ϕ_c in the inner region of the elliptic toroidal tank (Enoma N, 2018)

Figure 2-24 and Figure 2-25 show the variation of membrane stress resultants on the outer and inner regions of the elliptic toroidal tank with ϕ_c. The meridional stress resultants on the outer and inner regions of the ellipsoidal tank are in tension from the apex, reaching the maximum at the equator. The maximum tensile stress on the inner region is 1.3 times the maximum tensile stress on the outer region of the vessel. The meridional stress decreases from the equator to the compression zone. The hoop stress resultant in the outer region is in full tension, while the hoop stress resultant in the outer region is in full compression (Enoma N, 2018).

The elliptic toroidal tank behaves differently from the circular toroidal tank when it comes to the location of the maximum tensile stresses. Enoma N et al. (2015) showed that for the circular toroidal vessel, the meridional stresses are in full tension throughout the surface on both the inner and outer regions of the vessel. The maximum tensile stress occurs in the outer region of the shell surface, while in the other study, Enoma N (2018) found that the maximum tensile meridional stresses in the elliptic toroidal tank occur in the inner region. As a result,

both shells should be designed differently for their maximum tensile stresses. If the toroid is constructed of concrete, tensile reinforcement should be provided in regions of tensile stresses.

Zingoni (2018:66) studied the behaviour of the elliptical toroidal vessel while subjected to uniform internal pressure *p*. He found that for the elliptical toroidal vessel with $b=a$, the elliptic vessel has the same stress resultants as the ones in the circular toroidal vessel, as seen in Figure 2-20 for the geometric parameters.

2.3.2.3 Junction problems

Sutcliffe (1971) studied the bending behaviour of an elliptical toroid subjected to uniform internal pressure. To achieve the results, he introduced the boundary conditions at the apex of the vessel and the equator, as shown in Figure 2-26. The results of the investigation are shown in Figure 2-27. The results from the investigation show that the maximum bending stresses occur very close to the apex where $\phi = 0°$ and the bending stress in this region is about seven times the maximum bending stress in the circular toroidal vessel (Sutcliffe, 1971).

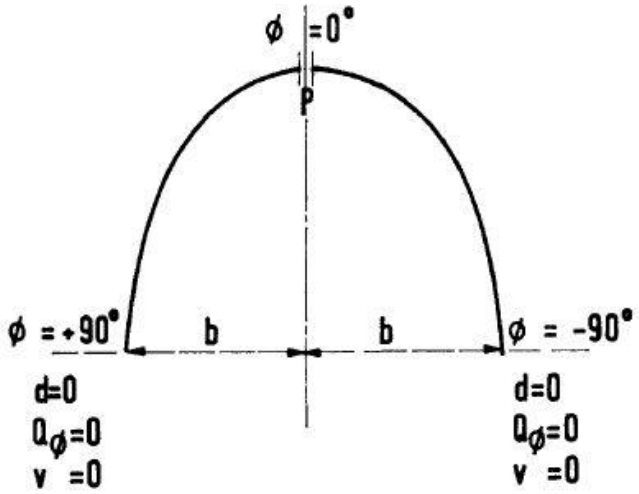

Figure 2-26:Boundary conditions on an elliptic toroid(Sutcliffe, 1971)

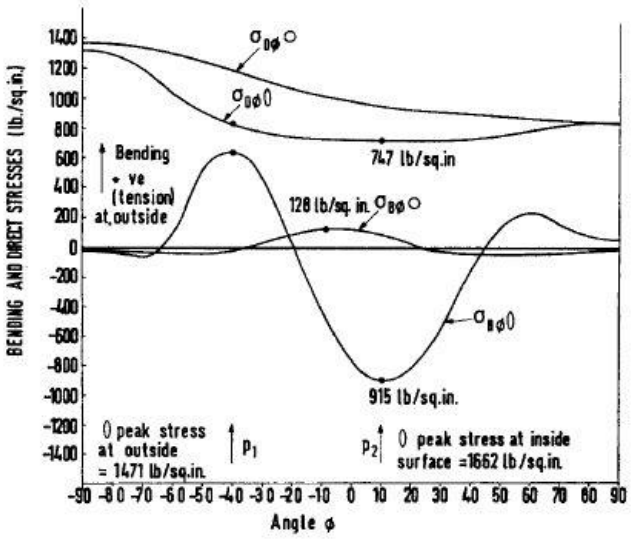

Figure 2-27:Variation of bending and direct stresses with angle ϕ (SutcliffeSutcliffe, 1971)

Zingoni, Enoma & Govender (2015) studied the equatorial bending of an elliptic toroidal shell. They found that by applying the edge moment M_e on the inner and outer edges of the shell, the magnitude of the induced stresses depends only on the thickness of the elliptic toroid and not on the principal radii of curvature. As a result, the peak stresses will be the same as seen in Figure 2-29 and Figure 2-30. Applying H_e shows that the resulting hoop and meridional stresses depend on both the thickness of the shell edge and vary directly proportional to $\sqrt{r_2}$. The secondary radius of curvature r_2 is different for the inner and outer edges of the vessel. As a result, the peak stresses induced are different, as seen in Figure 2-31 and Figure 2-32. The more significant stresses are found at the outer edge (Zingoni, Enoma & Govender, 2015).

Reference must be made to Figure 2-28 for the applied actions M_e and H_e on the edges of the vessel.

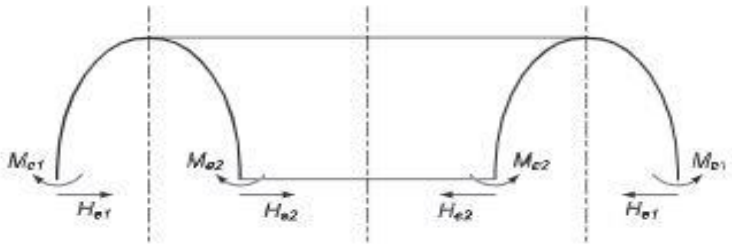

Figure 2-28:Actions on the semi-elliptical torus shell edge

The stress resultant results of an elliptic toroidal vessel as a result of applying M_{e1} are shown in Figure 2-29, M_{e2} in Figure 2-30, H_{e1} in Figure 2-31, and lastly, H_{e2} Figure 2-31 where (a) closed-form analytical solution results and (b) FEM results.

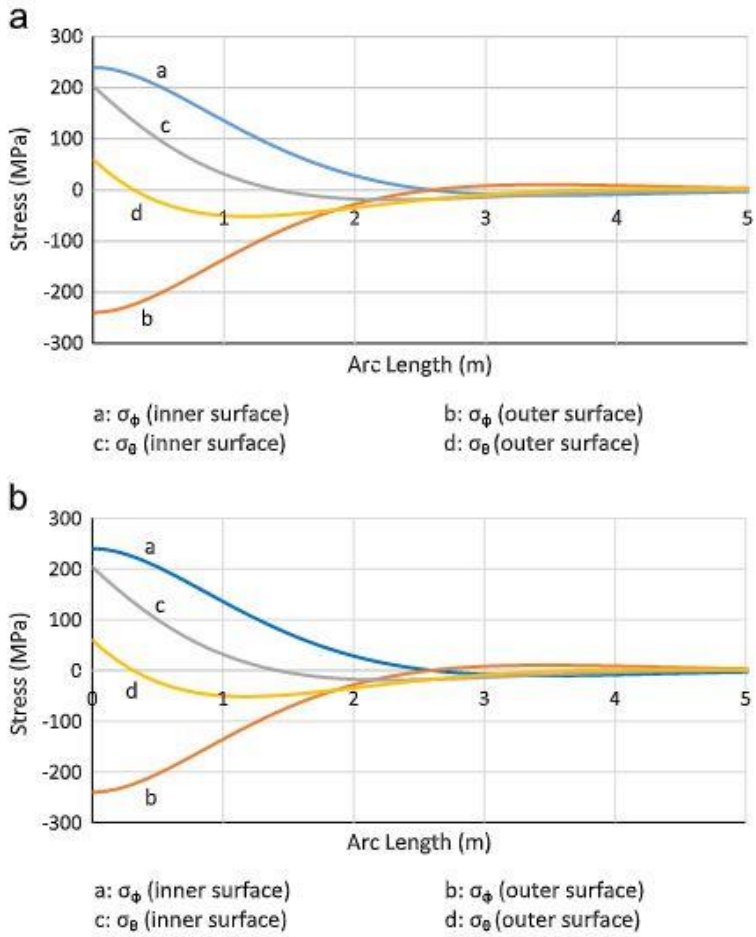

Figure 2-29: Variation of meridional and hoop stresses with arc length, due to M_{e1} (Zingoni, Enoma & Govender, 2015)

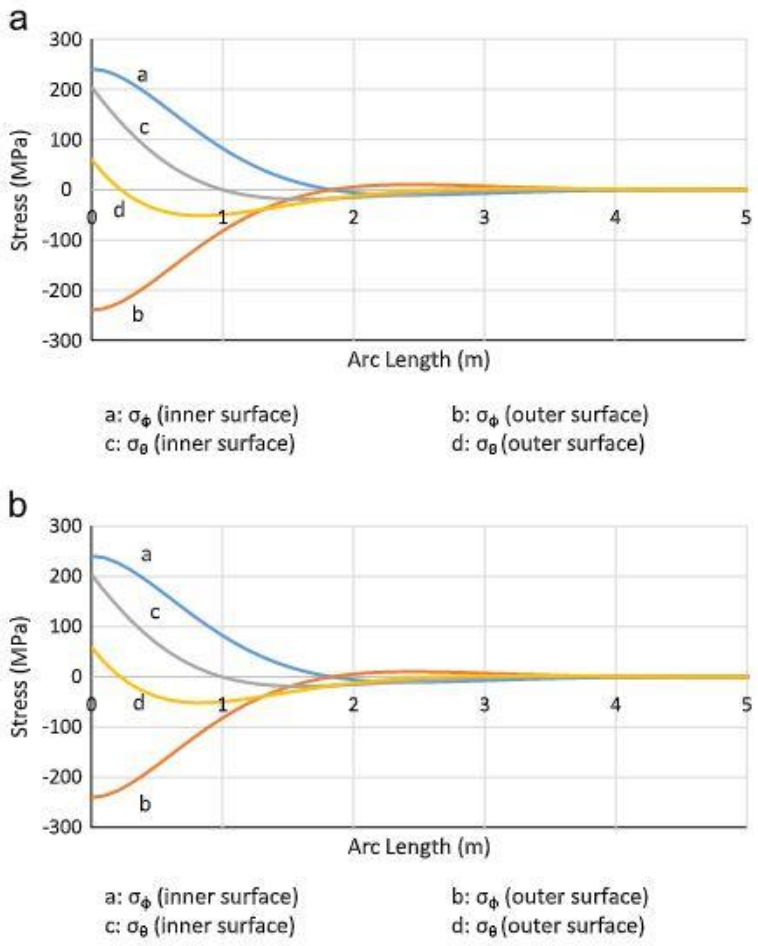

Figure 2-30:Variation of meridional and hoop stresses with arc length due to M_{e2} (Zingoni, Enoma & Govender, 2015)

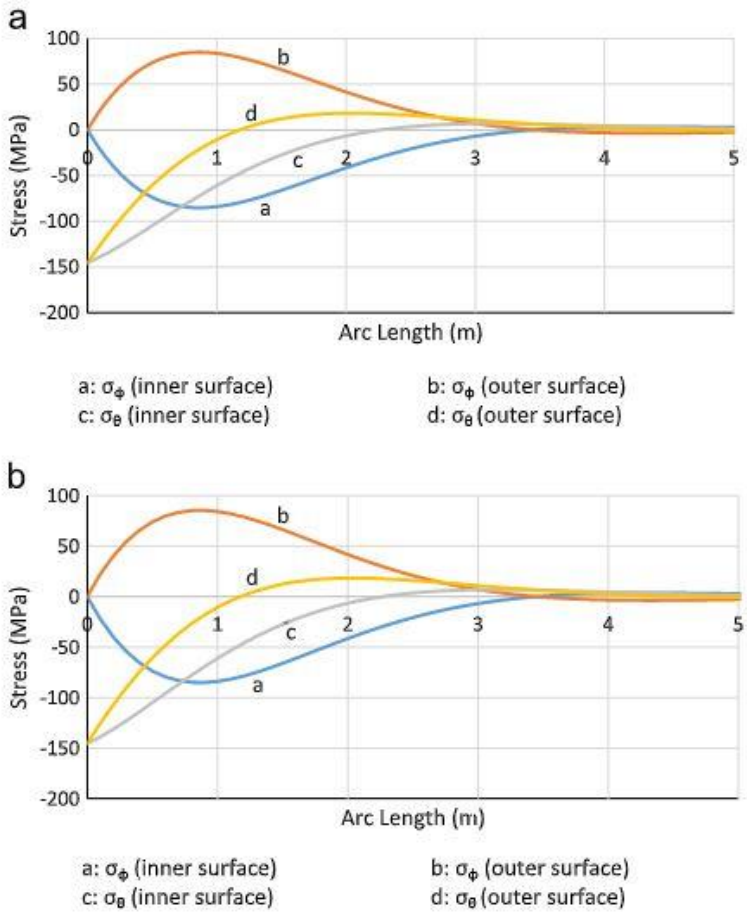

Figure 2-31:Variation of meridional and hoop stresses with arc length due to H_{e1} (Zingoni, Enoma & Govender, 2015)

There is a good agreement between the analytical results and FEM results. As a result, designers can use analytical solutions for design practices without having to do a complete numerical analysis of FEM to calculate the stresses. Furthermore, the theoretical formulations that have been developed can provide accurate results of stresses and deformations in the vicinity of any mid-side discontinuities of the shell (Zingoni, Enoma & Govender, 2015).

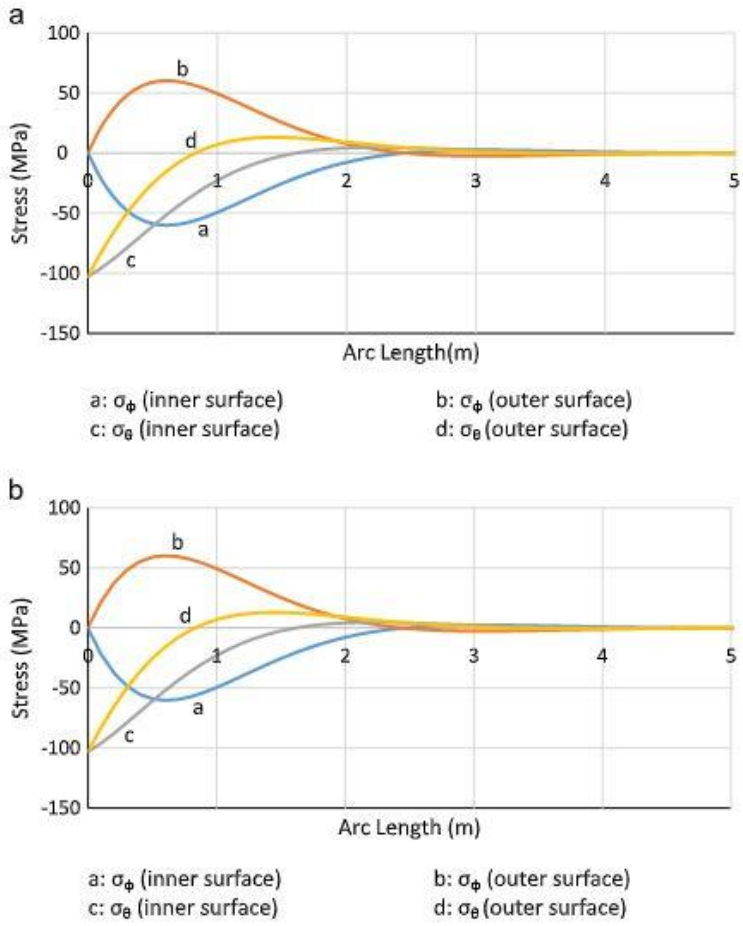

Figure 2-32:Variation of meridional and hoop stresses with phi, due to H_{e2} (Zingoni, Enoma & Govender, 2015)

2.3.2.4 Buckling and stability studies

Galletly (1998) investigated the elastic buckling of complete steel toroidal shells of elliptical cross-sections subjected to uniform internal pressure. The results were validated using two numerical analysis software, BOSR and INCA. The results obtained were in good agreement with each other.

2.3.2.5 FEM modelling and experimental studies

Song & Sun (2022) studied the nonlinear Goldenveizer's problem of a circular and elliptic elastic torus. In this study, they used FEM software ABAQUS and found that the radius ratios *a/R* and *a/b* greatly influence the deformation of both the circular and elliptical torus. They also found that the surface of the toroidal vessel with negative Gaussian curvature bears the load better than the positive Gaussian side. Increasing the ratio of *a/b* enhances the collapse load of an elliptic toroidal vessel (Song & Sun, 2022).

2.3.3 Hyperboloidal profile

This negative Gaussian surface has been widely used worldwide as a cooling tower in the energy industry. However, this profile has not been explored as an elevated liquid containment vessel. Nothing in existing literature has been reported for this new application, which the current study aims to explore. Existing literature on the use of hyperboloid cooling towers is reviewed to understand how this structure behaves under self-weight loading to form the basis of the current structural feasibility study for the application of a liquid containment vessel. A notable example of their application as cooling towers is the Niederaussem Cooling Tower in Germany, with a massive 200m height. The construction of this structure was completed in the year 2000. Figure 2-33 shows the reinforced concrete hyperbolic cooling tower.

Figure 2-33:Reinforced Concrete Hyperboloidal Cooling Tower Shell Structure(https://www.zenithstructural.com/structural-access-repair-specialists/cooling-towers/,n.d)

2.3.3.1 Shell geometry and shape optimisation

The geometry and generation of this shell of revolution can be found in studies (Zingoni, 1999; Mathieu, Shambina & Jaafar, 2021). A survey by Ansary, Damatty & Nassef (2011) on the optimum shape and design of cooling towers aimed at achieving an optimum shape and design of hyperboloid of revolution to be used as a cooling tower. The study was based on a non-linear finite element model using a genetic algorithm, and this model was developed in-house. The objective function of this study was to minimise the weight of the cooling tower, which was done by modelling the geometrical profile using B-spline curves. Mahfouz (2007) also used the genetic algorithm while studying the shape optimisation of a prismatic shell, as it leads to a reduction of strain energy and allows one to observe maximum displacement; it is

also suggested in this study for use in novel structural forms for future research in shape optimization.

The optimisation technique used by Ansary, Damatty & Nassef (2011) for the shape optimisation study is the global technique to arrive at a worldwide optimum approach other than a direct search local technique; the design variables and the constraints are also defined in the study. Furthermore, the study analysed the structure's response while keeping the thickness of the shell constant and including the thickness as one of the design variables. The findings on this optimisation of the 30MPa reinforced concrete hyperbolic cooling tower reduced the hoop (26%) and meridional moments (25%) in the first analysis of keeping the shell thickness constant (Ansary, Damatty & Nassef, 2011). Furthermore, a decrease in the self-weight of the tower was obtained as the shell thickness was reduced from 190mm to 165mm while applying the proposed optimisation technique, which included the shell thickness as the design variable. Figure 2-34 shows the geometric parameters of a hyperbolic cooling tower profile.

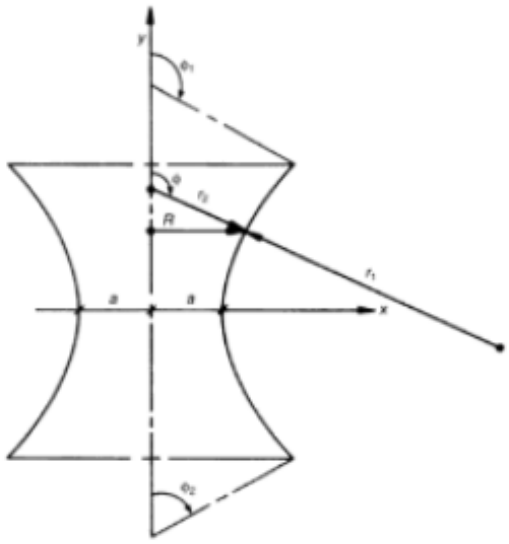

Figure 2-34:Geometric parameters of a hyperbolic shell [Zingoni, 1999]

2.3.3.2 Stress analysis

Self-weight and wind loading are primary concerns for analysing and designing the hyperboloidal shell. The loading components resulting from self-weight at any given point are expressed as a function of the shell's material unit weight and thickness. In addition, the shell has mid-surface curvature, which results in a tangential loading component to the surface and a radial component due to the self-weight of the structure (Zingoni, 1999).

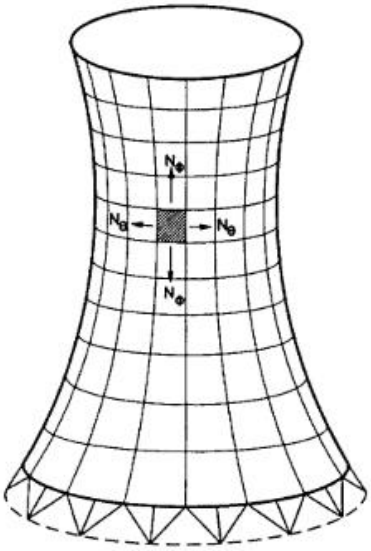

Figure 2-35:Membrane stress resultants on the hyperbolic shell

For the axisymmetric shell of revolution, such as the hyperboloid of revolution satisfying the smoothness in geometrical parameters, the derivatives and loading, the meridional and the hoop stress resultants may be adequate to perform the stress analysis if and only if requirements for a momentless stress state are all satisfied. Figure 2-35 shows the membrane stress resultants on a reinforced concrete hyperbolic cooling tower.

The shell thickness is firstly defined in terms of the meridional angle phi ($\emptyset$), the angle measured from the axis of revolution to a particular point of interest where the analysis of the stresses is performed. The loading components p_r and $p_{\varnothing}$ are then fully defined once the shell thickness is defined in terms $\emptyset$. In the study by Zingoni (1999), the hoop stresses in the hyperboloid shell are in compression throughout the surface, except near the free surface at the top, and these stresses are less when compared to stresses at the base of the cooling tower. Therefore, the provision of a ring beam nominal reinforcement at zones of less undergoing tensile stresses is necessary to minimise the shell's likelihood of tension failure.

Recommendations for the bottom angle with associated ratios of *b/a* are also given in the study. The quadratic distribution of the shell thickness also reduces the rapidly increasing stresses to about 50% in the shell as $\varnothing$ increases (Zingoni, 1999). Figure 2-36 Shows the force components on the hyperboloid meridian.

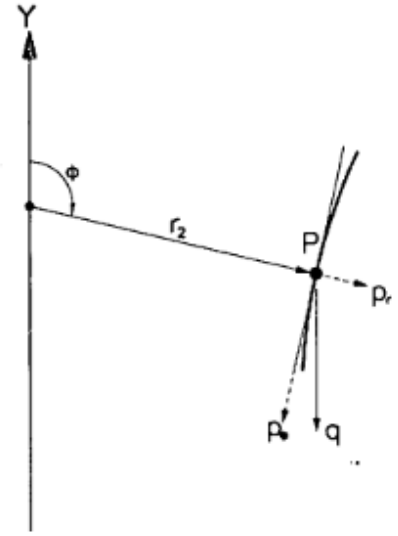

Figure 2-36:Force components on the shell surface (Zingoni, 1999)

2.3.3.3 Junction problems

The hyperboloid concrete cooling tower is generally supported on a group of flexible diagonal columns in a conical fashion at the base, tangential to the bottom of the shell. However, in the study by Rizkalla & Zia (1980), the assumption was made that there is a stiff ring girder bridging a gap between the column base plate surface; the first segment is supported radially when prestressing force is applied to reduce the tensile stresses in that region.

2.3.3.4 Buckling and stability analysis

According to Zingoni (1999), the choice of thickness of this shell of revolution is based on the body's buckling behaviour over material-strength considerations. This buckling phenomenon occurs when a stress combination of both meridional and hoop directions becomes critical. According to Bektas (2017), hyperboloidal shell structures are very resistant to buckling because they are doubly curved surfaces with negative Gaussian curvature. Figure 2-37 shows some examples of the buckling shape modes of a hyperboloid shell.

a) b)

Figure 2-37:Buckling mode shapes [(reproduced from(Ponath & George, 2016)]

2.3.3.5 FEM modelling and experimental studies

The optimum shape design of the hyperboloid cooling tower was done using a combination of finite element modelling, B-spline curves, and an accurately coded genetic algorithm. The FEM formulation included the geometric non-linear geometrical effects. The merit of the FEM model is due to its freedom from the shear-locking phenomenon observed while using the isoparametric shell elements used in most commercial software in the industry. The finite element used was composed of 13 nodes with the displacement degrees of freedom *u*, *v* and *w* along with the three global *x*, *y* and *z* coordinates, and the rotational degrees of freedom α, β, φ, and ψ were also defined using the local axis. The rotational parameters φ and ψ were varied on the quadrilateral, while α and β were kept constant through the depth of the element, as seen in Figure 2-38. A 3-D FEM, full-scale tower, was developed using 480 elements of finite-element mesh with two significant assumptions of simple support and linear elasticity since the structure is controlled by no cracking conditions (Ansary, Damatty & Nassef, 2011).

Yu et al. (2016) studied the collapse resistance performance of super-large hyperbolic cooling towers subjected to seismic actions using 4-node shell elements with bending and membrane capabilities. Figure 2-38 shows a 16-node shell element used on the shape optimisation of a hyperbolic shell structure by (Ansary, Damatty & Nassef, 2011).

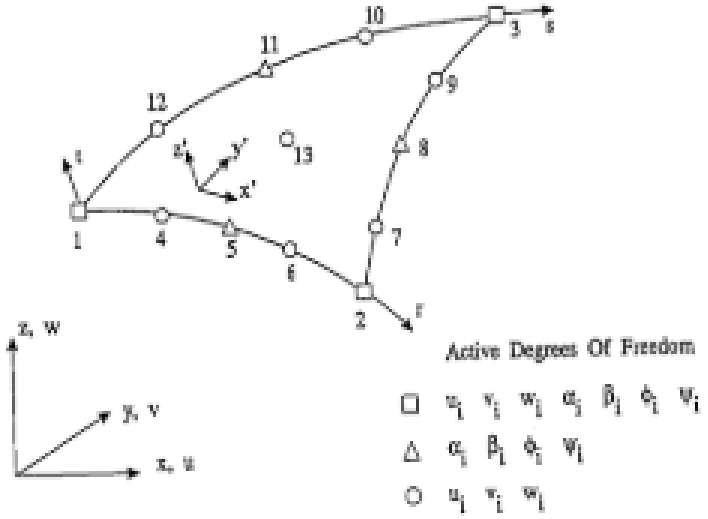

Figure 2-38:16-node shell element

The fully integrated general-purpose quadrilateral element S4 was used for accuracy in the current study. We see both authors using 4-node general shell elements with up to 6 degrees of freedom for their studies, an agreement between them for reinforced concrete shell elements.

Repeated eigenvalues in the linear eigenvalue buckling analysis will also be expected for the hyperboloidal shell used for liquid containment. It is also a structural system with symmetry in loading and geometry (Zingoni, 2022).

2.4 Design and construction considerations

2.4.1 Prestressed liquid containment structures

According to Kennedy (1944), prestressing was implemented to place concrete in sufficient compression by tightening the bands around the vessel's wall before subjecting the vessel to hydrostatic pressure. As a result, vertical cracks that would form due to tension at joints on the concrete vessel wall are minimised. Hence leaks and unsightly strains are avoided (Kennedy, 1944). The leaks in prestressed concrete circular water tanks mainly occur because of inadequate floors and foundations (Trahern J.W, 1955). Concrete tension limitations for service load conditions control the design of prestressed liquid containment structures. The ultimate limit state should also be checked (British Standards Institution., 1987).

Analysis and design of prestressed concrete are governed by peak hoop stresses and vertical bending moments of the wall along surface generators (Kennedy, 1944; Priestley M.J.N, 1985). The bending moments can be minimised by floating the wall on rubber pads, thus allowing it to

move inward when prestressed. Watertightness at the joint is achieved by using a dumbbell waterstop (Closner, 1960). Careful attention must be drawn to the tangential shear between the foundation ring and the walls of a prestressed concrete cylindrical tank. As a result, the tank becomes stable against seismic loads (Kennedy, 1944).

Design recommendations according to (British Standards Institution., 1987)

- The jacking force should not exceed $0.75f_{pu}$ for circular prestressed concrete tanks.
- The flexural compressive stress should not exceed $0.33f_c'$ at the extreme fibre
- When the structure is full or empty, there should be no resultant tension in the circumferential direction, after allowance for all losses of prestress and on the assumption that the top and bottom edges of the wall are free of all restraint.
- The tensile stresses arising from vertical moments should not exceed 1.0MPa

A study by Rizkalla & Zia (1980) gives insights into the prestressed concrete construction of a hyperboloid shell cooling tower in a step-by-step approach from starting point of segmental ring assembly to the complete erection of the structure. Rizkalla & Zia (1980) also recommends that the analysis of the sub-structure should be performed locally for the self-weight effects of the structure and that for each stage of construction, analysis and design must be treated separately. Zia & Mostafa (1983) conducted experimental studies to validate the theoretical results while using the principle of superposition of segments. The theoretical results agreed with the experimental results. On the other hand, discrepancies were found in circumferential strains and radial displacements; additionally, there was no comment on junction stresses.

The amount of reinforcement required for the hyperboloidal shell is based on the net stresses in the structure between the compressive stresses and the tensile stresses (Ansary, Damatty & Nassef, 2011). The stresses in the structure can be minimised by the gradual thickening of the structure (Zingoni,2022). Figure 2-39 shows how prestressing on a hyperboloidal vessel is done in segments.

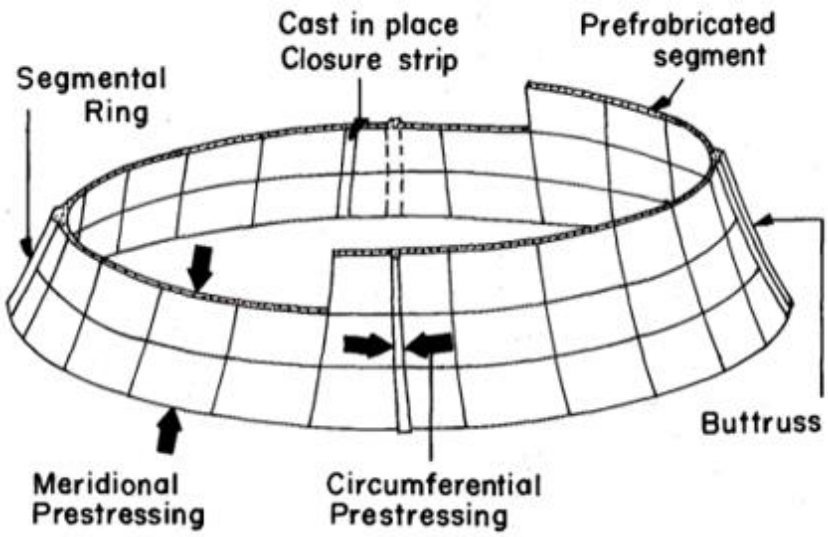

Figure 2-39:Prestressing on a hyperbolic cooling tower(Rizkalla & Zia, 1980)

The following recommendations for the construction of prestressed concrete cylindrical tank wall (Trahern J.W, 1955)

- Dense concrete, without honeycomb or shrinkage cracks, is fundamental. A well-designed concrete mix with a low water-to-cement ratio, careful placement, thorough vibration of the mix and thorough curing of the concrete is essential
- The walls should be constructed of separated panels continuously pouring from bottom to top. The panels should be short enough horizontally to prevent shrinkage cracks within them. The horizontal joints may result in differential shrinkage between the panels and locked-in stresses, which may make it impossible to achieve the anticipated distribution of prestress in the concrete
- Using high-strength steel for prestressing tank walls has some advantages of carrying the design loads even after the prestress losses have occurred in steel.
- Horizontal prestressing of the wall should be designed so that over-stressing of concrete will not occur so that some circumferential compression will be retained in concrete after stress losses with a full tank.
- Sufficient vertical prestressing in the wall should be provided to resist the vertical bending moments caused by horizontal prestressing. The vertical steel is centred in the wall to provide for bending in opposite directions

- The thickness of a tank wall at any elevation should be sufficient to support the initial tensioning of the prestressing steel without the development of stresses in concrete which might exceed safe working stresses

2.5 Concluding remarks

The review has covered the studies that have been covered in published journals, conference papers and a few textbooks on elevated liquid-storage reservoirs in the form of shells of revolution of double curvature. However, from this review, there is a gap showing that more research can be done on some geometries that have not been explored in liquid containment especially using concrete as a material because it can easily take any form. A hyperboloid of revolution has been used as a cooling tower before but has never been used in the application of elevated liquid-containment vessels. The review has shown some advantages of double curvature shells in strength and their capabilities of being built-in extended heights, which can be used as significant supersized vessels for liquid containment. Chapter 3 will focus on the methods used in this study t achieve the study's objectives.

3 Research Methodology

This section outlines the methods followed to achieve this research's expected outcome. The two methods followed in this study were the analytical method, which encompassed the derivation of closed-form equations that can be relied on to estimate the membrane stresses at the shell mid-surface. FEM (Numerical Method) is used to validate the results obtained from the Analytical method. The Finite Element Modelling method has been described as a powerful tool designers use to perform structural analysis and find solutions for problems involving complex geometries. These problems were reported to be practically impossible to solve in the 19^{th} century due to the nature of higher-order differential equations obtained using the shell theory. The Analytical method is first discussed, and the Finite Element Modelling will follow.

3.1 Analytical method

The analytical method conducted in the current study is based on the membrane theory of shells of revolution. The shell is assumed to have finite bending rigidity, and the membrane solution best approximates the actual state of stress in the shell. Although the actual state of stress can be obtained using the general bending theory of shells that also accounts for bending stresses, the equations developed from the bending theory are very complicated to solve, especially for the shells with complex geometry such as the one under investigation. Therefore, in this study, only the membrane theory will be considered.

3.1.1 Generating the shell surface

The shell of revolution was generated by rotating a plane hyperbola curve defined by equation 3-1 through 360^{o} about the axis of revolution in the plane of the curve. The axis of revolution was taken as the vertical axis, namely the y-axis in a three-dimensional space, as the shell under consideration will be used as an elevated liquid containment vessel. Furthermore, the stresses evaluated lie on the shell mid-surface, and therefore choosing the axis of revolution as vertical gave the shell the orientation that allowed the evaluation of the stresses in the main directions, the meridional direction, and the hoop direction.

The plane curve that was used to generate the hyperboloidal vessel had the form of the hyperbola defined using equation 3-1:

$$\frac{x^2}{a^2} - \frac{y^2}{b^2} = 1, \quad x \geq a \tag{3-1}$$

Where,

x is the vessel radius at any given point
y is the height of the vessel measured from the throat (y=0) positive upward direction
a is the throat radius
b is the constant of curvature

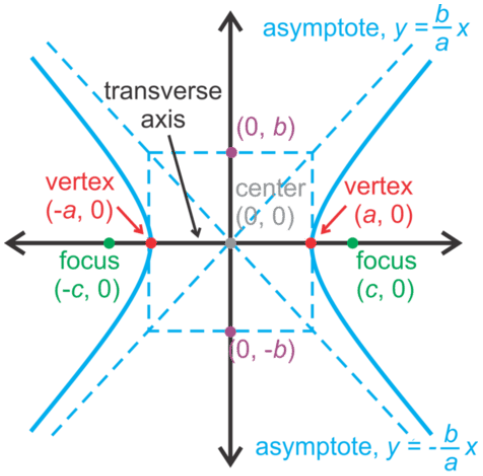

Figure 3-1: Hyperbola plane curve with the vertical axis of revolution (adapted from: https://sites.google.com/a/sas.edu.sg/math-club/home/algebra-2/chapter-9-quadratic-relations-and-conic-sections/9-5-graph-and-write-equations-of-hyperbolas

Figure 3-1 shows the hyperbola plane curve used to generate the vessel under investigation, which was formed with only the part above the line y=0 (x-axis, which was taken as the base of the vessel).

The height of the vessel *(H=70m)* and the throat radius *(a=21.65m)* were kept constant while generating the surfaces of the different shells under study. The geometric ratio *b/a* was varied from 2.1 to 2.8. These geometric ratios were used to calculate the constant of curvature *b* for different hyperboloidal vessels to be used in the parametric study to investigate the variation of the stress distribution along the shell's mid surface and buckling resistance of the vessel.

Table 3-1 shows the sample coordinates calculated using the equation 3-1 for different values of the z in a three-dimensional space from *z=0* at the vessel's base to *z=70* meters at the free surface of the vessel. The resulting profile of the vessel is shown in Figure 3-2.

Table 3-1: Coordinates for the surface generation (b/a=2.1)

Vessel Radius (m)	**Similar to X**	**Vessel Height (m)**	**Shell Curvature (m)**
X	Y	Z	b
21.65	0	0	45.465
21.67094	0	2	45.465
21.73363	0	4	45.465
21.83771	0	6	45.465
21.98261	0	8	45.465
22.1675	0	10	45.465
22.39142	0	12	45.465
22.65319	0	14	45.465
22.95152	0	16	45.465
23.28501	0	18	45.465
23.65218	0	20	45.465
24.05147	0	22	45.465
24.48131	0	24	45.465
24.94014	0	26	45.465
25.42637	0	28	45.465
25.93847	0	30	45.465
26.47493	0	32	45.465
27.03431	0	34	45.465
27.61521	0	36	45.465
28.21631	0	38	45.465
28.83634	0	40	45.465
29.4741	0	42	45.465
30.12847	0	44	45.465
30.79839	0	46	45.465
31.48288	0	48	45.465
32.18099	0	50	45.465
32.89186	0	52	45.465
33.61468	0	54	45.465
34.34871	0	56	45.465
35.09322	0	58	45.465
35.84758	0	60	45.465
36.61117	0	62	45.465
37.38343	0	64	45.465
38.16383	0	66	45.465
38.95188	0	68	45.465

39.74712	0	70	45.465

Typical throat radius (a)	21.65
b/a	2.1

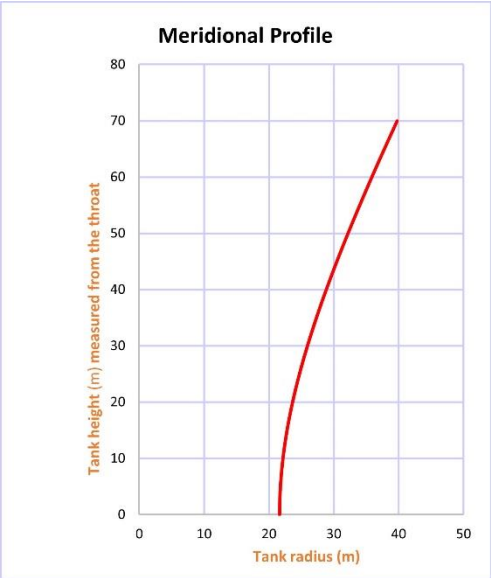

Figure 3-2:The shell's mid-surface profile

3.1.2 The meridional stresses

The stresses in the elevated liquid containment structures result from various loading conditions ranging from static loadings, such as self-weight and hydrostatic loading, and some dynamic loading, such as seismic loading, wind loading and some other kinds of loading. For this study, only hydrostatic loading will be considered as the investigation is focused on assessing the structural system's response when subjected to hydrostatic loading. Hydrostatic loading is axisymmetric since it results from the same pressure acting at all points on the surface at the same level in the horizontal circle on the surface. Therefore, any point on the surface can be defined in terms of the coordinates in space using one of the three coordinate systems, cartesian, cylindrical or spherical coordinates.

The general solution from the membrane theory of shells of revolution for the meridional stress is shown in equation 3-2. Reference must be made to section 2.1for the derivation of equation 3-2.

$$N_{\emptyset} = \frac{1}{r_2 sin^2\phi}\left[\int r_1 r_2 (p_r cos\phi - p_\phi sin\phi) sin\phi d\phi + k\right] \quad \textbf{(3-2)}$$

The general solution for the meridional stress of the shells of revolution was then adapted for the hyperboloidal vessel with only the hydrostatic loading taken into consideration. From equation 3-1, the relationship of the vertical coordinate *y* was developed in terms of the geometrical parameters *a, b* and *x.*

The derivations and results presented from equation 3-3 to 3-15 are extracted from Zingoni (2018:118)

$$y = \pm\frac{b}{a}\sqrt{x^2 - a^2} \quad \textbf{(3-3)}$$

Differentiating equation 3-3, with respect to x, equation 3-4 was obtained.

$$\frac{dy}{dx} = \pm\frac{b}{a}\frac{x}{\sqrt{x^2 - a^2}} = tan\phi \quad \textbf{(3-4)}$$

And from squaring 3-4,

$$tan^2\phi = \frac{b^2}{a^2}\left(\frac{x^2}{x^2 - a^2}\right) \quad \textbf{(3-5)}$$

Squaring of equation 3-4 to obtain equation 3-5 and rearranging enabled the development of equation 3-6.

$$x^2 = \frac{a^4 tan^2\phi}{a^2 tan^2\phi - b^2} \quad \textbf{(3-6)}$$

Then from equation 3-6, the *x*-coordinate that defines a coordinate on the meridian in the positive horizontal direction was obtained to be equation 3-7.

$$x = \frac{a^2 tan\phi}{(a^2 tan^2\phi - b^2)^{1/2}} = \frac{a^2 sin\phi}{(a^2 sin^2\phi - b^2 cos^2\phi)^{1/2}} \quad \textbf{(3-7)}$$

For the solution of equation 3-7 to be real, $a^2 sin^2\phi$ should be greater than $b^2 cos^2\phi$ and that was obtained when,

$$tan^2\phi > \frac{b^2}{a^2} \quad \textbf{(3-8)}$$

Then the second principal radius of curvature r_2 was given by,

$$r_2 = \frac{x}{sin\phi} = \frac{a^2}{(a^2 sin^2\phi - b^2 cos^2\phi)^{1/2}} \quad \textbf{(3-9)}$$

Substituting equation 3-7 into 3-3, equation 3-10 was obtained,

$$y = \pm \frac{b^2 cos\phi}{(a^2 sin^2\phi - b^2 cos^2\phi)^{1/2}} \quad \textbf{(3-10)}$$

Then by taking the second derivative of equation 3-10 with respect to x equation 3-11 was obtained as,

$$\frac{d^2y}{dx^2} = \frac{ab}{(x^2 - a^2)^{3/2}} \quad \textbf{(3-11)}$$

For any shell mid surface, the meridional radius of curvature (primary radius of curvature) is given by,

$$r_1 = \frac{\left[1 + \left(\frac{dy}{dx}\right)^2\right]^{3/2}}{\frac{d^2y}{dx^2}} \quad \textbf{(3-12)}$$

Substituting equation 3-4 and 3-11 into equation 3-12, equation 3-13 was obtained,

$$|r_1| = \frac{[a^2(x^2 - a^2) + b^2x^2]^{3/2}}{a^4 b} \quad \textbf{(3-13)}$$

Using equation 3-7 to eliminate x in equation 3-13, equation 3-14 was obtained,

$$|r_1| = \frac{a^2 b^2}{(a^2 sin^2\phi - b^2 cos^2\phi)^{3/2}} \quad \textbf{(3-14)}$$

The primary radius of curvature r_1 lies on the opposite side of the hyperboloid of revolution, which is the axis of revolution and must be taken as negative,

$$r_1 = \frac{-a^2b^2}{(a^2sin^2\phi - b^2cos^2\phi)^{3/2}} \quad \textbf{(3-15)}$$

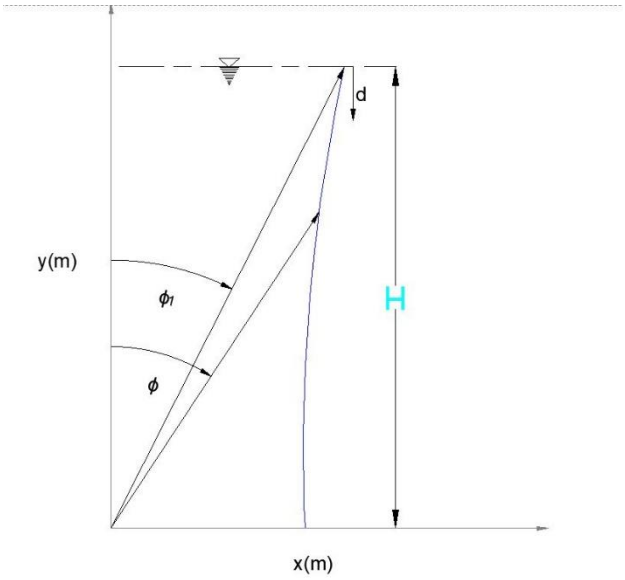

Figure 3-3:Positive direction meridian profile

Hydrostatic loading at any point on the shell surface acts in the direction normal to the surface and is proportional to the depth *d* of the liquid at that point. The depth of the liquid is defined using the downward vertical coordinate *d,* with the origin at the liquid's free surface at the vessel's capacity, as shown in Figure 3-3. The loading results in two loading components on the shell surface, the loading component in the meridional direction p_ϕ, and the loading component in the radial direction p_r. The loading component p_ϕ=0 since, for the study, only hydrostatic loading is considered, which is not the case when looking at the other loading types, such as the self-weight of the vessel. The radial direction force $p_r = \gamma d$, where γ is the unit weight of the liquid contained, and *d* is the depth of the liquid at the point of interest.

$$d = H - y \quad \textbf{(3-16)}$$

The equation for the radial force was given by,

$$p_r = \gamma(H - y) \quad \textbf{(2-17)}$$

Substituting equation 3-10 into 3-17 to eliminate *y,*

$$p_r = \gamma\left\{H - \frac{b^2 cos\phi}{(a^2 sin^2\phi - b^2 cos^2\phi)^{1/2}}\right\} \quad \textbf{(3-18)}$$

Substituting the expressions for r_1 (equation 3-15) and r_2 (equation 3-9)and those obtained for p_r (equation 3-18) and lastly, $p_\varnothing$ =0 into equation 3-2,

$$N_\phi = \frac{(a^2 sin^2\phi - b^2 cos^2\phi)^{1/2}}{a^2 sin^2\phi}\left[\int \frac{-a^2 b^2}{(a^2 sin^2\phi - b^2 cos^2\phi)^{3/2}} \times \frac{a^2}{(a^2 sin^2\phi - b^2 cos^2\phi)^{1/2}} \times \left(\gamma\left\{H - \frac{b^2 cos\phi}{(a^2 sin^2\phi - b^2 cos^2\phi)^{1/2}}\right\} \times cos\phi - 0\right) sin\phi d\phi + k\right] \quad \textbf{(3-19)}$$

Simplifying equation 3-19,

$$N_\phi = \frac{\gamma(a^2 sin^2\phi - b^2 cos^2\phi)^{1/2}}{a^2 sin^2\phi}\left[\int \left\{\frac{a^4 b^4 cos^2\phi sin\phi}{(a^2 sin^2\phi - b^2 cos^2\phi)^{5/2}} - \frac{H a^4 b^2 cos\phi sin\phi}{(a^2 sin^2\phi - b^2 cos^2\phi)^2}\right\} d\phi + k\right] \quad \textbf{(3-20)}$$

The integral in equation 3-20 translated into,

$$\int \left\{\frac{a^4 b^4 cos^2\phi sin\phi}{(a^2 sin^2\phi - b^2 cos^2\phi)^{5/2}} - \frac{H a^4 b^2 cos\phi sin\phi}{(a^2 sin^2\phi - b^2 cos^2\phi)^2}\right\} d\phi \quad \textbf{(3-21)}$$

$$= \frac{H a^4 b^2}{2(a^4 tan^2\phi - a^2 b^2)} - \frac{a^4 b^4 cos^3\phi}{3a^2(a^2 - (a^2 + b^2)cos^2\phi)^{3/2}}$$

Therefore,

$$N_\phi = \frac{\gamma(a^2 sin^2\phi - b^2 cos^2\phi)^{1/2}}{a^2 sin^2\phi}\left[\frac{H a^4 b^2}{2(a^4 tan^2\phi - a^2 b^2)} - \frac{a^4 b^4 cos^3\phi}{3a^2(a^2 - (a^2 + b^2)cos^2\phi)^{3/2}} + k\right] \quad \textbf{(3-22)}$$

At the top edge, $\phi = \phi_1$ as shown in figure 3-3, N_ϕ must vanish since the edge is free. This enabled the evaluation of *k*,

$$k = -\left(\frac{Ha^4b^2}{2(a^4tan^2\phi_1 - a^2b^2)} - \frac{a^4b^4cos^3\phi_1}{3a^2(a^2-(a^2+b^2)cos^2\phi_1)^{3/2}}\right) \quad \textbf{(3-23)}$$

Substituting equation 3-23 back into 3-22, the final solution for the meridional stress resultant,

$$N_\phi = \frac{\gamma(a^2sin^2\phi - b^2cos^2\phi)^{1/2}}{a^2sin^2\phi}\left[\left(\frac{Ha^4b^2}{2(a^4tan^2\phi - a^2b^2)} - \frac{a^4b^4cos^3\phi}{3a^2(a^2-(a^2+b^2)cos^2\phi)^{3/2}}\right) - \left(\frac{Ha^4b^2}{2(a^4tan^2\phi_1 - a^2b^2)} - \frac{a^4b^4cos^3\phi_1}{3a^2(a^2-(a^2+b^2)cos^2\phi_1)^{3/2}}\right)\right] \quad \textbf{(3-24)}$$

3.1.3 The hoop stress resultant

The hoop stress resultant is found at a point on the shell's mid-surface in the direction of the latitude circles. The general solution for the hoop stress resultant is given by equation 3-25. Reference must be made to chapter 1 for the derivation of equation 3-25.

$$N_\theta = r_2p_r - \frac{r_2}{|r_1|}N_\phi \quad \textbf{(3-25)}$$

Substituting expressions for $|r_1|$ (equation 3-14) and r_2 (equation 3-9)and those obtained for p_r (equation 3-18) into equation 3-25,

$$N_\theta = \frac{a^2}{(a^2sin^2\phi - b^2cos^2\phi)^{1/2}}\left[\gamma\left\{H - \frac{b^2cos\phi}{(a^2sin^2\emptyset - b^2cos^2\phi)^{1/2}}\right\} + \frac{(a^2sin^2\phi - b^2cos^2\phi)^{3/2}}{a^2b^2} \times N_\phi\right] \quad \textbf{(3-26)}$$

Where N_ϕ is the result obtained in equation 3-24

3.2 The Finite Element Analysis Method

The finite-element method was conducted to validate the analytical solutions used to calculate the membrane meridional and the membrane hoop stress resultants. It was further used for the Linear Eigenvalue Buckling Analysis to obtain the critical buckling pressures for the parametric study. For this method, the numerical analysis software ABAQUS was used.

3.2.1 Stress Analysis validation

Firstly, before turning into the current research problem, validation was carried out using equation 8.121a in (Zingoni, 2018:305) to get the total meridional stresses in the shell. After completing the analytical solutions, the problem was solved again using FEM software ABAQUS to obtain total meridional stresses in the shell for comparison. Secondly, for the current research problem, the stress analysis results were validated using the FEM software ABAQUS to check the correctness of the membrane meridional stress resultant equations and the membrane hoop stress resultant equation.

3.2.1.1 Validation based on literature

The geometrical and material properties of a spherical dome used to validate the solutions are shown in Table 3-2. The dome was modelled as an axisymmetric shell element because the geometry, loading, and deformation were considered axisymmetric. For this purpose, the quadratic axisymmetric shell elements SAX2 with three nodes was used. The number of shell elements along the surface was 100 in total. The boundary conditions were taken as encastre for FEM as well as the analytical method.

Table 3-2:geometrical and material properties of a spherical dome

Description	Value
Plan diameter of the dome	D=60m
Rise of the Dome	η=8.04
Rise-to-diameter ratio	η/D=0.134
The radius of the spherical shell	a=60m
Constant shell thickness	t=0.5m
Radius-to-thickness ratio	a/t=120
Support angle	$\emptyset s = 30^o$
Uniform distributed load	q=1kN/m^2
Young's Modulus of Elasticity	E=28GPa
Poison's ratio	v=0.15

3.2.1.2 Validation of the current problem

Validation of the closed-form analytical solution for the current study was carried out for the geometric ratio of b/a=2.1. Validation was done to check the correctness of the derived analytical solution equations for membrane meridional and hoop stress resultants using the numerical analysis software ABAQUS. The hyperboloidal vessel was modelled as an axisymmetric shell element for the stress analysis since the geometry and loading on the structure are axisymmetric, and the deformation is axisymmetric. Figure 3-4 shows the result of inserting the coordinates in ABAQUS to generate the meridian by creating a part. This FEM

was carried out on a series of steps called modules in ABAQUS software, as shown in Figure 3-5.

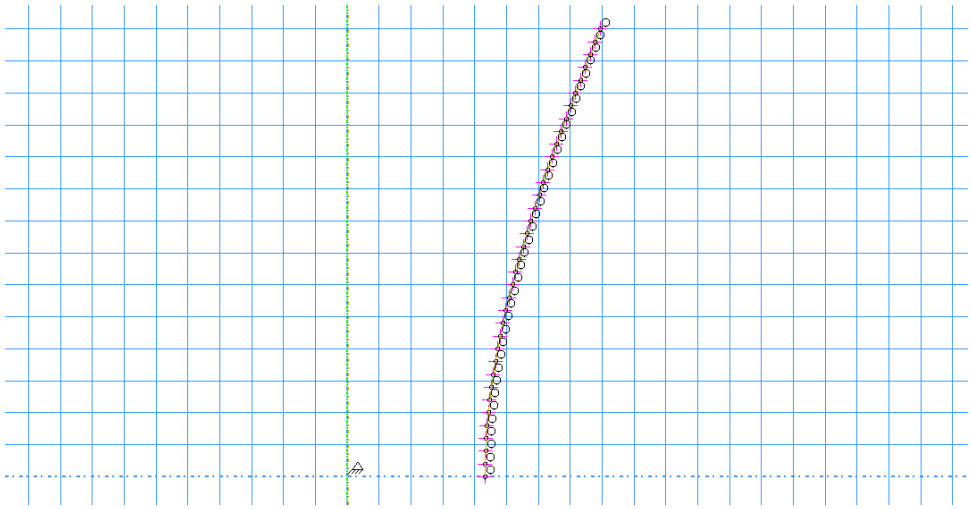

Figure 3-4:Part creation using coordinates

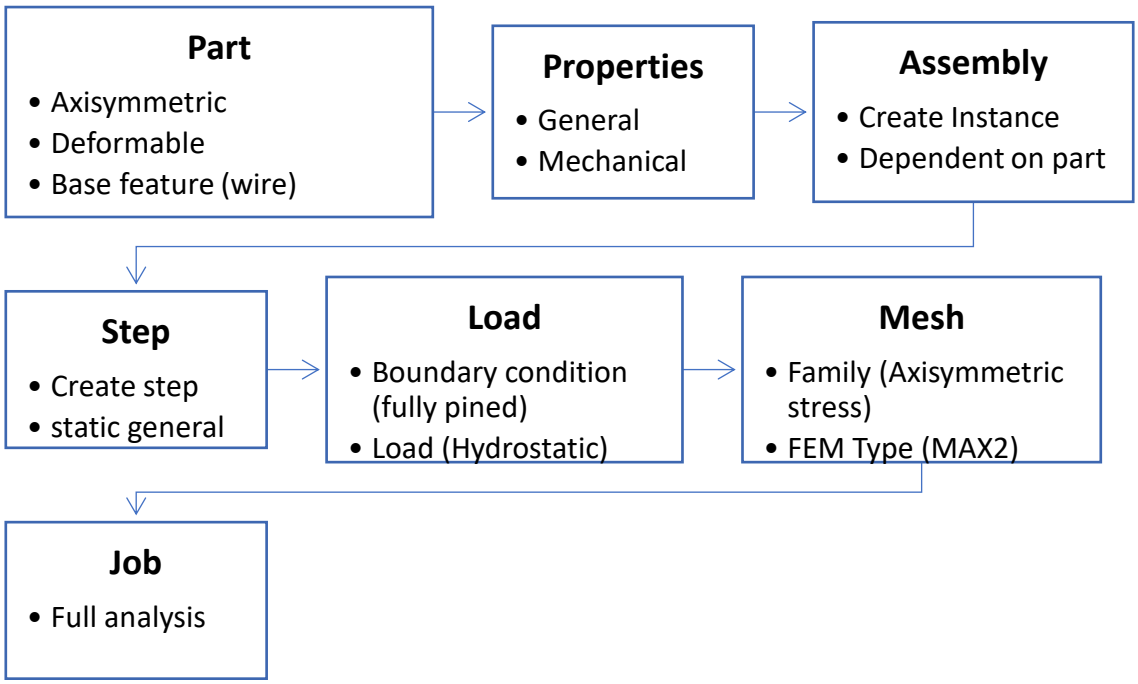

Figure 3-5: Modelling steps in ABAQUS

The material properties under the properties module were selected as general with (mass density=2400kg/m^3) and elastic mechanical properties (*E=28GPa, v=0.15)*, where *E* is Young's modulus of elasticity and *v* is the Poisson's ratio. Under the properties module, the

section thickness was kept constant at 100mm. The boundary condition was taken as fully pinned in the load module, as seen in Figure 3-6. The shell was analysed for only membrane forces so that no bending effects were to be induced in the shell through the support condition.

The unit weight of water was taken as 10 000N/m^{3,} which gave the maximum reference pressure at the support to be γH=700 000N/m^2. Where $H=70m$ is the height of the vessel, as seen in Figure 3-3. Lastly, under the mesh module, the FEM type was taken as MAX2, a three-node quadratic axisymmetric membrane with 208 elements in total, each element had a length of 0.347m and the element control formulation type was set to membrane as seen Figure 3-8.

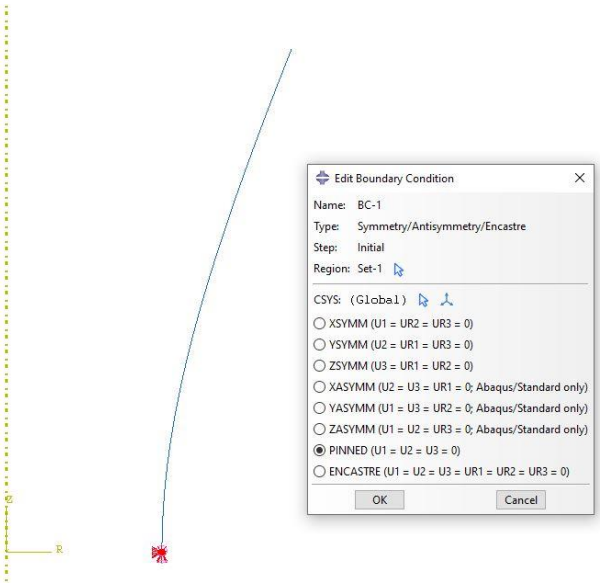

Figure 3-6:Support condition

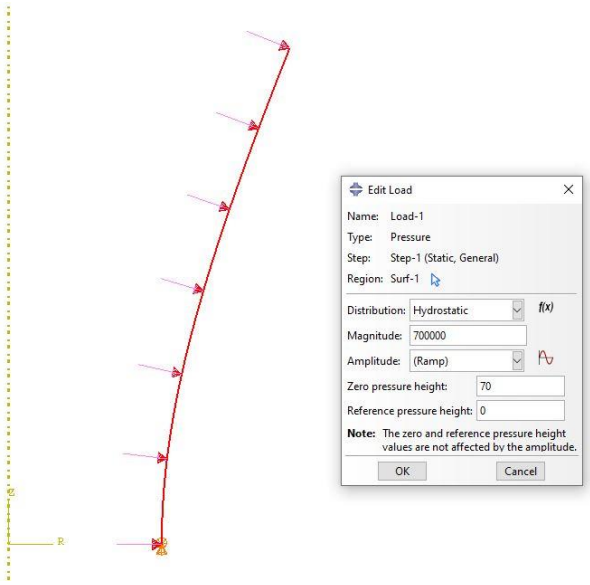

Figure 3-7:Hydrostatic load on the shell surface

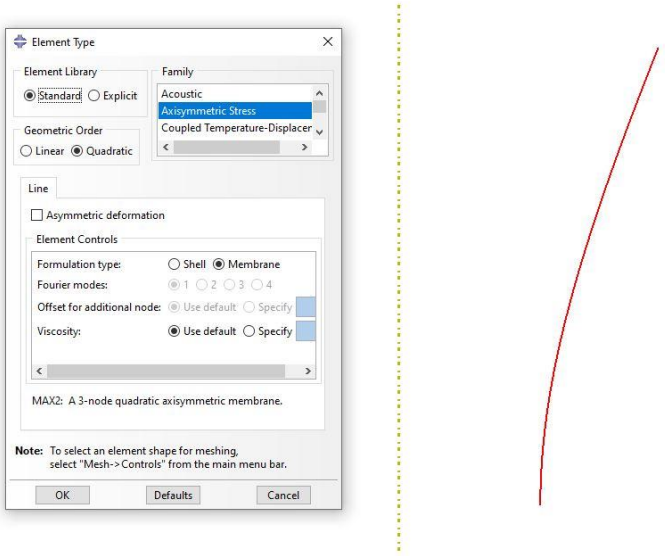

Figure 3-8:Meshing module

3.2.2 Linear Eigenvalue Buckling

3.2.2.1 Validation

Validation was done before turning into the current research problem based on the literature of the linear eigenvalue buckling analysis of spherical cap while subjected to a uniformly distributed pressure $p = 1MPa$ with fully pinned support conditions. Equation 11.65 (b) (Zingoni, 2018:385) was used, and the critical buckling load was obtained from the basis of the

analytical analysis. The material and geometrical properties used for the analysis are shown in Table 3-3. The same problem was solved using the FEM software ABAQUS for the eigenvalue buckling analysis to obtain the eigenvalue, which then gives the buckling pressure and the buckling mode. The steps outlined in Figure 3-10 were followed for the analysis. The FEM type was taken as a linear four-node doubly curved general-purpose shell S4 (Figure 3-11) with a total of 6692 elements.

Table 3-3:Geometrical and material properties of the spherical cap

Material parameter	Magnitude
Elasticity Modulus (MPa)	210 000
Poisson's ratio	0.3
Geometric parameters	
Radius *a* (mm)	500.25
∅	14.469
Uniform wall thickness (mm)	0.5
H/r	0.127

3.2.2.2 Linear eigenvalue analysis of the current research problem

A linear eigenvalue buckling analysis was performed using the FEM software ABAQUS in a series of steps called modules, as seen in Figure 3-9. The first module is part, as seen in Figure 3-10, where the coordinates in Table 3-1 were copied into the software to generate the vessel's profile. The material properties of concrete were taken as *E=28GPa and v=0.15,* and the section thickness was kept constant at 0.1 metres. Some buckling modes are not symmetric; therefore, the choice of the FEM type was taken as a linear four-node doubly curved general-purpose shell S4 as seen in Figure 3-11 with a total of 14016 elements. In the load module, the boundary condition was taken as encastre (fixed), as seen in Figure 3-12, since the vessel will be leakage free. The hydrostatic reference pressure was assigned a magnitude of $1000N/m^2$ as seen in Figure 3-13. The last step was to submit the job for analysis and obtain the eigenvalues and shape modes.

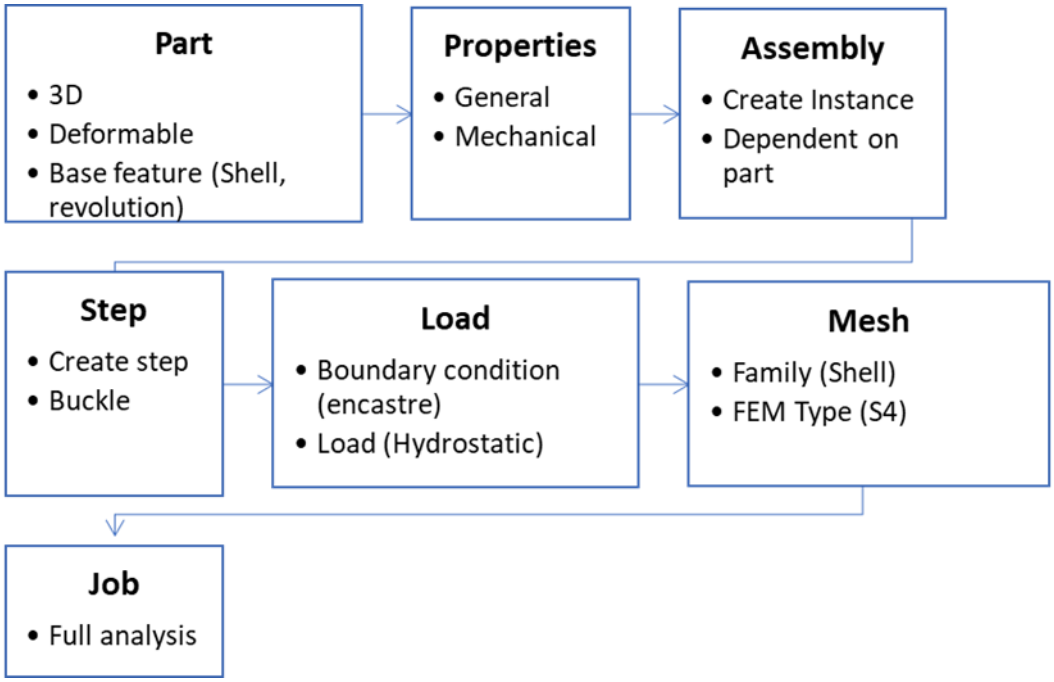

Figure 3-9:Linear Eigenvalue Buckling Modelling steps

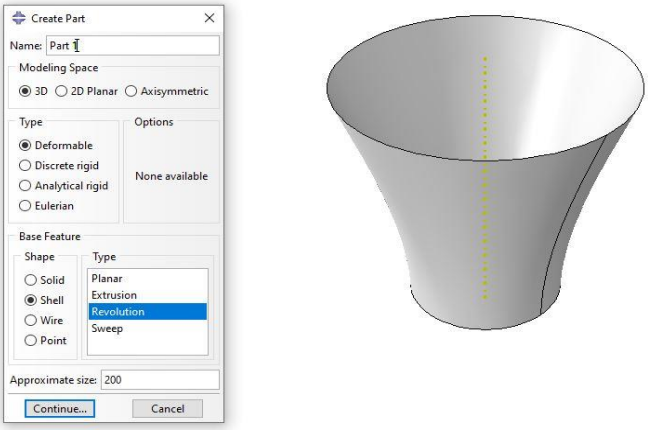

Figure 3-10:Part creation module

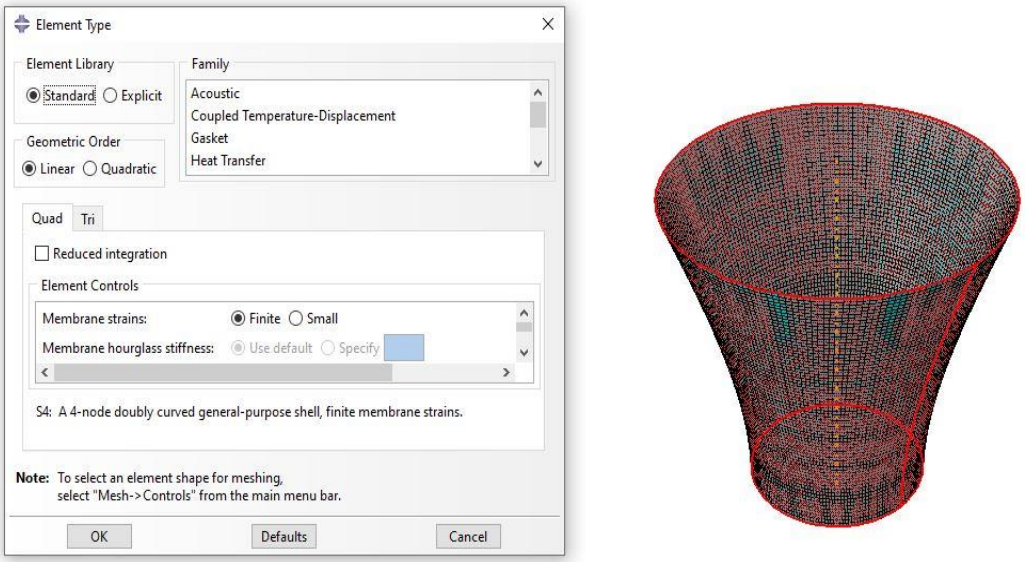

Figure 3-11:Meshing module

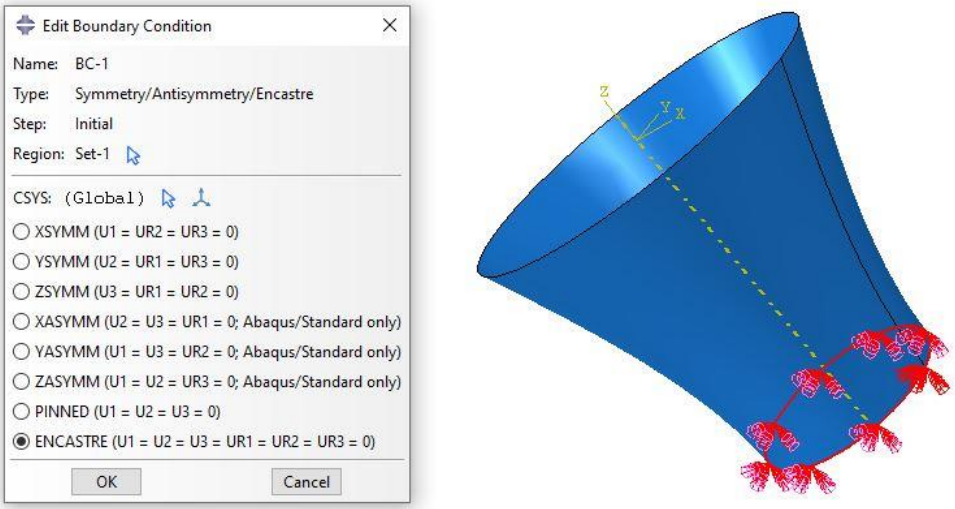

Figure 3-12:The support condition

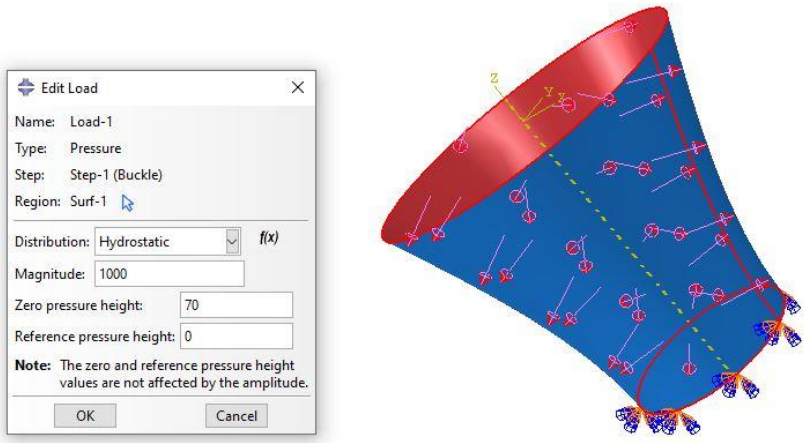

Figure 3-13:Applied internal hydrostatic load

4 Parametric study

Chapter 3 presented the methods followed to perform the stress analysis and the linear eigenvalue buckling analysis of the hyperboloidal vessel under hydrostatic loading. This chapter will present the results obtained from the described methods while varying the governing geometrical properties describing the vessel's mid-surface. The geometrical parameter ratio *b/a* of 2.1, 2.2, 2.3, 2.4, 2.5, 2.6, 2.7 and 2.8 was closely monitored for its effect on the meridional and hoop stress resultants and buckling pressures. In addition, the effect of the geometrical ratio on the vessel's capacity while keeping the throat radius *a* and tank height (*H)* constant will also be discussed.

4.1 Stress analysis

4.1.1 Validation

The method in section 3.2.1.1 was followed before attempting the current research problem, and the results of the meridional stress analysis of the spherical cap under uniform pressure loading *p* are shown in Figure 4-1.

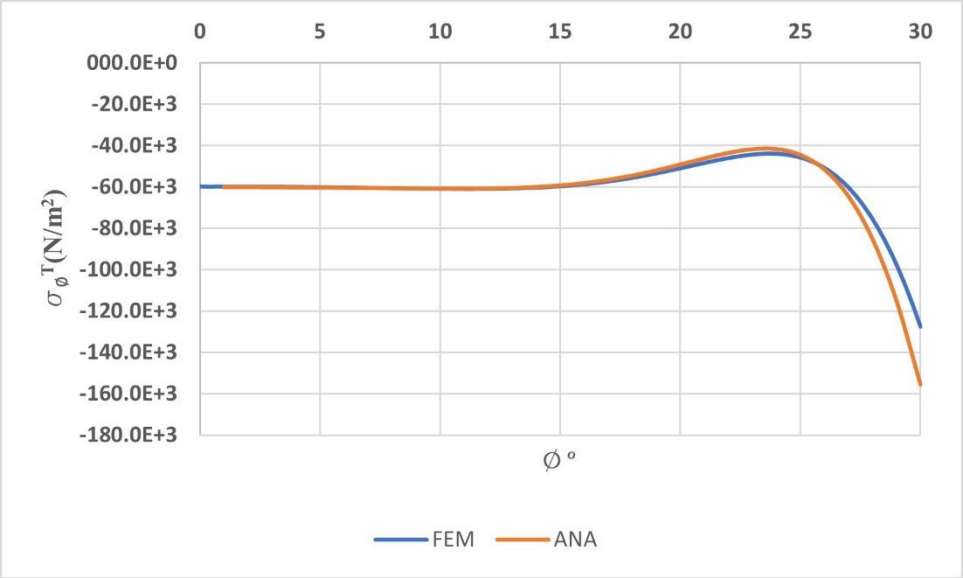

Figure 4-1:Inner meridional stress variation with ∅

A comparison of the stress analysis results from analytical closed-form results and FEM analysis results is shown in Table 4-1. From the comparison, the results are very close, and the difference between the two methods is less than 1% from the numerical results computed at six different locations on the shell surface. Therefore, it can be concluded that the results agree with each other and form the basis for modelling the current research problem.

Table 4-1:FEM vs Analytical results for inner meridional stresses

ϕ (°)	Analytical (x 10^3 N/m^2)	FEM(x 10^3 N/m^2)	(%)Diff
0	-60	-59.7	0.50
2	-59.9	-59.7	0.33
4	-59.9	-59.8	0.17
6	-60	-60	0.00
8	-60.2	-60.1	0.17
10	-60.5	-60.5	0.00

4.1.2 Numerical results

Further validation of the two methods, FEM and the analytical method was carried out for the current research problem to check the agreement of numerical results from the two methods before the parametric study for the current problem was carried out. The method (FEM) described in section 3.2.1.2 was followed to obtain the membrane meridional and hoop stresses from the numerical modelling, and the analytical method equations 3-24 (membrane meridional stress equation) and 3-26 (membrane hoop stress equation) were used to obtain the numerical results. The procedure for obtaining the meridional stress resultants and the hoop stress resultants using closed-from equations with the vessel with the geometrical ratio of *b/a*=2.1 is outlined in this section.

H=70m, a=21.65m, b=45.465m, γ*=10 000*N/m^3

Firstly, the computation of the meridional stress will be carried out, and then the hoop stress resultant will follow since it is dependent on the meridional stress resultant, as seen in their relationship from equation 3-26. From equation 3-24. The constant angle parameter ϕ_1, which is the angle at the free surface of the water at the vessel's capacity, must also be calculated before evaluating the stress at any point on the vessel's surface. Equation 3-24 can be used in conjunction with Figure 3-1 as the reference for the geometrical parameters of the hyperboloidal vessel.

The angle ϕ_1 is obtained from equation 4-1, when *y=H,* and the depth of water *d =0m,* see Figure 3-3.

$$\phi = tan^{-1}\left[\frac{b}{a}\times\left(1+\left(\frac{b}{y}\right)^2\right)^{1/2}\right] \qquad \text{for y > 0} \qquad \textbf{(4-1)}$$

$$\phi = \phi_1 = tan^{-1}\left[2.1\times\left(1+\left(\frac{45.465}{70}\right)^2\right)^{1/2}\right]$$

The value of $\phi_1 = 68.231^o$, say calculation of the meridional stress when the depth of the liquid is 5m from the water level when the vessel is full, is to be calculated. Firstly, the angle ϕ at a depth of 5m, when y =65m from the base, is calculated. Substitute the *y*=65m, *b/a*=2.1, and (*b*=45.465m) in equation 4-1 result $\phi = 68.684^o$. Then substitute the parameters into equation 3-24 to obtain the membrane meridional stress resultant at 5m depth from the free surface.

$$N_\phi = \frac{10\,000 \times (21.65^2 sin^2(68.684) - 45.465^2 cos^2(68.684))^{1/2}}{21.65^2 sin^2(68.684)} \times \left[\left(\frac{70 \times 21.65^4 \times 45.465^2}{2(21.65^4 tan^2(68.684) - 21.65^2 \times 45.465^2)} - \frac{21.65^4 \times 45.465^4 cos^3(68.684)}{3 \times 21.65^2 (21.65^2 - (21.65^2 + 45.465^2) cos^2(68.684)^{3/2}}\right) - \left(\frac{70 \times 21.65^4 \times 45.465^2}{2(21.65^4 tan^2(68.231) - 21.65^2 \times 45.465^2)} - \frac{21.54^4 \times 45.465^4 cos^3(68.231)}{3 \times 21.65^2 (21.65^2 - (21.65^2 + 45.465^2) cos^2(68.231))^{3/2}}\right)\right]$$

$$N_\phi = -5.374 \times 10^4 N/m$$

The corresponding hoop stress was found using equation 3-26,

$$N_\theta = \frac{21.65^2}{(21.65^2 sin^2(68.684) - 45.465^2 cos^2(68.684))^{1/2}} \times \left[10\,000 \times \left\{70 - \frac{45.465^2 \cos(68.684)}{(21.65^2 sin^2(68.684) - 45.465^2 cos^2(68.684))^{1/2}}\right\} + \frac{(21.65^2 sin^2(68.684) - 45.465^2 cos^2(68.684))^{3/2}}{21.65^2 \times 45.465^2} \times (-5.374 \times 10^4)\right]$$

$$N_\theta = 2.0246 \times 10^6 N/m$$

Table 4-2 (membrane meridional stress resultants) and Table 4-3 (membrane hoop stress resultants) show the difference in the percentage error of the results from the two compared methods for validation. For the numerical results shown in the table, the discrepancy is generally less than 5 percent, confirming the validity of the derived closed-form analytical equations and showing that engineers can rely on them to approximate the actual stress resultants in the vessel.

Table 4-2:Analytical versus Finite Element Method (FEM) results for meridional stress resultants

Depth(m)	**y(m)**	**∅°**	**ANA(N/m)**	**FEM(N/m)**	**%Diff**
5	65	68.684	-53.74×10^{3}	-54.610×10^{3}	1.59
10	60	69.216	-0.2141×10^{6}	-0.2116×10^{6}	1.18
15	55	69.846	-0.480×10^{6}	-0.4600×10^{6}	4.34
20	50	70.591	-0.8463×10^{6}	-0.8562×10^{6}	1.76
25	45	71.480	-1.308×10^{6}	-1.316×10^{6}	0.61
30	40	72.539	-1.855×10^{6}	-1.862×10^{6}	0.38

Table 4-3:Analytical versus Finite Element Method for membrane hoop stress resultant

Depth(m)	**y(m)**	**∅°**	**ANA(N/m)**	**FEM(N/m)**	**%Diff**
5	65	68.684	2.024×10^{6}	2.049×10^{6}	1.23
10	60	69.216	3.818×10^{6}	3.687×10^{6}	3.55
15	55	69.846	5.391×10^{6}	5.299×10^{6}	1.74
20	50	70.591	6.7454×10^{6}	6.773×10^{6}	0.41
25	45	71.480	7.897×10^{6}	7.912×10^{6}	0.19
30	40	72.539	8.853×10^{6}	8.867×10^{6}	0.16

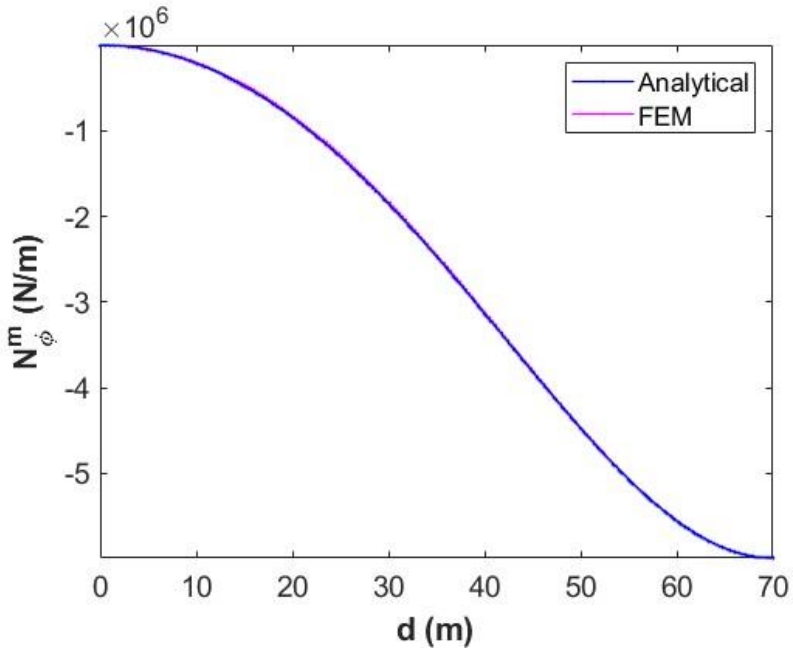

Figure 4-2:Variation of meridional stresses with the depth of the liquid (d)

Figure 4-2 shows the graphical comparison of membrane meridional stresses from the FEM analysis and the closed-form analytical results. In addition, the numerical results of the vessel with the geometrical ratio of b/a=2.1 were obtained at different depths d on the vessel's surface to check the difference in meridional stresses magnitudes from the two methods. From the graphical representation, it can be observed that there is a good agreement of results from both the FEM and the analytical methods.

Figure 4-3 shows a good agreement between the Finite-element method and the analytical method numerical results on a graphical presentation view of hoop stress resultant. This further validates the closed-form analytical derived equations in chapter 3 and can be relied on to approximate the actual hoop stress resultants in the vessel filled with a liquid.

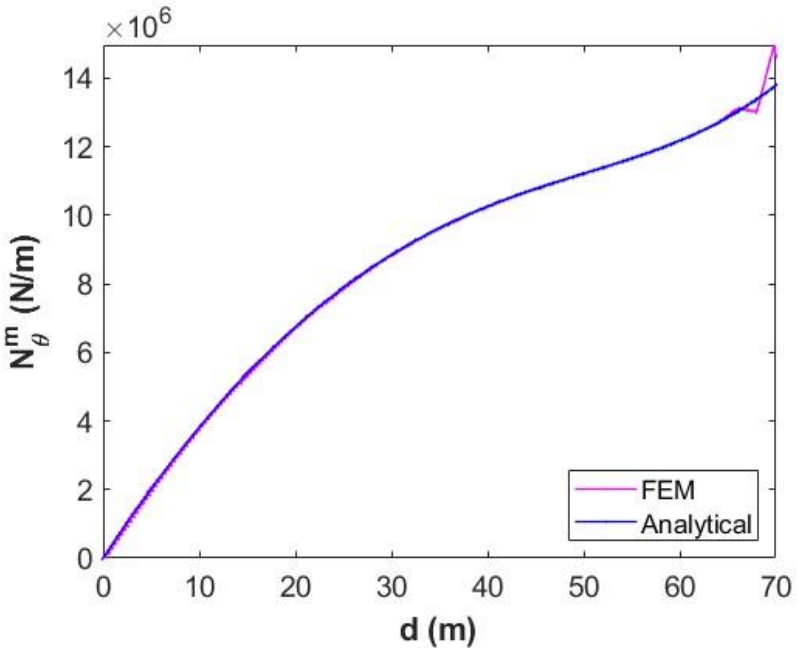

Figure 4-3:Variation of the hoop stress resultant with depth of the liquid d(m)

4.1.3 Effect of b/a variation on Meridional stress resultants

The geometric ratio of *b/a* was varied from 2.1 to 2.8 with an increment of 0.1, allowing analysis of eight hyperboloidal liquid containment vessels. The results shown in Figure 4-4 are parametric study results from the analytical method for obtaining membrane meridional stress resultants. Each line on the graph represents the meridional stress resultant variation with depth (m) for various *b/a* ratios on their respective vessels. For each vessel, the height of vessel *H*, and the throat radius *a*, were kept constant so that the different vessels were subjected to the same pressure at the base of the tank.

In Figure 4-4, it can be observed that, for all the vessels, the membrane meridional stress resultant is zero at the free surface as expected since the depth of the liquid at that point is zero for all different vessels and thus resulting in zero pressure exerted on the surface of the different vessels. However, as the depth of the liquid increases, it is also observed that all vessels experience a rapid increase in membrane meridional stress resultant, which is in total compression (negative forces) for all vessels.

It can also be observed that when the depth of the liquid is between 60 and 70 metres, the curves approach a zero slope. This shows that the stress resultant does not increase rapidly in that region as before, the region approaching the base of the vessel at a depth of 70 metres. At

the base of the vessel, the vessel experiences maximum stress resultant as expected, as that is where the vessel experiences the maximum hydrostatic pressure.

The throat radius *a* was kept constant for the geometric ratio *b/a*, while the curvature constant *b* was increased. The more cured the surface was, under the same loading conditions and boundary conditions, the better in resisting the membrane meridional stress resultant, as seen in Figure 4-4. This agrees with the existing literature that the shell structures inherit their strength from curvature.

The main observation of interest was to see what happens to the stress resultants when the geometric ratio of *b/a* is varied from 2.1 to 2.8. As the ratio of *b/a* was increased, the maximum stress resultant's slope moved from being steepest, which was when the ratio of *b/a* was the lowest, being 2.1, to the most gentle, as seen on the curve for the *b/a*=2.8. In addition, the membrane meridional stresses decreased as the ratio of *b/a* was increased, as seen in Figure 4-4.

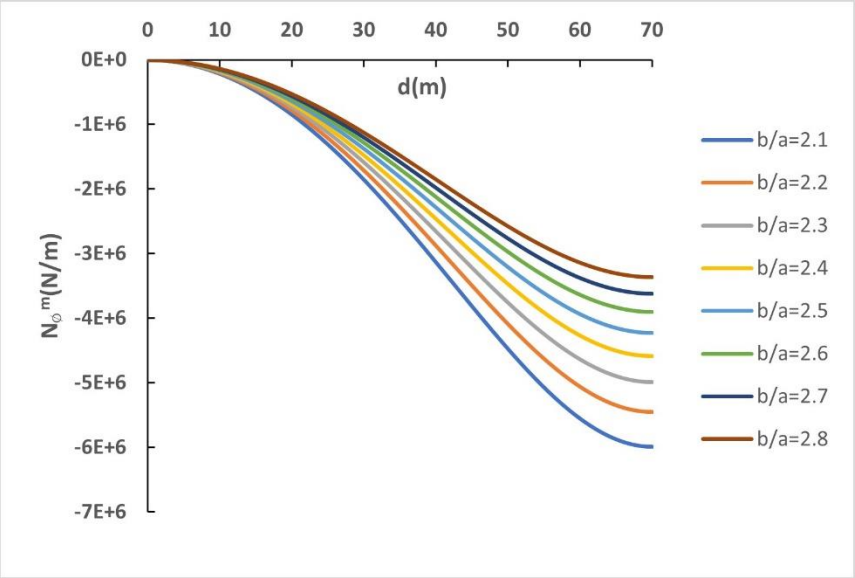

Figure 4-4:Variation of membrane meridional stress resultant with depth d(m) for various b/a ratios

4.1.4 The effect of b/a variation on Hoop stress resultant

The geometric ratio of *b/a* was varied from 2.1 to 2.8 with an increment of 0.1 to assess the effect of varying the ratio on the hoop stress resultant. Figure 4-5 shows the variation of hoop stress resultant with depth *d* for the eight hyperboloidal vessels analysed for hoop stresses. The solutions for hoop stress resultants are derived from equation 3-26, as shown in chapter 3.

Figure 4-5 shows that the hoop stress resultant is zero at the free surface for the eight different vessels. However, the hoop stress resultant increases more rapidly than the corresponding meridional stress resultant. The lines representing various *b/a* ratios are close to each other, indicating that the hoop stress resultant does not vary much from vessel to vessel. The hoop stress resultant increased from zero at the free surface up to where the depth of the liquid is 51 metres below the free surface. In that region, the vessel having the geometric ratio *b/a* of 2.1 experienced greater hoop forces than the other vessels.

As the ratio of *b/a* was increased from **2.1 to 2.8** with an increment of 0.1, in the region **0 <*d*<*51,*** the hoop stress resultant for the geometric ratio of 2.8 was the lowest, while the hoop stress resultant for the geometric ratio of 2.1 was highest. At a point where ***d=51m,*** indicated by a dashed vertical line, as seen in Figure 4-5, all eight hyperboloidal vessels have equal hoop stress resultant. The value of the hoop stress resultant is $\mathbf{11.34\times10^{6}}$ **N/m.** An interesting observation was made in the range **51≤*d*<70.** In this region, as the depth of the liquid *d* increased with an increase in the ratio of *b/a*, the stress resultant also increased. The opposite behaviour was observed earlier in region **0 <*d*<*51,*** where the hoop stress resultant decreased with increased depth of the liquid and *b/a* ratio. The peak hoop stress on the hyperboloidal vessel subjected to hydrostatic pressure was maximum for the geometric ratio b/a of 2.8.

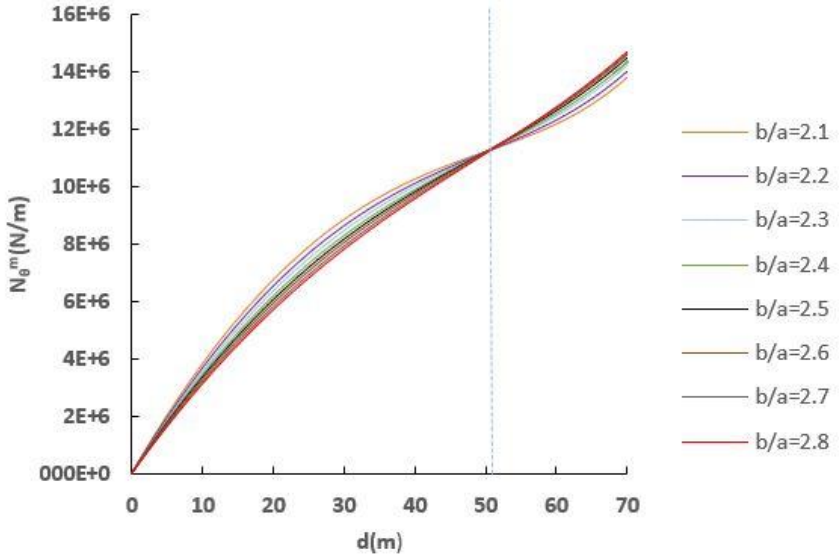

Figure 4-5:Membrane hoop stress resultant variation with depth for various b/a ratios

4.1.5 Summary of observations on the parametric study on stress analysis

In summary, an increase in the ratio *b/a* from vessel-to-vessel results in a decrease in membrane meridional stress resultants. For each vessel, the meridional stress resultant varied from zero at the free surface of the liquid to the maximum stress resultant at the maximum depth *d* of each vessel, which is at the base of the vessel. This observation agrees with the existing literature that the more curved the surface is, the better it resists the membrane meridional stress resultants.

Curved surfaces (shell structures) use almost wholly the extensional action than the bending action to resist applied transverse loads as reported in the existing literature. This is provided that the suitable boundary conditions, such as smoothness criteria for variations of shell loading and geometry, are met (Zingoni,2018:10). The current study of investigating the stresses behaviour for negative Gaussian surfaces under hydrostatic loading also agrees with existing literature curvature.

The maximum hoop stress resultants do not vary much from vessel to vessel, as seen in Table 4-4. As the depth *d* increases with the increasing geometric ratio of *b/a*, the hoop stress resultant is in tension at all points on the surface. The behaviour of the stress resultant changes at *d=51m,* and that is the point where all eight liquid containment vessels have the same hoop stress resultant. The hoop stress resultant increases more rapidly (see Table 4-4) than the meridional stress resultant; therefore, it is the governing stress resultant in designing the vessel.

Table 4-4:Maximum meridional versus maximum hoop stress resultants for various b/a ratios

b/a	$N^m_{ø}$ (N/m)	$N^m_{θ}$ (N/m)
2.1	-6.0E+6	13.8E+6
2.2	-5.5E+6	14.0E+6
2.3	-5.0E+6	14.2E+6
2.4	-4.6E+6	14.4E+6
2.5	-4.2E+6	14.5E+6
2.6	-3.9E+6	14.6E+6
2.7	-3.6E+6	14.7E+6
2.8	-3.4E+6	14.7E+6

4.2 Linear Eigenvalue Buckling Analysis

A linear eigenvalue buckling analysis was carried out following the method outlined in section 3.2.2 of chapter 3. This analysis was carried out to assess regions on the vessel that show high compressive stresses with the variation of the geometrical ratio *b/a* since high compressive stresses can cause buckling. Similarly, with the stress analysis, the buckling analysis was performed on eight vessels with different *b/a* ratios from 2.1 to 2.8.

4.2.1 Validation

Before performing linear eigenvalue buckling analysis on the hyperboloidal vessel, validation of the eigenvalue buckling analysis was performed on a spherical cap when subjected to uniform pressure p = 1MPa, as outlined in section 3.1.2.1 of chapter 3. The buckling pressure obtained from the analytical analysis was p_{cr} =0.254MPa. The FEM method was also used to solve the same problem, and buckling pressure was obtained as p_{cr} =0.2559MPa, as seen in Figure 4-6. The percentage error on the result obtained from the two methods was 0.74%. This result is acceptable and gives the basis for analysing the current research problem.

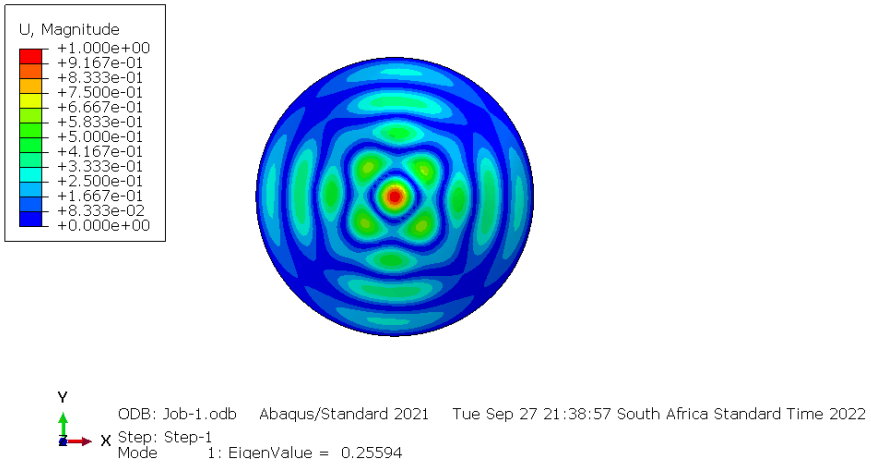

Figure 4-6:Mode shape and the corresponding eigenvalue of a spherical cap

From Figure 4-6, it can be seen that the buckling deformation of the spherical cap is symmetric due to the application of the uniform loading on the spherical cap.

4.2.2 Numerical results

For the hyperboloidal vessel, due to its complex geometry, it seemed almost impossible to come up with an equation that could predict the linear buckling analysis of such a vessel. Therefore, only the Finite-element modelling method was carried out to analyse the eight vessels being investigated. First, the eigenvalues (λ) obtained from ABAQUS were multiplied with the reference pressure to get the numerical values of the critical buckling pressure ($Pcr=\lambda p$) on the different vessels.

Table 4-5:Numerical values of Buckling pressure with the variation of b/a

b/a	Eigenvalue(λ)	Pcr (kN/m^2)
2.1	-24.914	-24.914
2.2	-25.696	-25.696
2.3	-26.402	-26.402
2.4	-27.075	-27.075
2.5	-27.720	-27.720
2.6	-28.298	-28.298
2.7	-28.883	-28.883
2.8	-29.340	-29.340

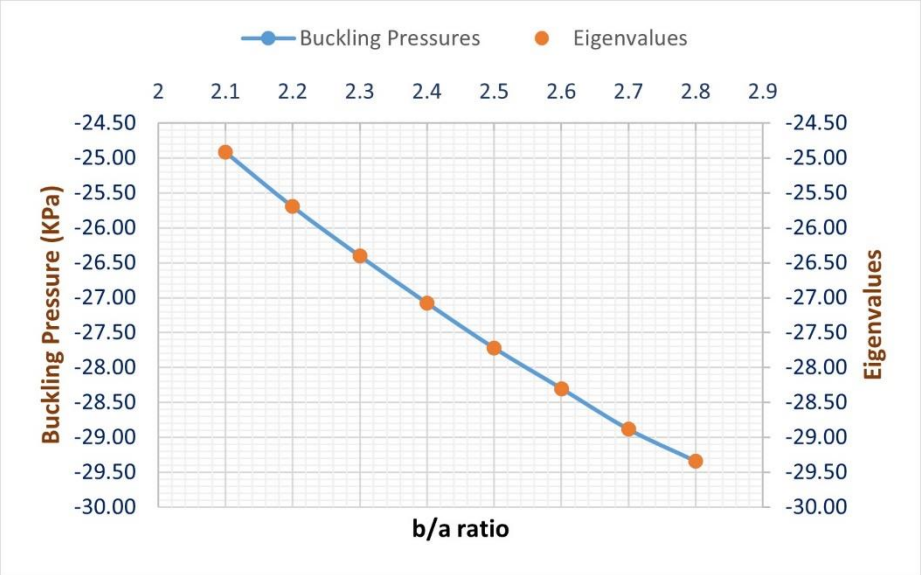

Figure 4-7:Variation of linear buckling capacity of hyperboloidal vessel with the ratio of b/a

Figure 4-7 shows the variation of critical buckling pressure with an increase in the geometrical ratio of *b/a*. As the ratio of *b/a* increases, the linear-buckling capacity of the vessel increases. Starting at a p_{cr} = -24.*914MPa at b/a=2.1 to* p_{cr} = *-29.340MPa* when *b/a=2.8* for the first buckling mode. The analysis was performed keeping the thickness of the shell constant at *t=0.1m* from the free surface to the thickness at the support t_s *=0.1m.*

When subjected to the hydrostatic loading, the different vessels' meridional stress resultants were in the full compressive regime. Furthermore, as the ratio of *b/a* increased, the meridional stress resultants decreased. Therefore, since buckling results from high compressive forces, increasing the ratio of *b/a* increased the buckling capacity of the vessel.

4.2.3 Mode shapes

The mode shapes show the vessel's failure modes under buckling stresses pictorially. For example, Figure 4-8 to Figure 4-15 show the buckling mode shapes of the hyperboloidal vessel with the geometric ratio of *b/a*=2.1 to 2.8 with an increment of 0.1 from vessel to vessel. For each vessel, the eigenvalues occur in pairs (repeated eigenvalues), which can be related to symmetrical structural system response, as seen in Table 4-6.

The other observation is that the eigenvalues are negative, which means that for buckling to occur on the vessel, the loading must be reversed, and the first eigenvalue means that the liquid contained must be 24.914 times denser than water for the vessel to buckle. The magnitude of the eigenvalue also represents the factor of safety, in this case 24.9 which is significantly greater than 1, giving us confidence to further study the negative Gaussian surfaces for the

possibility of being used in large capacity liquid containment even though only liner buckling analysis was conducted (Zingoni, 2022).

Table 4-6:Eigenvalues for first five modes for a vessel of b/a=2.1

	Eigenvalues	Buckling Pressure (kN/m^2)
λ_1	-24.914	-24.914
λ_2	-24.914	-24.914
λ_3	-25.878	-25.878
λ_4	-25.878	-25.878
λ_5	-28.574	-28.574

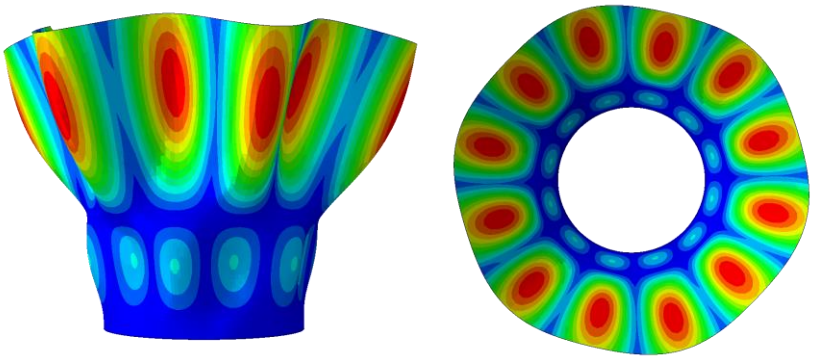

Figure 4-8:Mode 1 for **b/a** ratio of **2.1**, (Left)-side view, (right)-plan view

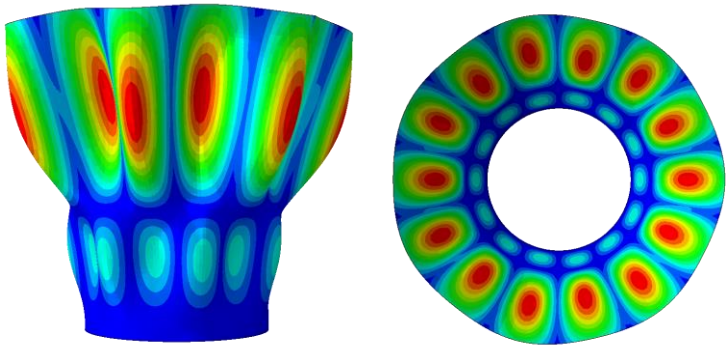

Figure 4-9:Mode 1 for **b/a** ratio of **2.2**, (Left)-side view, (right)-plan view

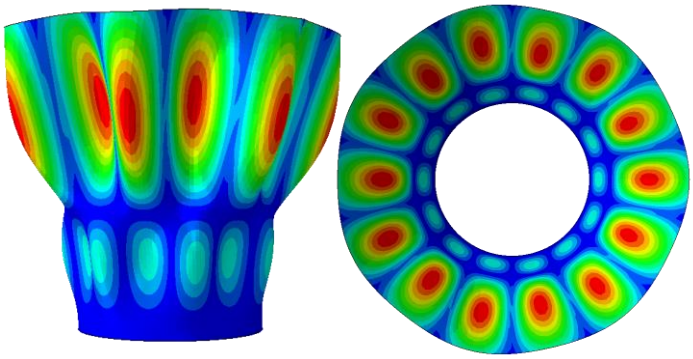

Figure 4-10:Mode 1 for **b/a** ratio of **2.3**, (Left)-side view, (right)-plan view

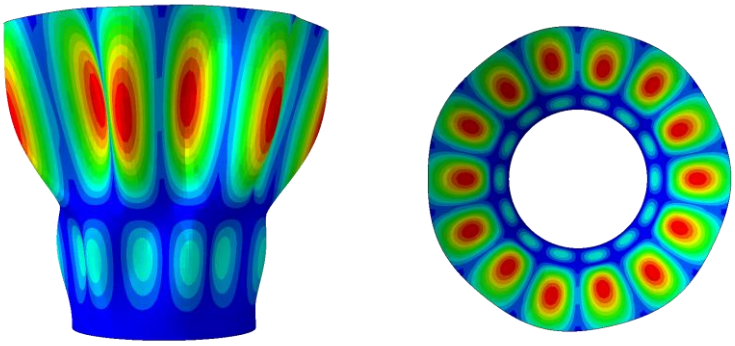

Figure 4-11:Mode 1 for **b/a** ratio of **2.4**, (Left)-side view, (right)-plan view

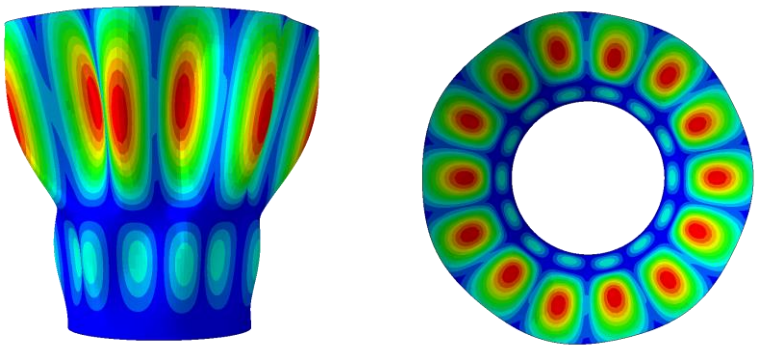

Figure 4-12:Mode 1 for **b/a** ratio of **2.5**, (Left)-side view, (right)-plan view

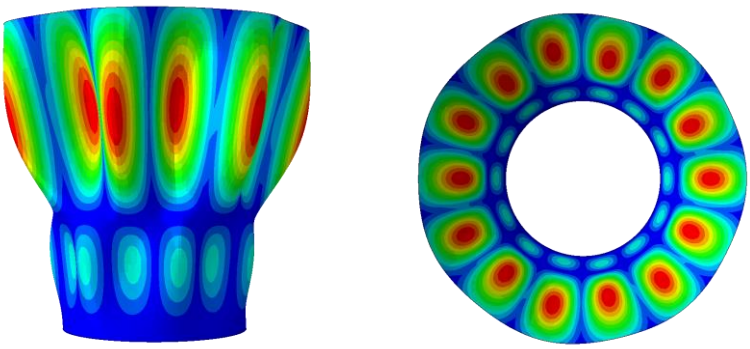

Figure 4-13:Mode 1 for **b/a** ratio of **2.6**, (Left)-side view, (right)-plan view

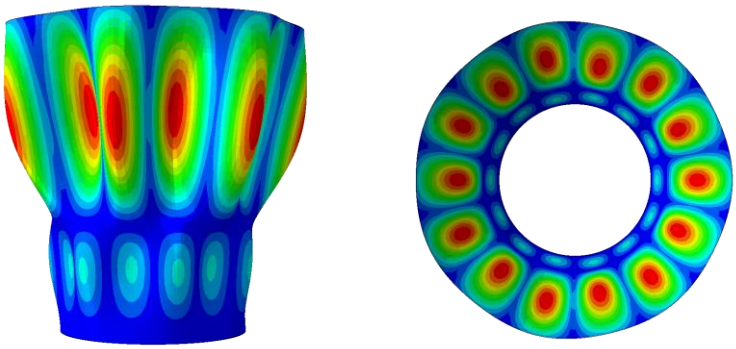

Figure 4-14:Mode 1 for **b/a** ratio of **2.7**, (Left)-side view, (right)-plan view

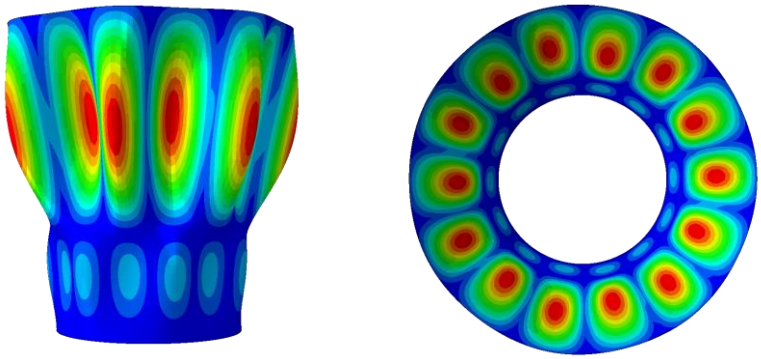

Figure 4-15:Mode 1 for **b/a** ratio of **2.8**, (Left)-side view, (right)-plan view

4.2.4 Concluding remarks on linear buckling analysis

It can be concluded that increasing the geometric ratio of *b/a* increases the linear buckling capacity of the vessel when subjected to hydrostatic loading. Furthermore, the eigenvalues occur in pairs, which resembles a feature of symmetry of symmetrical structural systems. The high factors of safety in Table 4-5 for the studied vessels under hydrostatic pressure in linear buckling analysis motivate for further analysis considering imperfections (non-linear buckling analysis).

In chapter five, a comparison of the membrane stress resultants while monitoring the tank's capacity will be made, and a conclusion will also be made on which tank performs better.

5 Comparative Studies

A comparative study was conducted on the stress analysis of the hyperboloidal vessel versus the circular cylindrical vessel to assess the structural feasibility of the hyperboloidal vessel. In addition, the stress resultants of the circular cylinder under hydrostatic loading were studied (Zingoni, 2018). The analytical equations governing the stress analysis of the two vessels compared in this section will be outlined.

5.1 The Circular cylindrical vessel

The analytical stress resultant equations of a circular cylinder, as studied by (Zingoni, 2018:69), are shown in equation 5-1 and equation 5-2. The hoop stress resultant is equation 5-1, and the stress in the meridional direction is shown in equation 5-2.

$$N_\theta = \gamma a x \quad \textbf{(5-1)}$$

$$N_x = 0 \quad \textbf{(5-2)}$$

Equation 5-1 shows a linear variation of the hoop stress resultant with the depth of the liquid *x*.

Where: γ is the unit weight of the contained liquid
a is the radius of the vessel
x is the depth of the liquid

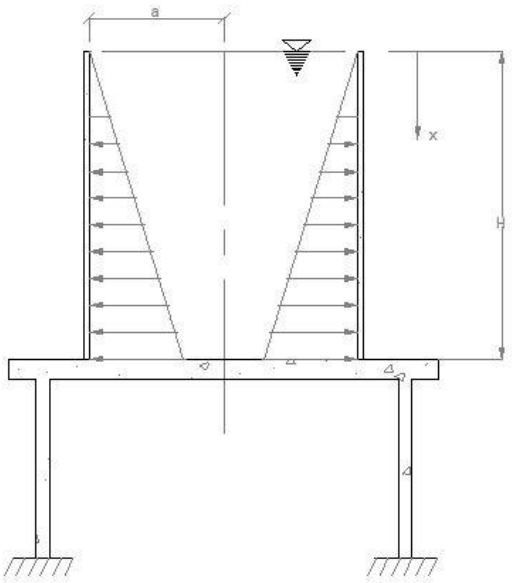

Figure 5-1:circular elevated-liquid storage vessel (Zingoni,2018:69)

The meridional and hoop stress resultant analytical solution equations of the hyperboloidal vessel can be found in equation 3-24 and equation 3-26, respectively.

The comparison was made, keeping the height of both tanks at 70*m*, while the radius of the circular tank varied from 19.714*m* to 21.04*m*. The assessment was made on the maximum hoop stress resultants for various *b/a* ratios at a depth of 70*m*. The volume capacities of both tanks were monitored for the same maximum hoop stress resultant on the circular cylindrical and hyperboloidal vessels. In comparison, the hyperboloidal vessel performed better when monitoring the volume-peak hoop stress behaviour for the same volume and height of both vessels.

The volume of the hyperboloidal vessel *V* was calculated using equation 5-4, an equation derived using the general equation 5-3 for the volume of surfaces of revolution using the method of discs (J.Steward,2016).

$$V = \pi \int_0^H r^2 dx \qquad \textbf{5-3}$$

$$V = \pi a^2 \times \left[H + \frac{H^3}{3b^2} \right] \qquad \textbf{5-4}$$

Table 5-1 shows the effect of *b/a* variation on the maximum hoop stress resultant on the eight different hyperboloidal vessels investigated in the current study. It can be seen that as the *b/a* ratio increases, the peak hoop stress resultant increases, while on the other hand, the volume decreases. Therefore, for the choice of tank, the one with a *b/a* ratio of 2.1 would be best as it has more capacity when compared with the other tanks. The other reason is that it has the lowest peak hoop stress result of the eight vessels examined in this study.

Table 5-1:Hyperboloidal vessel volumes and peak hoop stress resultants

b/a	N_θ **(MN/m)**	**Volume (m^3)**
2.1	13.80	184526.16
2.2	14.03	177290.02
2.3	14.21	170977.04
2.4	14.36	165436.62
2.5	14.48	160547.66
2.6	14.58	156211.89
2.7	14.66	152348.90
2.8	14.73	148892.35

In Table 5-2, the peak hoop stress resultant decreases as the volume decreases for the circular cylinder.

Table 5-2:Circular vessel volumes and peak hoop stress resultants

vessel	N_θ (MN/m)	Volume (m^3)
1	20.3	184526.16
2	19.9	177290.02
3	19.5	170977.04
4	19.2	165436.62
5	18.9	160547.66
6	18.7	156211.89
7	18.4	152348.90
8	18.2	148892.35

Adopting the structural efficiency of the vessel equation by Zingoni, 2002, equation 2-4,

Figure 5-2 shows the efficiency variation with the ratio of *b/a* of the hyperboloidal vessel with the calculations shown in Table 5-3. As the ratio of *b/a* increases, the efficiency of the hyperboloidal vessel decreases. However, even though it decreases, it decreases gradually. This is due to the gentle slope of the curve in Figure 5-2.

Table 5-3:Effeciency of different hyperboloidal vessels

b/a	Volume (m^3)	$(N_\theta)_{peak}$ (MN/m)	η
2.1	184526.16	13.80	1.91
2.2	177290.02	14.03	1.81
2.3	170977.04	14.21	1.72
2.4	165436.62	14.36	1.65
2.5	160547.66	14.48	1.58
2.6	156211.89	14.58	1.53
2.7	152348.90	14.66	1.48
2.8	148892.35	14.73	1.44

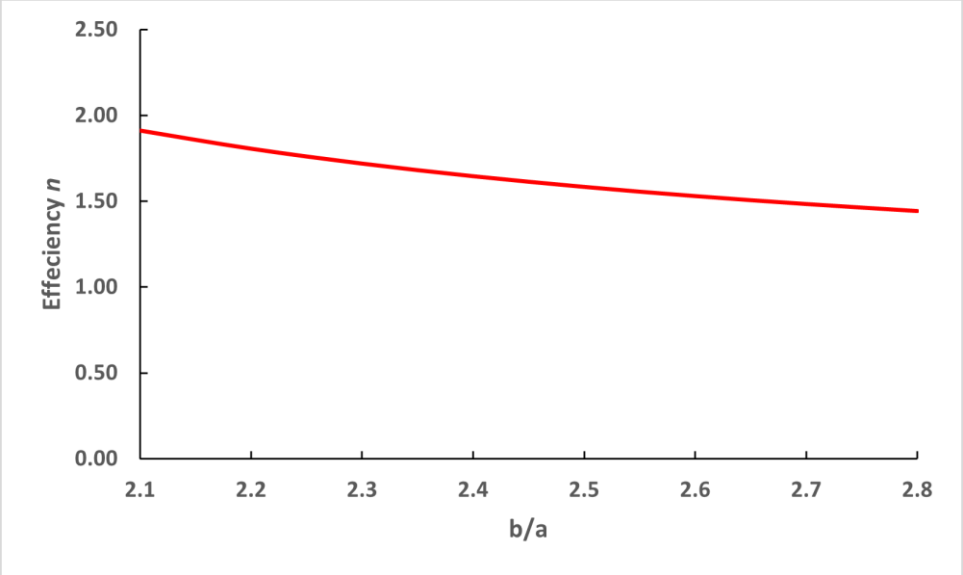

Figure 5-2:Effeciency variation with b/a ratio for hyperboloidal vessels

5.2 Concluding remarks

It was found that the hyperboloidal vessel is structurally feasible. This conclusion is based on comparing the circular tank and hyperboloidal vessel on the membrane hoop stress resultants. The membrane peak hoop stress resultant on the base of the hyperboloidal vessel decreased as the tank's capacity increased, which also observed a decrease in the *b/a* ratio. Conversely, an increase in the volume of the circular tank caused an increase in membrane peak hoop stress resultant.

Therefore, the hyperboloidal vessel can be used as a new, more efficient shell configuration for high-capacity, elevated liquid storage. In addition, concrete water tanks could be constructed into various shapes because fresh concrete can be moulded into different shapes using formwork.

6 Summary, Conclusion, and Recommendations

6.1 Summary

This study investigated the structural feasibility of negative Gaussian surfaces in the form of a hyperboloid of revolution when used in liquid containment applications. To the author's knowledge, this is a novel study in the given context. The structural feasibility study was conducted by varying the geometric ratio *b/a* from 2.1 to 2.8, giving a total of eight vessels studied. The closed-form analytical solutions were found based on the membrane theory for the hyperboloid of revolution when subjected to hydrostatic pressure. The feasibility study was based on the membrane stresses in the form of plots produced from the analytical solutions. To validate the correctness of the close-form solutions, FEM software ABAQUS was used, and the percentage error difference between the two analysis methods was calculated, which showed excellent results as shown in Table 4-2 and Table 4-3, and graphically in Figure 4-2 and Figure 4-3.

Linear eigenvalue buckling analysis was conducted using finite-element analysis software ABAQUS to inform the design engineer of the buckling pressures that would cause buckling instability due to high compressive stresses caused by loading on the structure. The associated failure modes due to buckling when subjected to high compressive stresses were also presented in chapter 4. The calibration of the FEM model on linear eigenvalue buckling analysis was based on literature, as indicated in chapter 4.

6.1.1 Parametric study

The parametric study was conducted based on the effect of varying the geometric ratio *b/a* on the membrane stresses. The membrane meridional stresses were in compression throughout the structure's surface for all eight tested vessels. Conversely, the membrane hoop stress resultants were positive (tensile) from the free surface to the tank's base. The compressive meridional stresses led to further investigation of the structural feasibility, which also investigates the structure's buckling response. Buckling analysis was only based on the linear eigenvalue buckling analysis to give insights into what to expect when buckling occurs due to large compressive stresses on the structure.

The increase in the geometric ratio of *b/a* from vessel to vessel decreased meridional stress resultants from vessel to vessel. The membrane hoop stress resultant showed the same trend up to a point at a 51-metre depth where all vessels shared the same hoop stress resultant and behaved differently afterwards. After this point towards the base of the tank, an increase in the *b/a* ratio led to an increase in hoop stress resultant, with the maximum *b/a* ratio vessel having the maximum hoop stress resultant.

The increase in the geometric ratio of *b/a* was found not to cause a significant change in the linear critical buckling capacity of different vessels from vessel to vessel, as shown in Figure 4-7.

6.1.2 Comparative study

A comparative study was conducted between the hyperboloidal vessel and the circular tank. The comparison was based on the membrane hoop stress resultant given by closed-form analytical results for the two vessels. The hyperboloidal vessel was found to perform better than the circular tank while looking at the peak hoop stress resultants, fixing the volume and height of the tanks to be the same for both tanks.

6.2 Conclusions

Figure 5-2 shows the structural efficiency variation with the *b/a* ratio for different hyperboloidal vessels graphically. The structural efficiency does not vary much from vessel to vessel based on the containment volume to peak hoop stress ratio. Likewise, the linear buckling capacity does not vary much from vessel to vessel, with an increase in the *b/a* ratio of the hyperboloidal vessel. Therefore, looking at the efficiency and the comparative study on the circular tank and hyperboloidal vessel, the hyperboloidal profile vessel can be regarded as one of the best solutions for large-capacity liquid containment structures.

6.3 Recommendations

6.3.1 Design recommendations

Based on the findings of this study, the design of the hyperboloidal vessel for liquid containment can be carried out as follows. The maximum hoop stress resultants are more than twice the meridional stress resultants for the hyperboloidal vessel, as seen in Figures 4-4 and 4-5 for reference. As a result, the hoop stress resultants govern the structural design of the hyperboloidal vessel. If the structural designer knows the capacity in the volume of the community to be served, the base diameter of the tank can be initially guessed, and from the *b/a* ratios, the value of *b* can be estimated. As a result, the height *H* of the tank can be estimated from equation 5-4. The closed form equation 3-26 can be used to determine the maximum hoop stress at the base of the tank based on the procedure under the numerical results section in chapter 4.

The structure's thickness at the base can be determined by equating the maximum allowable tensile service stress given in the available design standard as the starting point. The structural design procedure may then be carried out based on the available standards in the industry to check different failure mechanisms on prestressed concrete for liquid containment vessels. If

the structure fails at a given failure mechanism, check that the tank's wall can be gradually thickened to emanate the stresses at the base, the maximum thickness being at the base as expected. Additionally, the normal reinforcing bars may be supplied to also minimise the stresses on the structure based on the need discovered after checking the ultimate flexural capacity of the structure.

6.3.2 Recommendations for future research

The current study only looked at the membrane stress resultants with a parametric stress study on the wall of the hyperboloidal vessel. The linear eigenvalue buckling analysis was also conducted to inform the design engineer of the structural feasibility of such a profile for high-capacity liquid containment. Further studies should be conducted on the bending theory of the shells of revolution applied to the hyperboloidal liquid containment vessel. This provides information on the vertical bending moments generated at the base-to-wall interaction junction. When the vertical bending moments are known, the total stresses in the structure can be determined to aid the complete static analysis of the vessel.

The nonlinear buckling analysis of the vessel may be carried out by introducing the geometric imperfections on shell geometry based on eigenmodes of linear buckling to ease the possibility of tracing the post-buckling behaviour of the vessel. Linear buckling analysis overestimates the buckling pressure of the structure (Zingoni,2022).

The structural dynamics of the structure may be carried out in the future by looking at non-symmetric loadings such as wind and seismic loading to check the elevated structure's behaviour under dynamic loading and the associated shape modes of failure for the completeness of the design.

References

Adachi, J. & Benicek, M. 1964. Buckling of Torispherical Shells Under Internal Pressure The elastic instability of the toroidal knuckle portion of torispherical shells is examined experimentally using plastic models. *Experimental Mechanics*. 4(8):217–222.

Ali, M.A.K.M. al. 2018. Design Offshore Spherical Tank Support using Shape Uptimization. In *6th IIAE International Conference on Intelligent Systems and Image Processing* . Institute of Industrial Applications Engineers. 269–275. DOI: 10.12792/icisip2018.051.

Ansary, A. el, Damatty, A. el & Nassef, A. 2011. Optimum Shape and Design of Cooling Towers. *Waset.Org*. 9(January):4–13. Available: http://waset.org/journals/waset/v60/v60-2.pdf.

Barathan, V. & Rajamohan, V. 2022. Nonlinear buckling analysis of a semi-elliptical dome: Numerical and experimental investigations. *Thin-Walled Structures*. 171(November 2021):108708. DOI: 10.1016/j.tws.2021.108708.

Bektas, S. 2017. Design of Hyperboloid Structures. *MOJ Civil Engineering*. 3(6):414–420. DOI: 10.15406/mojce.2017.03.00089.

British Standards Institution. 1987. *British standard code of practice for design of concrete structures for retaining aqueous liquids.* British Standards Institution.

Closner, J.J. 1960. *Use of Prestressed Concrete for Storage Facilities*.

Enoma N. 2018. Studies on Strength and Stability of Toroidal Shell Forms for Containment Applications. University of Cape Town.

Enoma N, O, E.H., Itoje H J & Unueroh U G. 2015. *Membrane Solutions For Circular Toroidal Shells Under Internal Hydrostatic Pressure*. Available: www.jmest.org.

Flügge, W. 1960. *Stresses in Shells*. Berlin, Heidelberg: Springer Berlin Heidelberg. DOI: 10.1007/978-3-662-01028-0.

Frank J, V. & Michel P, C. 1987. The Modified Compression-Field Theory for Reinforced Concrete Elements subjected to shear. *American Concrete Institude*. 83(22). Available: http://www.vectoranalysisgroup.com/journal_publications/jp2.pdf [2022, February 15].

Galletly, G.D. 1998. *P I I : S 0 2 6 3-8 2 3 1 (9 7) 0 0 0 3 0-X Elastic Buckling of Complete Toroidal Shells of Elliptical Cross-Section Subjected to Uniform Internal Pressure*.

Galletly, G.D. & Blachut, J. 1995. Stability of complete circular and non-circular toroidal shells. *Proceedings of Institution of Mechanical Engineers*. 209:245–255.

Jones, D.P., Holliday, J.E. & Larson, L.D. 1999. Elastic-Plastic Failure Analysis of Pressure Burst Tests of Thin Toroidal Shells. *Journal of pressure vessel technology*. 121(2):149–153. Available: http://www.asme.org/about-asme/terms-of-use.

Kennedy, R.C. 1944. *East Bay Municipal Utility Dist*. Available: http://about.jstor.org/terms.

Krivoshapko, S.N. 2007. Research on general and axisymmetric ellipsoidal shells used as domes, pressure vessels, and tanks. *Applied Mechanics Reviews*. 60(1–6):336–355. DOI: 10.1115/1.2806278.

Li, K., Zheng, J., Liu, S., Ge, H., Sun, G., Zhang, Z., Gu, C. & Xu, P. 2019. Buckling behavior of large-scale thin-walled ellipsoidal head under internal pressure. *Thin-Walled Structures*. 141(March):260–274. DOI: 10.1016/j.tws.2019.04.031.

Mahfouz, S.Y. 2007. Shape optimization of shell structures. In *Proceeding of the 12-th ASAT Conference*. 1–10. DOI: 10.1080/12506559.1993.10511083.

Mathieu, G.O., Shambina, S.L. & Jaafar, Q. 2021. Geometric modelling and materially nonlinear numerical analysis of shells in the shape of one-sheet hyperboloid of revolution. *Advances in the Astronautical Sciences*. 174(3):753–765. DOI: 10.22363/1815-5235-2019-15-3-210-218.

Nasir, A.M., Thambiratnam, D.P., Butler, D. & Austin, P. 2002. Dynamics of axisymmetric hyperbolic shell structures. *Thin-Walled Structures*. 40(7–8):665–690. DOI: 10.1016/S0263-8231(02)00019-8.

Petrović, R., Živković, M., Topalović, M. & Slavković, R. 2015. Analytical, numerical and experimental stress assessment of the spherical tank with large volume. *Tehnicki Vjesnik*. 22(5):1135–1140. DOI: 10.17559/TV-20130905131504.

Ponath, A.P. & George, M. 2016. Study on Buckling Behaviour of Hyperbolic Cooling Towers. 3(5):3–8.

Priestley M.J.N. 1985. Analysis and Design of Circular Prestressed Concrete Storage Tanks. *PCI*. 64–85.

Purdel, C. & Stere, M. n.d. *Stress analysis of toroidal shell*.

Rizkalla, S.H. & Zia, P. 1980. Segmentally Constructed Prestressed Concrete Hyperboloid Cooling Tower. *Journal - Prestressed Concrete Institute*. 25(4):146–161. DOI: 10.15554/pcij.07011980.146.161.

Sharma, H., Sharma, H. & Mukhija, M. 2021. A Review on Thin-shell Structures: Advances and Trends. 2(2):950–952.

Song, G.K. & Sun, B.H. 2022. Nonlinear investigation of Gol'denveizer's problem of a circular and elliptic elastic torus. *Thin-Walled Structures*. 180. DOI: 10.1016/j.tws.2022.109862.

Subramani, T. & Sugathan, A. 2012. Finite Element Analysis of Thin Walled-Shell Structures by ANSYS and LS-DYNA. *International Journal of Modern Engineering Research (IJMER) www.ijmer.com*. 2(4):1576–1587. Available: http://scholar.google.com/scholar?hl=en&btnG=Search&q=intitle:Finite+Element+Analysis+of+Thin+Walled-Shell+Structures+by+ANSYS+and+LS-DYNA#0.

Sutcliffe, W.J. 1971. STRESS ANALYSIS OF TOROIDAL SHELLS OF ELLIPTICAL CROSS-SECTION. *Int. J. mech. Sci*. 13:951–958.

Trahern J.W. 1955. Prestressed Concrete Tanks at East Bay. *American Water Works Association*. 47(2):186–194. Available: https://about.jstor.org/terms.

Vu, V.T. 2015. Minimum weight design for toroidal shells with strengthening component. *Journal of Pressure Vessel Technology, Transactions of the ASME*. 138(2). DOI: 10.1115/1.4031445.

Yu, Q.Q., Gu, X.L., Li, Y. & Lin, F. 2016. Collapse-resistant performance of super-large cooling towers subjected to seismic actions. *Engineering Structures*. 108:77–89. DOI: 10.1016/j.engstruct.2015.11.023.

Zhang, J., Wang, M., Wang, W. & Tang, W. 2017. Buckling of egg-shaped shells subjected to external pressure. *Thin-Walled Structures*. 113:122–128. DOI: 10.1016/j.tws.2017.01.017.

Zhang, J., Wang, M., Wang, W., Tang, W. & Zhu, Y. 2017. Investigation on egg-shaped pressure hulls. *Marine Structures*. 52:50–66.

Zhang, J., Hua, Z., Tang, W., Wang, F. & Wang, S. 2018. Buckling of externally pressurised egg-shaped shells with variable and constant wall thicknesses. *Thin-Walled Structures*. 132:111–119. DOI: 10.1016/J.TWS.2018.08.013.

Zhang, J., Dai, M., Wang, F., Tang, W. & Zhao, X. 2021. Buckling performance of egg-shaped shells fabricated through free hydroforming. *International Journal of Pressure Vessels and Piping*. 193. DOI: 10.1016/j.ijpvp.2021.104435.

Zia, P. & Mostafa, M.T. 1983. Experimental Study of a Segmentally Constructed Cooling Tower. *Journal - Prestressed Concrete Institute*. 28(3):126–149. DOI: 10.15554/pcij.05011983.126.149.

Zingoni, A. 1995. On membrane solutions for elevated shell-of-revolution tanks of certain meridional profiles. *Thin-Walled Structures*. 22(2):121–142. DOI: 10.1016/0263-8231(94)00025-U.

Zingoni, A. 1999. Self-weight Stresses in Hyperbolic Cooling Towers of General Shape. 14(4):281–294.

Zingoni, A. 2001. Stresses and deformations in egg-shaped sludge digestors Discontinuity effects Junctions.pdf. *Engineering Structures*. 23(11):1373–1382. DOI: https://doi.org/10.1016/S0141-0296(01)00056-6.

Zingoni, A. 2002. Parametric stress distribution in shell-of-revolution sludge digesters of parabolic ogival form. *Thin-Walled Structures*. 40(7–8):691–702. DOI: 10.1016/S0263-8231(02)00020-4.

Zingoni, A. 2015. Liquid-containment shells of revolution: A review of recent studies on strength, stability and dynamics. *Thin-Walled Structures*. 87:102–114. DOI: 10.1016/j.tws.2014.10.016.

Zingoni, A. 2018. *Shell Structures in Civil and Mechanical Engineering*. Second ed. London,UK: ICE. DOI: 10.1680/ssicame.60289.

Zingoni, A. 2022. Stress and buckling resistance of dual-purpose concrete shells. *Thin-Walled Structures*. 170(July 2021):108596. DOI: 10.1016/j.tws.2021.108596.

Zingoni, A. & Pavlovic, M.N. 1993. *Discontinuity Phenomena around the Supports of Stepwise-Thickened Spherical Steel Tanks. Part 1: Theoretical Considerations and Parametric Results*.

Zingoni, A. & Pavlovic, M.N. 1991. Effect of support conditions in liquid-filled spherical vessels. Part l : limiting ring-beam stiffnesses. In *Institution of Civil Engineers*. 323–345.

Zingoni, A., Mokhothu, B. & Enoma, N. 2015. A theoretical formulation for the stress analysis of multi-segmented spherical shells for high-volume liquid containment. *Engineering Structures*. 87:21–31. DOI: 10.1016/j.engstruct.2015.01.002.

Zingoni, A., Enoma, N. & Govender, N. 2015. Equatorial bending of an elliptic toroidal shell. *Thin-Walled Structures*. 96:286–294. DOI: 10.1016/j.tws.2015.08.017.